

Geometric Tolerance Quantification and Prediction Framework
for Additive Manufacturing Processes

by

Baltej Singh Rupal

A thesis submitted in partial fulfillment of the requirements for the degree of
Doctor of Philosophy

Department of Mechanical Engineering
University of Alberta

© Baltej Singh Rupal, 2021

Abstract

Additive Manufacturing (AM) is an advanced manufacturing technology used to manufacture custom and geometrically complex parts using a layer-by-layer material addition process. Variations in the AM process lead to ‘deviations’ in the manufactured part, resulting in geometric non-conformance. To date, the geometric conformance or tolerance quantification for AM relies on two major methods: experimental methods based on geometric benchmark test artifacts (GBTA) and predictive methods such as finite element analysis (FEA). A common limitation in these methods is non-compliance with ISO 1101 standard [ISO 1101, 2017], i.e., usage of GD&T (geometric dimensioning and tolerancing). GD&T enables complete geometric quantification of form, orientation, and location of any mechanical part and should be used for AM parts to ensure geometric conformance. Experimental methods lack GD&T quantification due to GBTA design issues. There are limitations in design guidelines in terms of geometric conformance and linkage of features to GD&T is missing. Designing GBTAs without considering these factors leads to unnecessary experimentation and partial GD&T characterization. On the other hand, predictive methods lead only to geometric deviation regions and/or residual stresses on the part but do not estimate the GD&T characteristics. Due to these limitations, there are process specific gaps which need to be addressed. Such as, the need for parametric optimization for GD&T and assemblability for fused filament fabrication (FFF) process; along with the consideration of bead geometry in modeling methodologies. In laser powder bed fusion (LPBF), there is a need for GD&T based data-sets considering the effect of removal of base plate. Further, there is no methodology present in literature that leads to GD&T predictions and assemblability information.

Based on these research gaps, this thesis aims at developing a framework to quantify and predict the geometric tolerances and assemblability of AM parts based on GD&T standards. A

systematic GBTA design methodology is first proposed that links the features to GD&T and helps in assemblability investigation. Based on the new design methodology, newGBTAs are designed for conducting geometric quantification and prediction for different AM processes. For FFF, a new GBTA is designed to understand the effect of process parameters on GD&T and assemblability. The results suggest a direct dependence of GD&T and assemblability on the process parameters which were not studied before such as motor micro-stepping, component size, and material type. Further, a virtual geometric conformance investigation methodology was developed by converting the sliced file into a solid model. The resultant model called ‘the reverse CAD model’ is capable of performing accurate virtual geometric conformance investigation. This not only helps to reduce part rejection, but also helps in virtual design/parametric changes before manufacturing the part. For LPBF, a normative GBTA is designed for generic tri-planar GD&T quantification before and after removing the GBTA from the baseplate. The experimental GD&T results are compared with simulation results to understand the reliability of numerical simulations for GD&T prediction. The results provide a complete GD&T data-set for LPBF process, show a wide variation in GD&T results proving the need for GD&T based quantification, and provide quantified data about the usability of the simulation-based GD&T. Further, skin model shapes methodology is implemented for the first-time for LPBF to predict deviations leading to GD&T and assemblability estimation. To summarize, this thesis presents a framework for GD&T based assemblability investigation for AM using experimental and predictive methodologies.

Preface

This thesis presents an account of the original research work by Baltej Singh Rupal. Research articles originating from this thesis have been published in reputed journals and conference proceedings and are listed below.

List of journal articles and proceedings:

Obj. 1	<p>1. B.S. Rupal, R. Ahmed, A.J. Qureshi, “Feature-based methodology for design of geometric benchmark test artifacts for additive manufacturing processes”, <i>Procedia CIRP</i>, Vol. 70, pp. 84-89, 2018. Link: https://doi.org/10.1016/j.procir.2018.02.012</p>
Obj. 2	<p>2. B.S. Rupal, K. Ramadass, A.J. Qureshi, “Investigating the effect of motor micro-stepping on the geometric tolerances of Fused Filament Fabrication printed parts”, <i>Procedia CIRP</i>, Vol. 92, pp. 9-14, 2020. Link: https://doi.org/10.1016/j.procir.2020.05.172</p> <p>3. B.S. Rupal, K.G. Mostafa, Y. Wang, A.J. Qureshi, “A reverse CAD approach for virtual estimation of geometric and mechanical properties of FDM printed parts”, <i>Procedia Manufacturing</i>, Vol. 34, pp. 535-544, 2019. Link: https://doi.org/10.1016/j.promfg.2019.06.217</p>
Obj. 3	<p>4. B.S. Rupal, T. Singh., T. Wolfe, M. Secanell, A.J. Qureshi, “Effect of base plate removal on tri-planar geometric tolerances of SS 316L benchmark manufactured on laser powder bed fusion process”, <i>Materials Journal</i>, Vol. 14, issue 13, pp. 1-30, 2021. Link: https://doi.org/10.3390/ma14133575</p>
Obj. 4	<p>5. B.S. Rupal, N. Anwer, M. Secanell, A.J. Qureshi, “Geometric Tolerance and Manufacturing Assemblability Estimation of Metal Additive Manufacturing (AM) Processes”, <i>Materials and Design</i>, Vol. 194, pp. 1-15, 2020. Link: https://doi.org/10.1016/j.matdes.2020.108842</p> <p>6. B.S. Rupal, N. Anwer, M. Secanell, A.J. Qureshi, “Geometric Tolerance Characterization of Laser Powder Bed Fusion Processes Based on Skin Model Shapes”, <i>Procedia CIRP</i>, Vol. 92, pp. 169-174, 2020. Link: https://doi.org/10.1016/j.procir.2020.05.185</p>

List of conference papers:

<p>Background study (Thesis chapter 1)</p>	<p>1. B.S. Rupal, A.J. Qureshi, “Geometric deviation modeling and tolerancing in additive manufacturing: a GD&T perspective”, 1st Conference of NSERC Network for Holistic Innovation in Additive Manufacturing (HI-AM), pp. 1-6, May 2018, Waterloo, Canada. Link: https://www.researchgate.net/publication/325920752</p> <p>2. S.T. Toguem, B.S. Rupal, C. Mehdi-Souzani, A.J. Qureshi, N. Anwer, “A review of AM artifact design methods”, ASPE and euspen Summer Topical Meeting on Advancing Precision in Additive Manufacturing, July 2018, Berkeley, USA. Link: https://www.researchgate.net/publication/326636044</p>
<p>Obj. 3</p>	<p>3. B.S. Rupal, M. Secanell, A.J. Qureshi, “Geometric Benchmark Test Artifact for Laser Powder Bed Fusion Process: Design and Preliminary Results”, 2nd Conference of NSERC Network for Holistic Innovation in Additive Manufacturing (HI-AM), June 2019, pp. 1-7, Vancouver, BC, Canada. Link: http://www.researchgate.net/publication/334098916</p>

Apart from the above-mentioned research publications, this Ph.D. thesis also resulted in several research collaborations which led to the following publications, posters, and presentations:

List of peer-reviewed journal and conference publications:

1. R. Holmes, W. Persons, **B.S. Rupal**, A.J. Qureshi, and P. Currie, "Morphological variation and asymmetrical development in the skull of *Styracosaurus Albertensis*." *Cretaceous Research*, Vol. 107, pp. 1-16, March 2020. Link: <https://doi.org/10.1016/j.cretres.2019.104308>
2. **B.S. Rupal**, E.A. Garcia, C. Ayranci, and A.J. Qureshi, “3D printed 3D-microfluidics: recent developments and design challenges”, *Journal of Integrated Design and Process Science*, Vol. 22, pp. 5-20, 2018. Link: <http://doi.org/10.3233/jid-2018-0001>
3. **B.S. Rupal**, M. Secanell, A.J. Qureshi, “Investigating the effect of the temperature and stress fields on the geometric tolerances of the laser powder bed fusion printed parts”, 3rd Conference of NSERC Network for Holistic Innovation in Additive Manufacturing (HI-AM), June 2020, pp. 1-6, Online conference. Link: <https://www.researchgate.net/publication/342852103>

Invited oral presentations:

1. **B.S. Rupal**, N. Anwer, A.J. Qureshi, “Geometric Benchmark Test Artifacts for Additive Manufacturing: Design guidelines and capability assessment”, 2nd Workshop of the Foundations of Accuracy Control for Additive Manufacturing, June 2019, Paris, France.
2. **B.S. Rupal**, A.J. Qureshi, “Establishing Guidelines for Variation Management in Additive Manufacturing”, 2nd Seminar of the European Group of Research in Tolerancing, June 2017, Metz, France.

Poster presentations:

1. T. Singh, **B.S. Rupal**, T. Wolfe, H. Henein, A.J. Qureshi, “Geometric quality characterization of selective laser melting process”, Additive Manufacturing Alberta, October 2018, Innotech Alberta, Edmonton, Canada.
2. **B.S. Rupal**, T. Wolfe, H. Henein, A.J. Qureshi, “Geometric Quality Control for Metal AM”, Additive Manufacturing Alberta, October 2018, Innotech Alberta, Edmonton, Canada.
3. G. Guney, **B.S. Rupal**, A.J. Qureshi, “Geometric Optimization of 3D Printed Assemblies”, UARE Poster Presentation, March 2018, University of Alberta, Canada.

Dedicated to my family.

Acknowledgements

To start with, I would like to express my sincere gratitude to Dr. Ahmed Jawad Qureshi for giving me the opportunity and scholarship to pursue a Ph.D. degree at the University of Alberta. Over the last few years, Dr. Qureshi's continuous encouragement, support and guidance have made this thesis possible. I sincerely thank Dr. Marc Secanell for co-supervising my thesis and for advising me on various technical and non-technical aspects. I am grateful that both Dr. Qureshi and Dr. Secanell guided me in every step of this work and have helped me through the thick and thin during this Ph.D. project. The countless discussions with both my supervisors not only shaped this thesis work but my personality as well. I would also like to acknowledge Dr. Stanislav Karapetrovic for being a part of my supervisory committee, for providing me constructive feedback during the supervisory committee meetings, and for thesis review. I am thankful to Dr. Nabil Anwer for inviting me to ENS Paris Saclay and allowing me to conduct the collaborative research project that became a part of my thesis work. I would like to thank the thesis committee members and the external examiner Prof. Qiang Huang for sparing their precious time to read the thesis and for providing useful comments.

I would also thank the NSERC HI-AM network grant for funding my research throughout the past few years. Further, I would like to state my immense gratitude and thanks to everyone and anyone who has helped me throughout this journey and helped to bring out the best in me. I am grateful to my friends and lab mates for their help and encouragement during my Ph.D. Last but not least I would like to acknowledge my parents, my younger brother, and my wife for their unconditional love and support that have always pushed me to do better throughout my life.

Table of Contents

1.	Introduction and background	1
1.1.	Background	1
1.2.	AM processes.....	2
1.2.1.	FFF process.....	3
1.2.1.	LPBF process	5
1.3.	Geometric properties and GD&T.....	7
1.4.	Motivation.....	11
1.5.	State-of-the-art	12
1.5.1.	Benchmark artifact design process	13
1.5.2.	Modeling for geometric tolerances	23
1.6.	Objectives	28
2.	Systematic feature-based design methodology for GBTA design for AM.....	29
2.1.	Systematic methodology.....	29
2.2.	Feature technology and assembly consideration.....	31
2.3.	Case study and conclusions	35
3.	Parametric optimization for GD&T and size tolerances for FFF process	38
3.1.	Background and context	38
3.2.	Experimental methodology.....	40
3.3.	Results and discussion	45
3.4.	Conclusions.....	52
4.	Accurate geometric prediction for FFF process.....	53
4.1.	Reverse CAD methodology	54
4.2.	Results and discussion	58
4.3.	Conclusions.....	63
5.	Normative GBTA design and characterization for LPBF process.....	64

5.1.	Experimental procedure	66
5.2.	Measurement procedure.....	67
5.3.	Numerical simulation.....	71
5.3.1.	Governing equations and boundary conditions.....	72
5.4.	Results and discussions.....	76
5.4.1.	Straightness	80
5.4.2.	Flatness	82
5.4.3.	Circularity	84
5.4.4.	Cylindricity	86
5.4.5.	Perpendicularity	88
5.4.6.	Parallelism.....	89
5.4.7.	Angularity	91
5.4.8.	Concentricity.....	91
5.4.9.	Position	92
5.4.10.	Runout tolerances.....	94
5.5.	Conclusions.....	96
6.	GBTA based GD&T and assembly prediction for LPBF process	98
6.1.	Assembly benchmark test artifact (ABTA) design.....	99
6.2.	ABTA design criteria.....	100
6.3.	Skin model shapes based tolerancing	104
6.4.	Prediction phase sample generation based on in-plane shrinkage.....	106
6.5.	Observation phase sample generation based on thermo-mechanical simulations	108
6.5.1.	Implementation and input parameters.....	108
6.5.2.	Deviation comparison and variable selection	110
6.5.3.	GD&T extraction from deviated STL files.....	111

6.6.	Experimental Procedure.....	111
6.7.	Results and discussions.....	114
6.8.	Conclusions.....	120
7.	Conclusions and Future Scope.....	121
7.1.	Conclusions.....	121
7.2.	Future research.....	123
	References.....	124
	Appendix A: GBTA features for normative benchmark.....	134

List of Tables

Table 1. LPBF process stages, significant process parameters, and corresponding geometric deviation modes	7
Table 2. GD&T characteristics, symbols and corresponding descriptions	9
Table 3. Common features used for GB&T characterization in benchmark artifacts	18
Table 4. Comparison of GBTAs according to geometric features evaluated. [DA: Dimensional Accuracy; MFS: Minimum Feature Size; R: Repeatability; SF: Surface Finish; FFA: Fit for assembly evaluation].....	20
Table 5. Brief overview of the relevant literature of LPBF manufactured parts in terms of coverage of material, geometric tolerance, and assembly aspects	25
Table 6. AM features for GD&T characteristics evaluation.....	33
Table 7. AM features for other geometric properties and assemblability evaluation. DOF – degree of freedom.	34
Table 8. Features on the GBTA and corresponding geometric characteristics.....	36
Table 9. Factors and levels table.....	44
Table 10. Tolerance zones for mating features along with IT grades.....	46
Table 11. Signal-to-noise ratio ranking table.....	51
Table 12. Optimal settings table	51
Table 13. Printing Parameters for experimentation	59
Table 14. Mass comparison Table	60
Table 15. Machine Parameters and Manufacturing Parameters for the Experimentation	67
Table 16. Feature categorization based on GD&T characterization.....	71
Table 17. Simulation parameters	74
Table 18. Assembly joints for AM and GBTA features for the same	100
Table 19. Simulation parameters of LPBF process	109
Table 20. LPBF process specifications	113

List of Figures

Figure 1. Generic Steps for the AM Process: from CAD file to the final part	1
Figure 2. Overview of AM output part properties: mechanical, geometric, and surface	3
Figure 3. Depiction of FFF process showing the print bed movability of the extruder in X, Y, and Z direction to fuse the filament into a 3D manufactured part [Gibson et al., 2014].....	4
Figure 4. Depiction of various process parameters commonly used in the parametric studies of FFF process [Rupal et al., 2019].....	5
Figure 5. Schematic depicting the major components of an LPBF process. Adapted from [Zhang et al., 2018]. The Z movement of the powder tank and build piston is also shown.	6
Figure 6. Depiction of a) Flatness and b) Cylindricity tolerance zone	10
Figure 7. Example of benchmark artifacts used for additive manufacturing [Rebaioli et al., 2017]	13
Figure 8. Circle-diamond-square [Moylan et al., 2014]	14
Figure 9. Schematic presenting the linkage between different objectives of the thesis	28
Figure 10. Stage one of geometric benchmarking and GBTA design	30
Figure 11. Stage two of geometric benchmarking and GBTA design.....	31
Figure 12. GE LEAP® aircraft engine bracket (Adapted from Carter and others [Carter et al., 2014]).....	35
Figure 13. a) The hole and pin benchmark artifact depicted in mating condition for the assembly b) The hole and pin benchmark artifact linear dimensions c) Corresponding GD&T characteristics for functionality	42
Figure 14. Relationship between the input and output variables	42
Figure 15. Printed components: ABS, PLA, and Magnetic PLA	44
Figure 16. Dimensional deviation from nominal diameter (mm).....	45
Figure 17. Cylindricity tolerance results (mm) for FFF study.....	47
Figure 18. Flatness tolerance results (mm) for FFF study.....	48
Figure 19. Box and whisker plot for Flatness, Parallelism, Concentricity and FPC average.....	49
Figure 20. Main effects plot for signal-to-noise ratio for percentage cylindricity tolerance.....	50
Figure 21. Main effects plot for signal-to-noise ratio for FPC average.....	50
Figure 22. A flowchart depicting the output property prediction methodology based on the Reverse CAD algorithm.....	54

Figure 23. Theoretical model for the filament as an ellipse	55
Figure 24. The Reverse CAD algorithm	57
Figure 25. a) Cubic Reverse CAD model: isometric and zoomed-in view, b) The printed cubic part: isometric and zoomed-in view, c) Cylindrical Reverse CAD model: isometric and zoomed-in view, d) The printed cylindrical part: isometric and zoomed-in view	61
Figure 26. Geometric deviation analysis for the CAD model vs. Reversed CAD model of the cylindrical part, a) Build orientation 1: cylinder axis aligned to print bed, b) Build orientation 2: cylinder axis parallel to print bed.....	62
Figure 27. Nominal GBTA design and corresponding features. Left: Top view; Right: Isometric view.....	65
Figure 28. a) Isometric view of the GBTA, b) Top view of the manufactured GBTA showing the ‘front side’ of the LPBF system, gas flow direction and recoater direction, and c) Side view of the manufactured GBTA showing the depicting and the base plate.....	68
Figure 29. Measurement strategy for different features. The red dots represent the locations where the CMM probe will record the measurement data.	69
Figure 30. GBTA after the removal of the base plate. a) Isometric view, b) Side view showing warped features	70
Figure 31. a) GBTA with supports (in blue), b) Layer based adaptive coarsening mesh.....	75
Figure 32. Extraction of GD&T a) Construction of fitting feature on deviated STL,	75
Figure 33. von Mises stress distribution of the GBTA with the base plate intact.	77
Figure 34. von Mises stress distribution of the GBTA after removal of the base plate.....	78
Figure 35. Overall deviations of the GBTA with the base plate intact.....	79
Figure 36. Overall deviations of the GBTA after removal of the base plate	80
Figure 37. Straightness tolerance results with and without base plate	81
Figure 38. Flatness tolerance results with and without base plate	83
Figure 39. Circularity.....	85
Figure 40. Diameter vs circularity (Experimental).....	85
Figure 41. Cylindricity.....	87
Figure 42. Diameter vs cylindricity (Experimental).....	88
Figure 43. Perpendicularity.....	89
Figure 44. Parallelism	90

Figure 45. Angularity.....	91
Figure 46. Concentricity	92
Figure 47. Position tolerance (Planar)	93
Figure 48. Position tolerance (Axial).....	94
Figure 49. Circular Runout	95
Figure 50. Total Runout.....	96
Figure 51. Overall schematic of the research approach for GD&T and assembly prediction for LPBF process	99
Figure 52. Pin component (a) and hole component (b) of the ABTA along with the functional dimensions and GD&T characteristics. Units: mm.	102
Figure 53. Zoomed-in view of the hole component of the assembly GBTA to show important dimensions. A unit cell of the simple cubic lattice used in the assembly GBTA is also shown on the right. Units: mm.	104
Figure 54. Usage of supplemental surface for topology optimized flat features. Inset shows the contact points on the surface which are recorded by the CMM probe to measure flatness.....	104
Figure 55. The skin model shapes generation workflow	106
Figure 56. Deformations obtained from the simulation of the LPBF process	110
Figure 57. Depiction of various geometric tolerances for the hole component of the ABTA....	112
Figure 58. Manufactured ABTA on the build plate (a) and removed from the build plate and (b) assembled as per the specified orientation.....	112
Figure 59. Comparison of diameter values from skin model shapes and experimental data for hole component and pin component, where the horizontal red lines indicate nominal dimensions...	115
Figure 60. Comparison of cylindricity tolerance from skin model shapes and experimental data for hole component and pin component	116
Figure 61. Comparison of flatness tolerance from skin model shapes and experimental data for hole component and pin component	117
Figure 62. Comparison of perpendicularity tolerance from skin model shapes and experimental data for hole component and pin component.....	118
Figure 63. Comparison of true position tolerance from skin model shapes and experimental data for hole component and pin component.....	119

1. Introduction and background¹

1.1. Background

Additive Manufacturing (AM) or 3D printing is a rapidly growing manufacturing technology with the potential to manufacture complex geometric shapes with minimum material wastage and with possibilities for new processes, materials, and vast application areas. The first commercial AM system was developed in 1987 by 3D systems [Gibson et al., 2014]. Currently, AM can be used to manufacture a wide range of part sizes and material options ranging from a composite airplane wing to metallic dental implants. A vast number of AM applications like aerospace, automotive, medical, bio-manufacturing, custom, and multi-material components are making the process even more popular and disruptive [Schmidt et al., 2017].

AM includes a few processes under one umbrella that use a layer-by-layer technology, for example, FFF (fused filament fabrication), SL (stereolithography), SLS (selective laser sintering), and LPBF (laser Powder Bed Fusion). The steps of almost all the AM processes are similar due to the commonality of the layer-by-layer material deposition, slicing procedure with .STL file and G-code for path planning. However, the processes differ due to several factors such as physical design, energy deposition method, and the material used [Gao et al., 2015]. The material deposition in AM is opposite to the conventional manufacturing technologies that are subtractive. The basic steps are described in Figure 1.

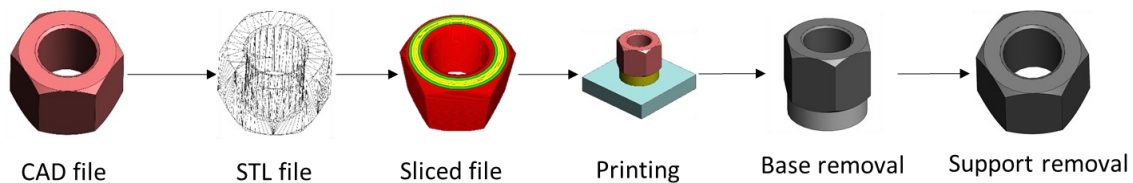


Figure 1. Generic Steps for the AM Process: from CAD file to the final part

¹ Parts of this chapter have been published in:

- B.S. Rupal, A.J. Qureshi, “Geometric deviation modeling and tolerancing in additive manufacturing: a GD&T perspective”, 1st Conference of NSERC Network for Holistic Innovation in Additive Manufacturing (HI-AM), pp. 1-6, May 2018, Waterloo, Canada.
- S.T. Toguem, B.S. Rupal, C. Mehdi-Souzani, A.J. Qureshi, N. Anwer, “A review of AM artifact design methods”, ASPE and euspen Summer Topical Meeting on Advancing Precision in Additive Manufacturing, July 2018, Berkeley, USA.

The AM process starts with the creation of a virtual model of the geometry in CAD software such as SolidWorks or Pro-E. The CAD model is then converted to a file format, which is known to the AM process: usually, STL (standard tessellation language) file format is used. The STL file is then sliced into layers in dedicated software, supports are generated, and process parameters are defined before finally manufacturing the part layer by layer. Some significant process parameters are part orientation, layer height, slicing strategy, and settings related to hardware such as laser power and scanning speed for metal AM processes. In some cases, especially in metal AM, part manufacturing is followed by post-processing steps such as support material removal, removal of the base plate, and special processes to enhance output properties such as surface quality.

There are many AM processes, which are mostly categorized by material type and material joining method. Common AM materials are metals, polymers, and ceramics. The common AM process types are material extrusion, vat photopolymerization, directed energy deposition, and laser powder bed fusion (LPBF) [ISO/ASTM 52900]. Material extrusion or FFF, and LPBF are two of the widely used AM processes. The physics of the AM processes, the steps included, STL file settings, toolpath parameters, process parameters, and material selection all play a large role in deciding the output properties of the final manufactured part. Some of the most important output properties of the AM manufactured parts are shown in Figure 2. The next sections cover the basics of the processes under consideration for this thesis i.e., FFF and LPBF, before moving onto the output properties that are the focus of this thesis.

1.2. AM processes

The two most widely used AM processes in industry and also the processes investigated for this thesis work are FFF and LPBF. FFF is a polymer filament-based process and LPBF is a metal powder-based process. Both processes along with their major process parameters are discussed in the sections below.

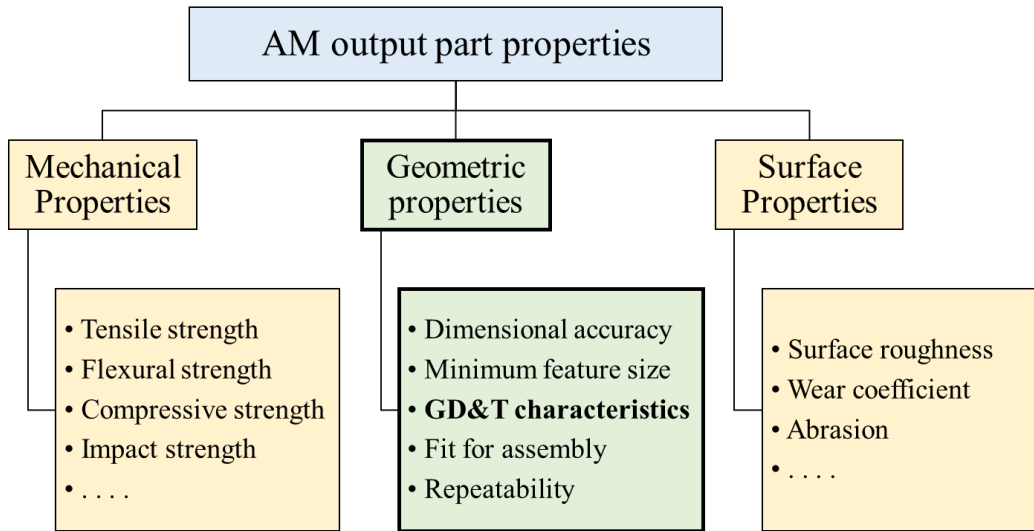


Figure 2. Overview of AM output part properties: mechanical, geometric, and surface

1.2.1. FFF process

The fused filament fabrication (FFF) process or fused deposition modeling (FDM) process involves converting the CAD model into a tessellated file format, which facilitates slicing the model into layers. The slicing is done by dedicated computer-aided manufacturing (CAM) based software before the file is converted to a toolpath. Finally, the material (in filament form) is extruded on the print bed according to the prescribed toolpath to fabricate the part. The range of materials and printed part sizes is rather vast, ranging from simple polymers such as Nylon-12, Polycarbonate (PC), and Acrylonitrile Butadiene Styrene (ABS), to highly sophisticated and high-strength materials like carbon fiber or metallic composites, including special purpose materials. The major process parameters include the STL file resolution, slicing parameters, and machine parameters such as the bed temperature, and extruder speed [Singh et al., 2020]. Figure 3 shows a schematic of the FFF process with the extruder, fused filaments in the shape of the input CAD, and the moveable print bed.

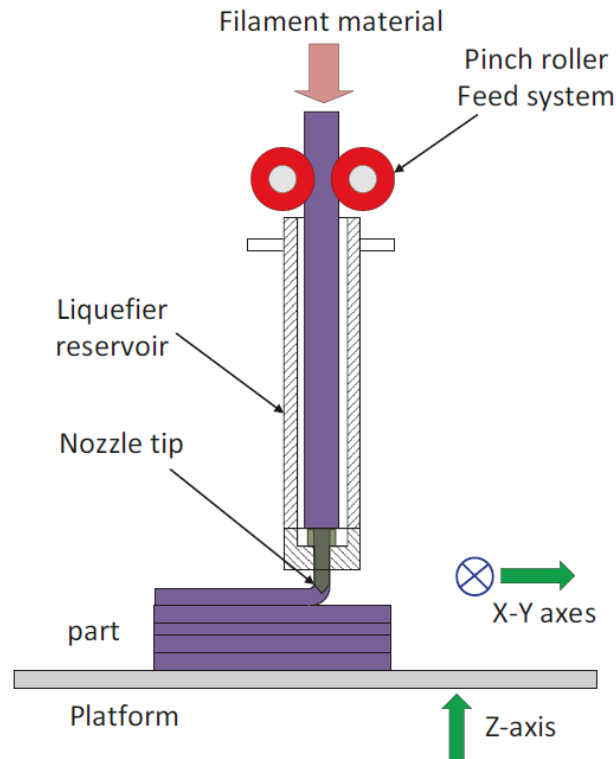


Figure 3. Depiction of FFF process showing the print bed movability of the extruder in X, Y, and Z direction to fuse the filament into a 3D manufactured part [Gibson et al., 2014]

The important FFF parameters are shown in Figure 4 and explained below:

- Filament diameter: The diameter of the input filament used for the process
- Infill density: The percentage measure of the area of the layer to be printed to the total area of the layer.
- Number of contours: Number of boundaries around each layer to increase the stability and mechanical behavior of the part.
- Raster angle/orientation: Angle between one of the axes and the direction of the raster.
- Raster pattern: There are two types of raster patterns – sparse and double sparse. In sparse patterns, the orientation or the raster angle remains the same for all layers. For double sparse patterns, the raster angle shifts by 90° after each layer.
- Number of shells: Number of upper and lower covers (surfaces) with 100% infill density to make the part solid even if it has less infill density inside.

Due to several unknown variables and process parameters, challenges arise in achieving the desired geometric and mechanical properties of the FFF manufactured components.

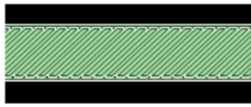
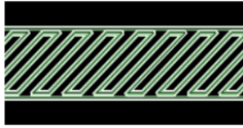
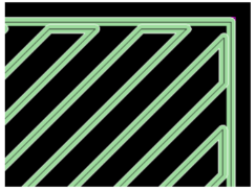
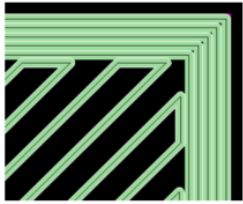

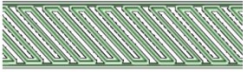
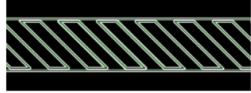
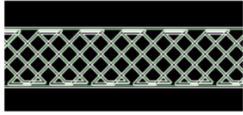
Infill density	 100%	 50%
Number of contours	 One contour	 Five contours
Raster angle	 0°	 45°
Raster pattern	 Sparse	 Double sparse

Figure 4. Depiction of various process parameters commonly used in the parametric studies of FFF process [Rupal et al., 2019]

1.2.1. LPBF process

LPBF is a metal powder and laser-based AM process. The basic components of an LPBF process are shown in Figure 5. The process stages, typical process parameters, along with corresponding deviation modes is shown in Table 1. Metal powder with a particle size ranging from a few microns (usually 15-45 μm) is used as the raw material for manufacturing. The powder is stored in the powder tank and is moved into the powder bed when the manufacturing process starts, using the recoating blade. The build piston moves ‘one layer’ height down and the recoater fills in the powder on the bed. The recoating blade makes sure that the powder is spread evenly on the powder bed with the required layer thickness. After one layer of powder is spread, the laser moves over the area that needs to be melted as per the part geometry for that layer. The laser movement is controlled by scanner mirrors, which use information from the cross-section geometry of each

layer. The melted, fused powder cools to form a solid metal layer. The layer addition procedure continues until the required geometry is formed. The manufactured part is then left to cool off for a few hours and removed from the powder bed.

For the manufacturing of the first layer, a solid metal base plate is bolted to the powder bed, which is lowered as the part is being manufactured. The support structures also originate from the base plate, which is used to support the features on the part structurally. The manufactured part characteristics (geometric, mechanical, and surface) are dependent on the various process parameters throughout the LPBF process discussed above. Process parameters for the LPBF process and corresponding geometric deviation modes are shown in Table 1

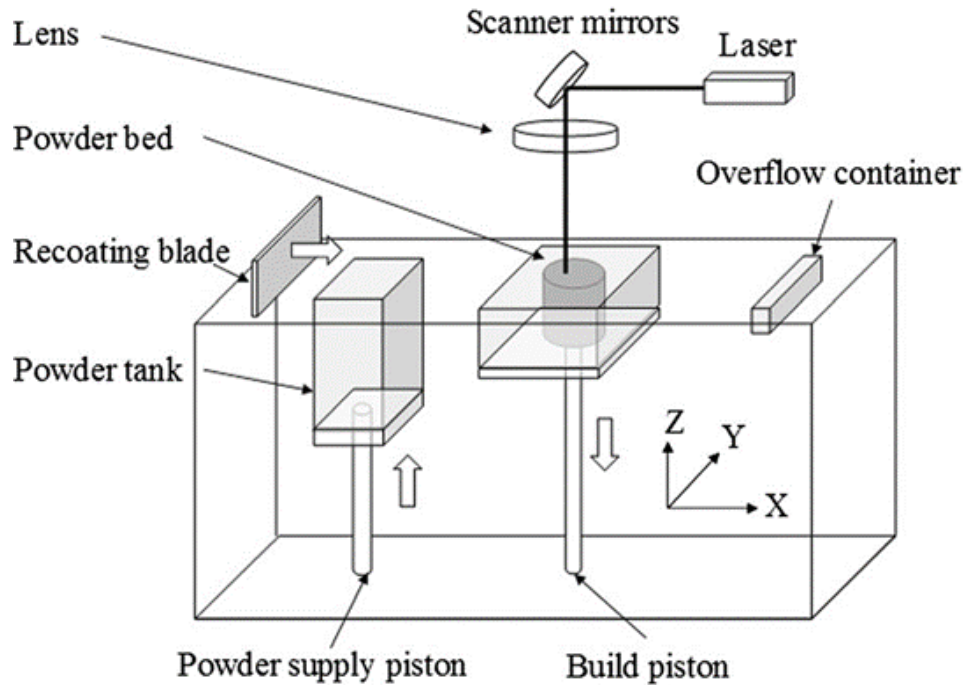


Figure 5. Schematic depicting the major components of an LPBF process. Adapted from [Zhang et al., 2018]. The Z movement of the powder tank and build piston is also shown.

Table 1. LPBF process stages, significant process parameters, and corresponding geometric deviation modes

Process Stage	Process Parameters to reach the Stage (List not exhaustive)	Corresponding Deviation Mode
Pre-processing	STL Settings: - Angle Deviation - Tolerance Deviation	CAD to STL Mode
	Slicing parameters: - Part Orientation - Hatch Style - Layer Height	Slicing Mode
Part Manufacturing	Process Settings: - Laser Power - Bed Temperature	Thermo-mechanical Mode
Post-processing	- Base Plate Removal	Base Removal Mode
	- Support Structure Removal	Support Removal Mode





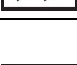




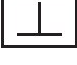




1.3. Geometric properties and GD&T

A significant barrier to AM process industrialization is the difficulty in predicting the output properties before manufacturing the part. This pre-processing prediction and evaluation are of extreme importance in cases where large-sized parts are needed, high-cost materials are used, many parts are needed, or financial constraints exist. Moreover, it gives the designer and customer a means to understand and estimate the output part properties so that both parties can reconsider the part design if it does not meet the required criteria. Currently, most of the industries rely on the experience of the operators, analytical models, data-driven methods, experimentation, trial & error to estimate the output properties of the manufactured part. This practice is usually followed for subtractive manufacturing processes and has made its way onto AM as well.

The geometric properties of the AM manufactured part is one of the most important characteristics to evaluate as it is critical to assess the part selection or rejection. Geometric properties of a part in the advanced manufacturing industry, is standardized via an ISO standard

i.e. ISO 1101 [ISO 1101, 2017], simply referred to as GD&T (Geometric Dimensioning and Tolerancing). GD&T is a geometric language that offers a method of dimensioning and tolerancing the CAD model or the manufactured part using various characteristics to define the form, position, location, and orientation of the features on a specific part and how they relate to the assembly later. There are total 14 GD&T characteristics, which can be used interchangeably to define the geometric characteristics of a feature completely. The GD&T characteristics are defined as per 'ISO 1101: 2017' and are explained briefly in Table 2. The most commonly used GD&T characteristics are flatness and cylindricity, which define the form characteristics of a flat feature and a cylindrical feature respectively. Figure 6 a) shows a flat surface with a flatness value of 0.3, which means that all physical points on the surface lie in a dimensional band of 0.3 mm as shown, using the perfect two planes on the top and bottom of the surface with a gap of 0.3 mm. Similarly, Figure 6 b) shows a cylindricity tolerance band using two concentric cylinders which enclose all physical points on the periphery of the cylinder. For functional features as well as for features that have to be used as mates in an assembly, quantifying the GD&T characteristics is crucial to ensure proper part functioning and for the fitting/working of the assembly.

Table 2. GD&T characteristics, symbols and corresponding descriptions

GD&T characteristic symbol	Control type	Name	Summary Description
	Form	Straightness	Controls the straightness of a feature in a relation to its own perfect form
	Form	Flatness	Controls the flatness of a surface in relation to its own perfect form
	Form	Circularity (Roundness)	Controls the form of a revolved surface in relation to its own perfect form by independent cross-sections
	Form	Cylindricity	'Circularity' applied to the entire revolved surface
	Profile	Profile of a line	Controls the size and form of a freeform feature. Also controls the location and orientation when a datum reference frame is used
	Profile	Profile of a surface	'Profile of a line' applied to the complete feature surface
	Orientation	Angularity	Controls orientation of a feature at a specific angle in relation to the primary datum of its datum reference frame
	Orientation	Perpendicularity	Controls the orientation of a feature that is nominally perpendicular to the primary datum of its datum reference frame
	Orientation	Parallelism	Controls orientation of a feature that is nominally parallel to the primary datum of its datum reference frame
	Location	Position	Controls the location and orientation of a feature in relation to its datum reference frame
	Location	Concentricity	Controls concentricity of a surface of revolution to a central datum
	Location	Symmetry	Controls the symmetry of two surfaces about a central datum
	Runout	Circular Runout	Controls circularity and coaxiality of each circular segment of a surface independently about a coaxial datum
	Runout	Total Runout	Controls circularity, straightness, coaxiality, and taper of a cylindrical surface about a coaxial datum

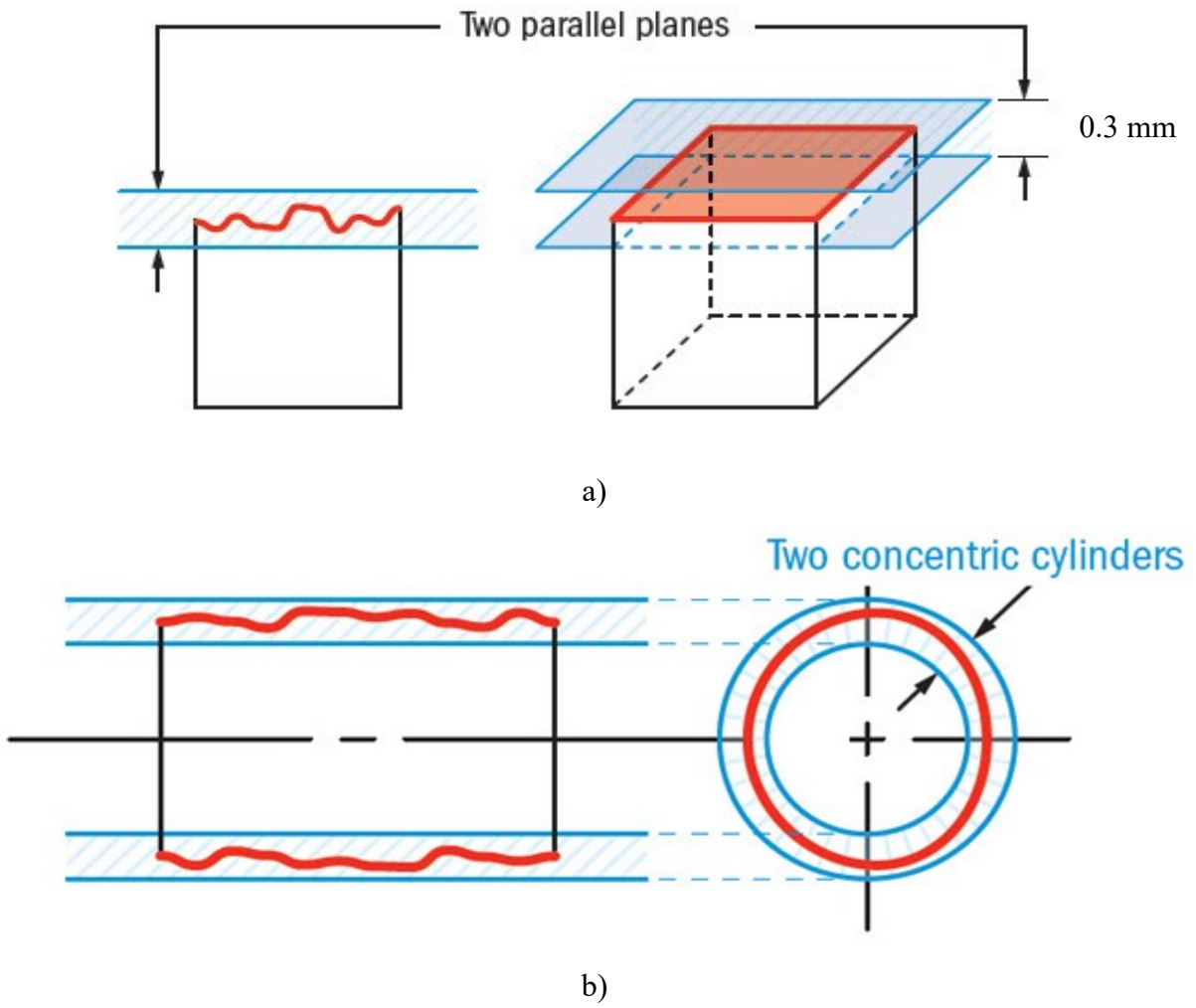


Figure 6. Depiction of a) Flatness and b) Cylindricity tolerance zone

1.4. Motivation

AM is a fast-growing manufacturing process but still needs improvement to make it a reliable advanced manufacturing technology [Rajaguru et al., 2020]. The manufactured part's output properties are of paramount importance and hence need research focus to make sure that the manufactured parts adhere to design specifications. The output part properties of an AM process can be categorized as follows:

- Mechanical properties such as tensile strength and flexural strength.
- Surface properties such as surface roughness and wear properties.
- Geometric properties such as dimensional accuracy, minimum feature size, repeatability, and fit for assembly.

These part properties are dependent on the various process parameters throughout the AM process discussed above. The standardized methods are already present for mechanical and surface quality estimations [Mahmood et al., 2017; Garcia et al., 2017, Barari et al., 2017]. Currently, the major challenge is the quantification and prediction of geometric characteristics [Shahrain et al., 2016; Rebaioli et al., 2017]. The input CAD file dimensions and final part dimensions or form are never the same. Due to the various process parameters and manufacturing conditions that give rise to 'geometric deviations' or 'geometric errors' need to be quantified and assessed in advance, to ensure the required geometric characteristics of the AM part.

An AM standard [ISO 17296-3, 2014] specifies the need to follow geometric characteristics which should be measured, quantified, and controlled to ensure the geometric quality of an AM part:

- Size, length, angle dimensions, and dimensional tolerances
- Geometrical tolerancing (deviations in shape and position)

These characteristics are defined and controlled by GD&T. A major concern for AM is that the geometric deviation models, process-based geometric models and thermo-mechanical deviation models solved using finite element methods (FEM), are limited to individual deviation mode assessments and part orientation optimization [Paul et al., 2014]. The absence of GD&T-based total geometric characteristic quantification and assessment for metal AM presents a significant barrier to its use as a reliable advanced manufacturing process.

GD&T-based geometric property assessments should enable designers and manufacturers to reliably quantify geometric characteristics, thereby enabling the quantification of geometric

deviations in terms of various GD&T characteristics of functional features. Based on that, the process capability index for various GD&T characteristics could provide estimations of the geometric properties of the part to be manufactured, considering parametric variations. Moreover, GD&T-based geometric deviation models could standardize the thermo-mechanical based simulation models of the AM process in consideration.

This thesis aims to develop a framework for quantification and prediction of geometric tolerances for AM processes using experimental and simulation methods as per geometric standards, i.e. GD&T characteristics. In the next section, relevant state-of-the-art methodologies and their limitations are discussed followed by detailed research objectives.

1.5. State-of-the-art

The literature review is divided into subsections to cover the relevant background in geometric characteristic assessment for AM. In literature, geometric property quantification and prediction falls into the pre-processing analysis step which is generically classified into three methods:

1. Performing designed experiments using some pre-selected benchmark artifacts and making meta-models that can predict the geometric capability of the AM process and, hence, the geometric properties of the parts to be manufactured [Shahraïn et al., 2016].
2. Analytical modeling of the specific AM process based on the thermo-mechanical interactions. These models are then used to predict the effect of the AM process on the output properties. The models are later validated using benchmark artifacts [Aboutaleb et al., 2017].
3. A hybrid compensation model based on thermo-mechanical simulation complemented by designed experiments with benchmark artifacts to have statistical data. These models usually separate out the systematic and non-systematic effects of the process on the output properties and generate a predictive tool for performance evaluation [Dantan et al., 2017].

In all the above-mentioned methods, benchmark artifacts are used to predict, model, or evaluate the geometric performance characteristics of the AM part. In the last decade, many different benchmark artifacts were designed and used to evaluate the geometric performance of AM parts. Benchmark artifacts give specific information on geometric metrics like GD&T characteristics, dimensional accuracy, minimum feature size, repeatability, and surface finish.

In the sub-sections below, first, the various experimental methods based on benchmark artifacts are discussed from a standpoint of benchmark artifact design criteria. Then, analytical and

thermo-mechanical models used for the prediction of AM part deviations are discussed. Finally, research objectives of this thesis are formulated based on research gaps found in the literature study.

1.5.1. Benchmark artifact design process

A benchmark artifact usually consists of some geometric features with different intended purposes placed on a common base as shown in Figure 7. Benchmark artifacts are designed for manufacturing processes performance evaluation. Using benchmark artifacts for performance evaluation is neither a new practice nor unique to manufacturing. In 2D graphic printing, test targets are usually used for systems performance evaluation with the purpose of calibration and optimization to fit the functional requirements. Many artifacts for additive manufacturing are inspired by 2D printing test targets [Chang et al., 2015]. Also, in the metal cutting machining domain, there exist several artifacts for machine characterization. One of them named “circle-diamond-square” is quite widely used and it is shown in Figure 8. It was developed in 1966 for performance evaluation of Computer Numerically Controlled (CNC) machining centers [Moylan et al., 2014] and has inspired the design of many artifacts for additive manufacturing.

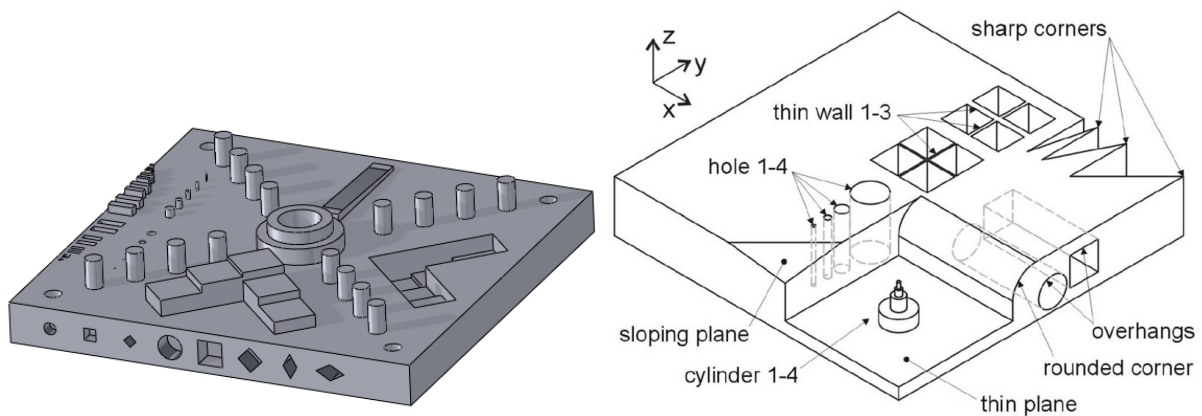


Figure 7. Example of benchmark artifacts used for additive manufacturing [Rebaioli et al., 2017]

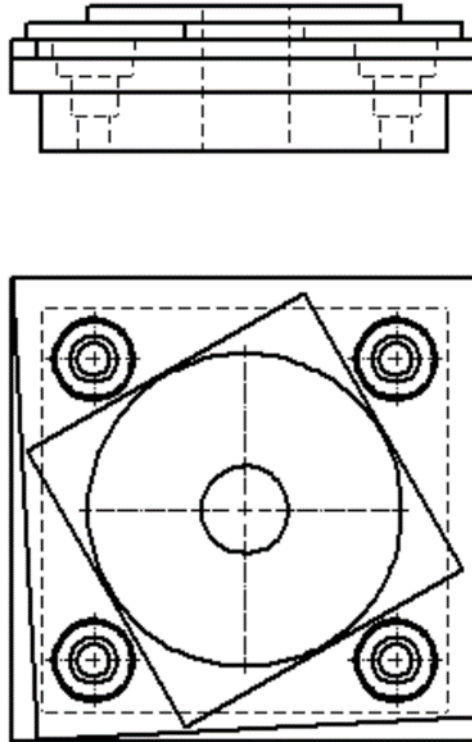


Figure 8. Circle-diamond-square [Moylan et al., 2014]

To understand the applicability of the benchmark artifacts for performance evaluation it is important to discuss their design methodology. Some research articles and review papers have provided useful insights [Moylan et al., 2014; Rebaioli et al., 2017]; however, none has explicitly examined and compared AM artifact design approaches, even though the final artifact depends on the design approach, criteria and constraints definition as well as the overall design methodology. In addition, discussing AM artifacts design methods could provide insights into differences between final artifacts because there are different approaches for artifacts design in the literature. According to Rebaioli et al. [Rebaioli et al., 2017], the first and most commonly used approach is based on the criteria defined by Jacobs and Richter which focuses directly on the features of the test parts and their shapes when defining AM design criteria and constraints. Many test parts have been designed based on this approach, others are inspired by existing artifacts in other fields such as (2D graphic printing, and CNC). More recently, the approach proposed by NIST in 2014 [Moylan et al., 2014] has also inspired many artifact designs. There are also communities which design artifacts and make them available on websites. This literature survey presents the main existing artifacts and for each the aim is to give answers to the following questions:

- Why was the artifact designed for?
- What is the design approach?
- What are the design criteria considered?
- What are the constraints and the importance of each?
- What are the difficulties faced during the design process?

Besides GD&T accuracy evaluation, AM artifacts can be used for mechanical properties characterization (where important results are already available) and process parameters optimization/comparison (e.g., with the aim to improve the design for AM or DFAM), but this thesis only deals with test artifacts which characterize GD&T accuracy evaluation, repeatability, and minimum feasible size/resolution of systems/processes with fit for assembly considerations. Common design approaches for additive manufacturing benchmark artifacts are discussed below.

Like for most products design, AM benchmark artifact design usually begins by requirements and constraints definition. The design process then aims to find solutions satisfying the design requirements and constraints. Thus, in the literature, AM benchmark artifact design usually starts by criteria definition and each criterion is implicitly translated into design requirements. Many criteria have been defined for AM benchmark artifact design, some of them have been enhanced and completed over time. Solutions to GD&T requirements are usually represented by features (simple or complex). There are common features that repeatedly appear in the majority of existing AM benchmark artifacts.

On the other hand, a few numbers of AM benchmark artifacts design are based on actual parts by building them directly for AM system's performance evaluation. For instance, the first AM artifact was designed basing on real objects, but the result was a limited test part unable to efficiently characterize and evaluate specific AM systems/processes characteristics and performances. As previously mentioned, there are also artifacts designed basing on practices in other fields (2D printing test targets, metal cutting machining test parts).

There are two main tendencies in AM artifact design criteria/constraints definition. The first is to base on criteria defined by Jacobs & Richter and the second (and most recent) on the ones defined by Moylan and others [Moylan et al., 2014]. Several artifacts have been designed according to Jacobs & Richter's design criteria defined as follows:

- Should be large enough for performance evaluation in all the building surface (center and edges),

- Should include small, medium, and large common features (cubes, thin walls, and cylinders),
- Features should be both positive and negative (inside and outside features),
- The test part should not be time consuming at the building stage,
- Should not be material consuming,
- Should be easily and quickly measurable,
- And should include enough features.

These criteria have been further completed by Byun and Lee [Byun and Lee., 2003] who noted that features of an ideal artifact should also be aligned along all the axes and provide information on the minimum feasible feature/resolution of the AM system/process and by Scaravetti [Scaravetti et al. , 2008] who stated that a suitable artifact should require neither post treatment nor manual interventions, allow evaluation of spatial repeatability and most importantly should help in linking systems/processes errors with their causes. Further, Mehdi-Souzani and others [Mehdi-Souzani et al., 2017], stated that AM artifacts should also include complex features to represent complex forms achievable by AM systems/processes.

Moylan and others [Moylan et al. 2014] presented a set of AM artifacts design criteria. For demonstrating capabilities and limitations of AM systems/processes, general criteria that are not specific to systems/processes and thus not directly related to systems/processes characteristics have been defined as follows: the test part should provide information on the system's abilities to produce real world parts, also to create canonic forms (straight, circular, and arced features) and orientations (parallel, perpendicular and inclined features), the test part should provide information on the dimensional accuracy of the system (ability to produce features with the correct indicated size and in the correct location, the feature minimum size that can be produced) and finally, the test part should help in evaluating the system capabilities to create both cavities and bosses features. For identifying and quantifying systems errors, a number of criteria specific to powder bed fusion (PBF) systems were proposed: the test part should be designed to identify and quantify alignment errors between axis, geometric errors in laser positioning and axis positioning the building platform.

Several AM artifacts have been designed based on previously defined design criteria. However, design constraints considered for each artifact are usually different and this can significantly affect the final test part. AM Artifacts Design Constraints: Design constraints represent limits that must be overcome during the design process and the life cycle of the product

to fit the requirements/criteria. In the literature, AM artifact's design constraints are usually about measurements (system, methods) and building of the part (system characteristics, process). Measurements constraints are usually about measurability of the test part either by one of commonly used measurement systems (contact or non-contact) or by all of them. It also concerns data collected during measurements that needs to be repeatable and reliable. This depends on the type of features of the artifact, their accessibility, their arrangement, the usage or not of support structures and their sizes. The thickness of the base feature of the artifact also plays important role here, as a thick base feature leads to unnecessary warpage, and hinders with the measurement repeatability of the geometric tolerances of the features on the base feature. Measurements constraints are also about ability of artifacts to be easily characterized by standard measurement methods.

Other main design constraints are building constraints related to system/process characteristics and parameters. This is about system/process capabilities in terms of building strategy and even building surface dimensions. Another constraint is about support structures and post treatments which are usually minimized during the building of the artifact to avoid and minimize measurement errors and human intervention. As mentioned by Umaras and others [Umaras et al. 2017], there are errors that can be anticipated and compensated by the designer when knowing the characteristics of the intended manufacturing process during the 3D CAD test part creation such as file conversion errors - from CAD to STL, AMF, STEP, STEP NC, 3MF, VOXEL BASED format depending on the process used, which vary from one file to another. As clearly demonstrated by Calignano and others [Calignano et al. 2017] the destination file type can significantly affect geometric accuracy of the AM system/process depending on the file conversion parameters. This constraint is not widely considered and has been ignored in benchmark artifact designs.

The selection of AM artifact features generally begins by the overall dimension definition. Knowing that artifacts should evaluate system/process accuracy within all the building surface and should be measurable by existing measuring systems, artifact's base dimensions usually consider the build platform size, and the measurement surface dimensions to be replicated at different building platform locations. After that, features are chosen according to the GD&T characterization (e.g., for flatness, choose cubes, slots, rectangular bosses, and thin walls) and GD&T allocations are done. Primitive features are likely to be used because they avoid CAD errors

and reduce file conversion errors. They also allow quick visual inspection especially for form inspection. Common features used for GB&T characterization in benchmark artifacts are shown in Table 3.

Table 3. Common features used for GB&T characterization in benchmark artifacts

GD&T	Feature(s)
Flatness	Base surface, cube, Flat beam, slots
Straightness (internal/external linear accuracy)	Square hole, cube, Square, Base surface, Flat beam, slots, Brackets
Circularity (internal/external)	Cylindrical hole, cylinder
Parallelism	Square hole, square, cube
Perpendicularity	Square hole, Square
Angularity	Inclined feature, Brackets
Position	Holes, cylinders
Profile	Cones, spheres, hemispheres
Surface roughness	Base surface
Cylindricity (internal/external)	Cylindrical hole, cylinder, hollow cylinders
Sphericity	Sphere
Concentricity	Cylindrical hole
Thickness (small linear accuracy)	Wall, Hollow squares
Minimum feasible size	Fine features
Repeatability	Repeated features (e.g., Cube, cylindrical holes, spheres, cylinders)
Overhang	Flat beam

Further, most of the mechanical components and assemblies are based on primitive feature. To summarize, to propose a new test part, features are chosen according to a set of design criteria and arranged on a base surface. The commonly accepted criteria for artifacts design were the ones defined by Jacobs and Richter and enhanced later. Simple geometrical features are used (cylinders, holes, wall, and cones) as well as complex (freeform) features. A general method for features

arrangement is proposed by Byun and Lee [Byun and Lee, 2003]. Many test parts do not consider fit for assembly criteria as well as digital chain errors constraints (more than 80% of the examined literature).

To extract the geometric metrics, differentGBTAs use various types of primitives like cubes, cylinders, pins and holes, stairs, thin walls, oriented geometries and even freeform surfaces [Mehdi-Souzani et al., 2017]. There are many researches describing the experimental results using geometric benchmark test artifacts (GBTAs) to characterize the geometric tolerance of the AM systems under consideration. One of these studies [Mahmood et al., 2018] considered a GBTA with a cubical base and some cylindrical and prismatic features on the top. It was used to characterize the dimensional and geometric accuracy of the FFF process. Taguchi's design of experiments method was used to optimize 13 process parameters for geometric tolerance in terms of linear dimensions and various geometric tolerances such as cylindricity and flatness. Similarly, numerous other studies [Shahrain et al., 2016; Mostafa et al., 2017; Moylan et al., 2014] used different types ofGBTAs to characterize and improve the geometric tolerances of various AM processes such as FFF, Vat photopolymerization, and laser powder bed fusion (LPBF). There is no doubt in the fact that the complete geometric property evaluation of any manufactured part is incomplete without GD&T characterization [Cogorno, 2020]. However, it is interesting to note that out of a large number ofGBTAs available, only a small number ofGBTAs claim to provide information on GD&T characteristics, and even in these cases incomplete information is given. A comparative analysis of theseGBTAs according to the geometric properties evaluated is shown in Table 4. The table segregates theGBTAs based on how many GD&T characteristics its features can quantify, and also other important geometric properties, such as dimensional accuracy, minimum feature size, repeatability, surface finish, and fit for assembly. The table shows that most of the genericGBTAs lack in terms of quantifying GD&T characteristics and in providing holistic geometric capability about the AM process in consideration.

Table 4. Comparison ofGBTAs according to geometric features evaluated. [DA: Dimensional Accuracy; MFS: Minimum Feature Size; R: Repeatability; SF: Surface Finish; FFA: Fit for assembly evaluation]

Reference	GD&T characteristics	DA	MFS	R	SF	FFA	Comments on GBTA design
[Mahesh et al., 2004]	Roundness, cylindricity, sphericity, Flatness, concentricity, squareness, symmetry, coaxiality, perpendicularity, angularity, parallelism	✓	✗	✓	✓	✗	<ul style="list-style-type: none"> • Designed for comparison of different AM processes with different process and toolpath parameters. • Warpage of the base plate studied by changing parameters based on experience, no specific feature designed for that.
[Hanumaiah et al., 2007]	Straightness, flatness, circularity	✗	✗	✗	✗	✗	<ul style="list-style-type: none"> • Eight different samples regarded as one GBTA • Manufactured in different batches (potential source of error)
[Cooke et al., 2010]	Flatness, squareness, parallelism, circularity	✓	✗	✗	✓	✗	<ul style="list-style-type: none"> • Positional error is observed in all features • Lack of process-specific pre-processing analysis
[Saqib et al., 2012]	Flatness, cylindricity, perpendicularity	✗	✗	✗	✗	✗	<ul style="list-style-type: none"> • Very simple test part to access three GD&T features • Logic can be extended to other geometric features too
[Moylan et al., 2012]	Straightness, flatness, roundness, cylindricity, perpendicularity, parallelism, profile, concentricity	✓	✓	✓	✓	✗	<ul style="list-style-type: none"> • Widely accepted NIST standard test artifact (generic in nature) • Process specific geometric evaluation requirement ignored
[Yang et al., 2014]	Straightness, parallelism, flatness, position	✗	✓	✗	✓	✗	<ul style="list-style-type: none"> • Relation between process capability and geometric features considered • Process specific GBTA design

[Shahrain et al., 2016]	Flatness, straightness, circularity, perpendicularity, parallelism, angularity, concentricity, position	✓	✗	✓	✗	✗	<ul style="list-style-type: none"> • Considered process and toolpath parameters and designed experiments for the same • Part scalability and assembly considerations not considered
[Han et al., 2018]	Straightness, Flatness, Roundness, Concentricity, Total runout	✓	✗	✓	✗	✗	<ul style="list-style-type: none"> • Surface roughness and topographies measured • Geometry linked to scan strategy • Focussed on flat features only
[Fahad et al., 2017]	Flatness, cylindricity, true position	✓	✓	✓	✗	✗	<ul style="list-style-type: none"> • Parts stacked, not ideal for repeatable results • Geometric tolerances not studied even when the features are present such as cylindricity
[Toguem et al., 2020]	Straightness, flatness, roundness, cylindricity, perpendicularity, parallelism, angularity, profile, concentricity, position	✓	✓	✓	✗	✗	<ul style="list-style-type: none"> • Directional true position not studied • Scalability issue • Feature accessibility issue

As seen in the above table, and from the discussion on previously developed GBTA designs, it is observed that researchers have aimed at developing a generic GBTA for all geometric characteristics common to all AM processes. However, even the most-widely used genericGBTAs are not holistic in nature and all of them lack fit for assembly evaluation. A generic GBTA is not advisable as the GBTA feature definition, size, orientation, and features need to be designed according to the thermo-physical mechanism and the process and toolpath parameters of the AM process under consideration. For example, the error generated by misalignment of motors and the linear slides in FFF process is not present in digital light processing or laser-based AM processes. Therefore, it becomes important to check GD&T characteristics like circularity and cylindricity tolerances on FFF based AM processes for quantifying the in-built geometric errors, which are systematic in nature. Similarly, other process differences lead to the notion that using the same GBTA for different AM processes is not advisable. Moreover, the same AM process with different process and toolpath parameters will lead to conditions which cannot be evaluated by genericGBTAs. Further, tolerances like the profile of a surface and true position, which is important for freeform surfaces and assemblability, are rarely considered in existingGBTAs. These facts specifically suggest that a generic GBTA can only give a high-level overview and tolerance ranges for an AM process. However,GBTAs should be specifically designed according to the geometric requirement and/or the application in consideration. In general, lack of a systematic design approach for feature selection and a focus towards a generic GBTA are the reasons for the design of manyGBTAs. Moreover, the inability of the majority of theGBTAs to give information about the form, profile, and location GD&T characteristics, assembly consideration, fit for assembly evaluation, and the arbitrary selection of features on the GBTA creates a research gap that this thesis proposes to fill.

Assemblability is the ability of the part to assemble with a mating part and to perform a specified function. Assemblability largely depends on the geometric tolerances of the mating parts [Morse et al., 2018] which need to be controlled not only from the size point of view but also from the shape and orientation perspective. However, GBTA studies to date have not conducted assembly-based experimentation on AM processes. Some studies have explored the DfAM for assembly designs [Sossou et al., 2018] using benchmarks, outlining the generic assembly conditions and constraints for AM parts and assemblies, common assembly joints in AM, their possible fits, and orientation strategies. However, they have not explored the geometric tolerance

of mating features, and manufacturing assemblability of the manufactured parts, which is also an open research area. This thesis aims at studying the necessary process parameters for achieving a specified geometric tolerance and, in turn, ensuring assemblability for AM parts using experimental and process modeling methods. The following subsection briefly outlines the recent research into modeling methods for geometric tolerance modeling for AM processes.

1.5.2. Modeling for geometric tolerances

Contrary to the experimental methods, the process modeling methods aim at understanding the thermo-mechanical interactions and parameters to predict the possible deviations and improving geometric tolerance characteristics of the part to be manufactured. There are several methods that lead to prediction of deviations:

1. Inspecting and improving the input file
2. Using macro-scale thermo-mechanical simulations
3. Statistical methods for prediction the tolerances

First method is focused on using the input STL file to make the process error-free so that it can lead to a better geometric tolerance. Different file formats and improvement algorithms are introduced to do the same. Few research papers [Navangul et al., 2013; Paul et al., 2015; Dantan et al., 2017] presented methods to perform pre-processing estimation of the geometric tolerance, however, most of these methods are applied and tested on polymer-based processes as they are more open architecture and enable changes in the file formats and slicing methods. Although these methods can be applied on FFF process, none of them leads to generic or feature based GD&T and assemblability quantification or prediction. Further, these methods do not consider the high-temperature gradients and the corresponding energy-material interactions and their effects on geometric tolerances, which makes them useless for processes which have high energy sources such as metal AM processes based on laser power.

For laser-metal based AM, the energy-material interactions lead to material shrinkage, changes in microstructure, and residual stresses, therefore significant deviations from the nominal geometry of the part are expected [King et al., 2015]. Changes in process parameters lead to changes in cooling time, microstructure, and eventually, affect the stresses and hence the geometric accuracy. Extensive and dedicated studies of the effect of process parameters affecting, solidification, microstructure and residual stress and as a result, the manufacturing feasibility and

dimensional integrity on a material level have been performed by various authors and can be found in literature for a variety of materials [Yang Y. P. et al., 2018; Barros et al., 2019]. Even if the process parameters are optimal for a given material and stresses are below the yield stress, internal stresses still present from the macroscopic manufacturing process result in deviations which require attention for specification conformance of a given geometry. Moreover, as the part is removed from the base plate and the support structures, it releases the residual stress leading to further geometric deviations [Luo et al., 2018]. Geometric deviations due to material shrinkage and residual stresses depend not only on the material microstructure, and the solidification process, as investigated in the materials-oriented research cited above, but also on the geometry and manufacturing process, and therefore, the development of predictive models that can be used to estimate such deformations for different materials is of paramount importance to material and process parameter selection. Table 5 presents an overview of a recent literature in terms of the different coverage of the material, geometric tolerance, and assembly aspects of the LPBF processes. A lot more publications can be found in literature with focus leaning towards materials and mechanical properties but lacking a detailed analysis on geometric tolerances and assemblability.

Macro-scale finite element (FE) thermo-mechanical simulations are commonly utilized to predict the residual stresses [Peng et al., 2018-I; Peng et al., 2018-II]. The results of the numerical simulations lead to strain and stress maps and the residual stress regions in the geometry to be manufactured. These results lead to localized deviation information, i.e. point to point distortion/displacement maps using color scales to get a generalized idea of the regions with higher deviations. However, these methods have not been extended to quantify geometric tolerances and assemblability. Furthermore, thermo-mechanical models have their own limitations, such as long computation times, difficulty in modeling the complete CAD model with support structures, and prediction accuracy [Luo et al., 2018; Schoinochoritis et al., 2017].

Table 5. Brief overview of the relevant literature of LPBF manufactured parts in terms of coverage of material, geometric tolerance, and assembly aspects

Ref.	Micro Structure evaluation	Parametric variations	Mechanical properties	Residual stresses	Macro Scale Deviations	Geometric Tolerance	Assemblability
[Yang H et al., 2018]	✓	✓	✗	✗	✗	✗	✗
[Yi et al., 2019]	✓	✓	✓	✗	✓	✗	✗
[Lu et al., 2015]	✓	✗	✓	✓	✗	✗	✗
[Nadammal et al., 2017]	✓	✓	✗	✓	✗	✗	✗
[Song et al., 2019]	✗	✓	✗	✓	✗	✗	✗
[Mishurova et al., 2018]	✓	✓	✗	✓	✓	✗	✗
[Jia et al., 2014]	✓	✓	✓	✗	✗	✗	✗
[Cheng et al., 2016]	✗	✓	✗	✓	✓	✗	✗
[Yang Y. P. et al., 2018]	✓	✓	✓	✓	✓	✗	✗

Another set of process modeling methods use a statistical approach to predict the deviations. In this case, random deviations are used to predict the process deviations mathematically and then extrapolate the mathematical model for predicting the geometric tolerance of the parts to be manufactured. In a similar study [Huang et al., 2018], a method was presented for segregation of error modes throughout the process chain of AM and then modeling them individually and lumping the errors along with random errors to generate a predictive shape of the part to be manufactured. The method does not use a classification of the modal errors and is limited to only FFF processes as the modes are specific to the process. No similar study was found considering the effect of thermo-mechanical interactions prevalent in the metal AM processes leading to large geometric deformations. A set of research articles [Huang et al., 2014; Huang et al., 2015; Luan and Huang, 2015] focused on modeling the in-plane shape deviations caused by shrinkage along the part boundary. In this case, shrinkage is modelled as a parametric function proportional to the difference between the actual and nominal shape. The usage of the models is dependent on the experimental data as it deduces information in terms of principal components. Usually, these methods are tested on regular geometries, i.e. bulk solids. In LPBF, bulk solid parts also experience large deviations, cracks, and part failures [Li et al., 2015]. However, in most cases the parts are topology optimized for functionality and weight minimization, and therefore usually include lattice cells rather than bulk solids. The optimized and latticed geometries also need residual stress management to ensure specification conformance and functionality [Vilardell et al., 2019]. In another work [Moroni et al., 2017], a voxel-based representation was used to model the part geometry and to conduct a volumetric based tolerance analysis to achieve the required geometric specifications. The method highlights the need for conducting geometric tolerance assessment based on international standards, i.e., ISO 1101 and ASME Y14.5 [ASME Y14.5, 2019].

Numerical simulation based and statistical tolerancing based methods have the potential to be used together to predict the deviations of metal AM processes. These deviations should be represented in the form of the standardized quantifiers for tolerance specification and assemblability study. The role of standards and their implication on tolerancing for AM parts is explored by Ameta and others [Ameta et al., 2015]. The challenges related to tolerance transfer are also highlighted for producing single and multiple parts in a single build as per the geometric requirements. Some of them being the orientation selection, placement of parts on the build, and producing as-built assemblies. Specification issues in AM and the incorporation of new

capabilities of AM into the tolerance analysis also create issues and challenges. Some of the issues are in tolerance communication, tolerancing of the topology optimized shapes, and tolerancing of internal features [Ameta et al., 2018]. However, a standardized deviation estimation method leading to tolerance analysis and manufacturing assemblability for AM processes is yet to be developed.

Explicitly, in terms of the part geometry, AM standard ISO 17296-3 [ISO 17296-3, 2014] specifies the need to follow geometric quantifiers which should be measured and controlled to ensure the following geometric attributes of an AM part:

- Size, length, angle dimensions, and dimensional tolerances
- Geometrical tolerancing (deviations in shape and position)

These quantifiers are defined and controlled by geometric dimensioning and tolerancing (GD&T) characteristics outlined in ISO 1101 [ISO 1101, 2017] and explained briefly in section 1.3. Several articles in the academic literature outline methods for ensuring geometric tolerance for AM and DfAM guidelines for the same [Leach et al., 2019; Colosimo et al., 2018; Zhu et al., 2017; Ameta et al., 2015]. However, many of these articles focused primarily on size and overall deviation control leaving major research gaps. i.e. inclusion of the standardized GD&T characteristics for deviation quantification of AM parts and processes, both for GBTA based experimental studies and for process modeling studies.

To summarize, despite the presence of large number of benchmarks in literature which are used for AM part and process qualification, the benchmark artifact design process is not streamlined. The features on the benchmarks are not able to quantify geometric tolerances that can lead to reliable data. Non-compliance with the ISO 1101 based GD&T characteristics is also a major set-back in the geometric benchmarks present in literature. This leads to a research gap for formulating the benchmark design methodology and testing it for applicability for process parameter optimization leading to geometric quantification and prediction for an AM process. The discussion on Table 4 suggests that a normative benchmark design based on GD&T quantifiers is missing for AM processes in general. Further, for prediction of geometric tolerances, there are no clear guidelines present in literature to assess and predict GD&T and assemblability of the AM parts. This thesis work is focused on addressing limitations outlined in above sub-sections to ensure accurate geometric tolerance quantification and prediction of AM processes by using ISO 1101 based GD&T characteristics.

1.6. Objectives

Based on the literature review above, the main objective of this thesis is the development of a geometric tolerance quantification and prediction framework. The individual objectives are explained below. The linkage between various objectives of this thesis is presented using a schematic in Figure 9.

1. Development of a systematic methodology for the design of geometric benchmark test artifacts (GBTAs) for additive manufacturing (AM).
2. Testing of the GBTA design methodology on FFF process for parametric variation and simulation studies for GD&T quantification and estimation.
3. Development of a normative GBTA based on the methodology developed in objective 1, for LPBF processes.
4. Development of a predictive method to evaluate the geometric tolerances of the AM parts with respect to GD&T characteristics for investigating the assemblability of mating parts.

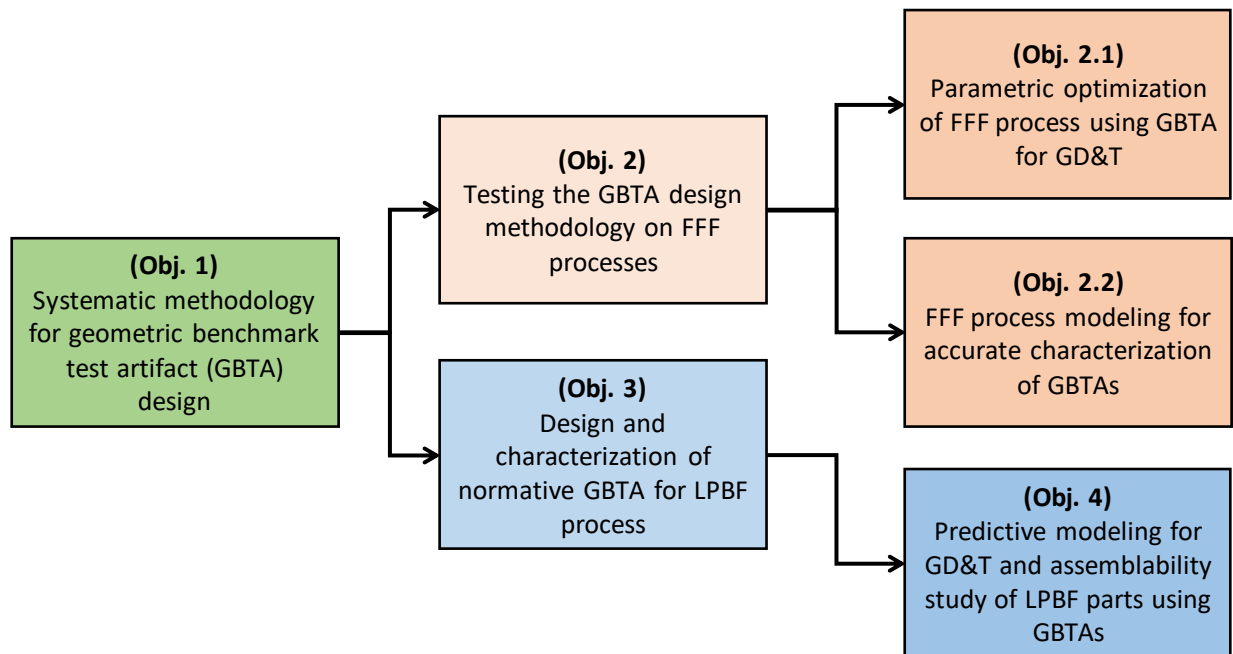


Figure 9. Schematic presenting the linkage between different objectives of the thesis

2. Systematic feature-based design methodology for GBTA design for AM²

The main purpose of manufacturing GBTAs is to predict and evaluate geometric capability and uncertainties in the AM process before manufacturing the final product or a ready to use part. A new methodology is presented for the systematic design of GBTAs depending on the AM process and required geometric properties. The GBTA design guidelines for specific process and application are based on feature technology and assembly consideration. The methodology will provide systematic guidelines for selecting previously available GBTAs, redesign based on the available ones or designing a new GBTA from scratch as per requirement. Finally, a case study is presented to demonstrate the use of the new methodology to design a new GBTA according to given geometric requirements.

2.1. Systematic methodology

A GBTA design methodology is proposed that can provide systematic guidelines for GBTA selection and design for AM process capability analysis and for geometric properties evaluation depending on specific requirements and process parameters on a particular AM process. Figure 10 and Figure 11 schematically shows how the process flows for a geometric benchmarking and GBTA design, which in turn is dependent on the purpose or the need for which a particular GBTA is designed. The benchmarking, divided into stage 1 and 2 will provide the user with required tools, and knowledge base which needs to be selected, based on the particular product's functional requirement or output property requirement. In the first stage, i.e. for AM process geometric characterization for a new process or a machine, a generic GBTA like NIST or a newly designed one can be taken to characterize the process and to optimize parameters using designed experiments. Further, ranking tables for the parameters and geometric tolerance value tables should be made. On the other hand, stage two is need-based, where geometric evaluation is required prior to manufacturing high-cost geometry, or as per some specific geometric property, assembly constraint, or kinematic requirement.

² Parts of this chapter have been published in:

- B.S. Rupal, R. Ahmed, A.J. Qureshi, "Feature-based methodology for design of geometric benchmark test artifacts for additive manufacturing processes", *Procedia CIRP*, Vol. 70, pp. 84-89, 2018.

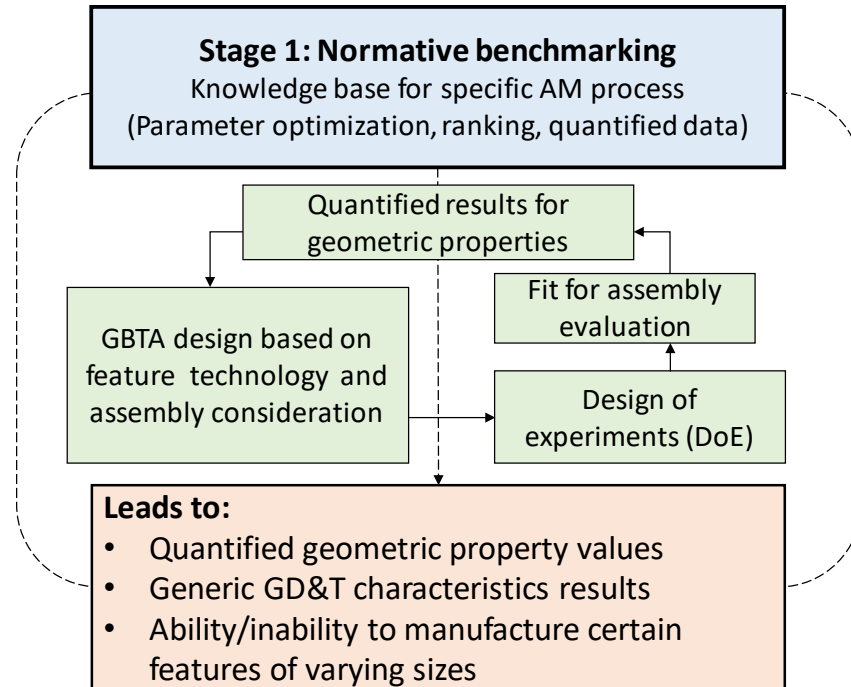


Figure 10. Stage one of geometric benchmarking and GBTA design

In the second stage, the geometric process capability results from the first stage can be used to select the process as it will provide a comparison of the geometric capability of the different processes for which data is available. Also, it will provide optimized parameters and their ranking for a particular geometric property. However, the requirement of the application (a specific product such as the GE aircraft bracket shown in Figure 12) will need a new GBTA design. The rationale behind designing a new GBTA for the second stage is that there can be cases in which certain geometric property needs to be evaluated at some different process and toolpath parameters, for which manufacturing again the generic GBTA is mere wastage of time and money. However, designed experiments will be required in category three as the parameters will change as per other predominant output properties. The first stage will eventually lead to the GBTA design criteria which are based on feature technology and assembly consideration guidelines provided in next section.

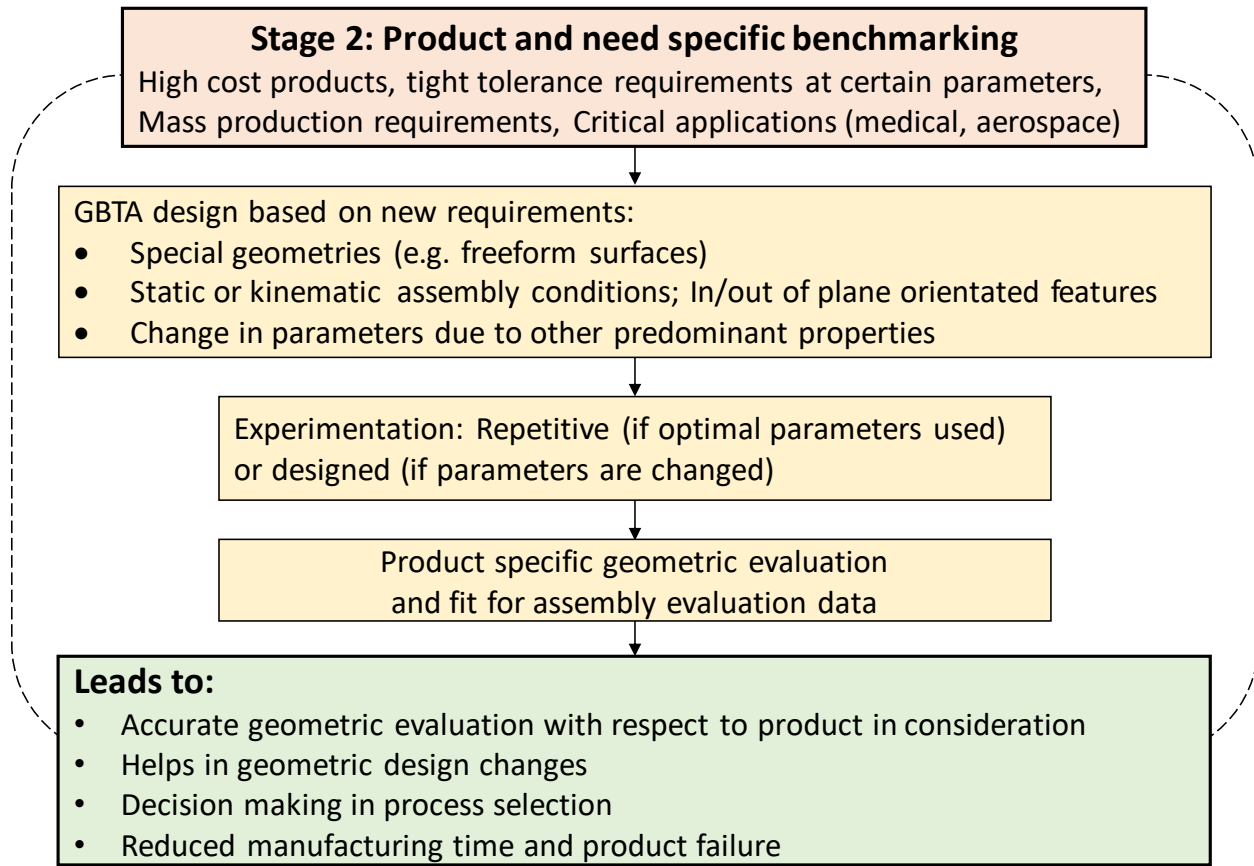


Figure 11. Stage two of geometric benchmarking and GBTA design

2.2. Feature technology and assembly consideration

According to one of the first papers on feature technology by Jami J. Shah, “Features encapsulate the engineering significance of portions of the geometry of a part or assembly, and, as such, are important in product design, product definition, and reasoning, for a variety of applications” [Shah J.J., 1991]. In general, feature technology simplifies complex geometries based on the generic implicit features, common edges, and surfaces. For example, a cylinder is a primitive feature for a piston. Feature technology is in use for process planning and manufacturability evaluation from the last two decades. In AM, it is used to develop AM design feature database [Bin Maidin, 2012] and feature extraction for remanufacturing using AM and machining [Paris and Mandil, 2018]. Moreover, to provide guidelines to obtain optimal part build orientation depending on feature definition and alternate orientations [Zhang et al., 2016]. Similarly, feature technology has the potential to play a role in GBTA design. The idea is to attach the available GD&T characteristics and geometric evaluation metrics to specific features. Mostly

generic implicit features such that the user has the freedom to select features as per the requirement (mostly functional) on a case-to-case basis as selected. Rather than manufacturing the available and overdesigned GBTAs which are unable to evaluate the required geometric/GD&T characteristics. On the other hand, the size of the base plate, size of features, the orientation of the features, the number and location of the features on the base plate are also a matter of case-to-case base selection. For example, in processes like FFF or LPBF the orientation of the part around the z-axis (in x-y plane parallel to the print bed) also has a key role to play as the raster direction changes with the change in orientation and so does the geometric properties in x and y direction. In such a case, two similar features in different orientations can be used on one GBTA or one feature can be used on a GBTA and the whole GBTA can be manufactured in various orientations. These decisions will stay with the designer and will vary as per material, cost and time availability.

Our focus is to assign features to the GD&T characteristics, which will provide a holistic geometric evaluation as the GD&T characteristics cover all the form, profile, orientation, location and run-out characteristics [Cogorono, 2006]. Along with the GD&T characteristics, the fit for assembly depends on static and kinematic considerations of the mating surfaces. Assemblability needs to be considered to make sure that the parts assemble and function properly after manufacturing.

The geometric properties and corresponding design features are depicted in Table 6 and Table 7. Guidelines for the feature selection with respect to the GD&T characteristics are presented in Table 6. Other important geometric properties, and assembly considerations along with features for basic mechanical joints are presented in Table 7. These features are classified as per the degree of freedom for evaluating the fit for assembly for any specific AM process. However, complex or compound assembly joints, such as in human body, can be included as required. The fit for assembly evaluation will include classifying the joints based on the fits that they can achieve according to the IT tolerance grading e.g. clearance, transition or interference fits. In the feature selection presented in Table 6 most of the features are primitives and basic mechanical features that form the kinematic structure of any mechanical assembly or mechanism. For freeform features, characteristics like the profile of a surface are included. The rationale behind selecting a bicubic surface is that when performing a virtual analysis, it becomes easy to make a CAD model of a mathematically defined surface, rather than a complete free-form surface. However, other surfaces like Bezier or NURBS surfaces can also be used. The uniqueness of this methodology is

that it is completely modular and gives the designer freedom to select the features based on the geometric properties' requirement, kinematic constraints, specific AM process, and parameters that the user is concerned with. Including variable size features also includes the effect of scalability [Qureshi et al., 2015], which further aids in the geometric prediction of scaled up/down parts. In the next section, a case study is presented to validate the above methodology.

Table 6. AM features for GD&T characteristics evaluation

GD&T characteristic	AM Features proposed
Straightness	Features with flat surfaces, Cuboids
Flatness	Features with flat surfaces, Cuboids
Circularity	Cylindrical protrusions and depressions
Cylindricity	Cylindrical protrusions and depressions
Profile of a line	Bicubic polynomial surfaces and a datum
Profile of a surface	Bicubic polynomial surfaces and a datum (base plate can be used)
Perpendicularity	Flat surface with corresponding normal datum feature
Angularity	Prismatic primitive features like prism with variation in angles (both acute and obtuse angles)
Parallelism	Features with flat protrusions with surfaces parallel to a corresponding datum feature/plane
Symmetry	Symmetric protrusions with flat surfaces with a datum mid-plane
True Position	Holes and protrusions (pins) located at varying distances from common datums
Concentricity	Cylindrical protrusions and depressions with a datum
Circular run-out	Cylindrical protrusions and depressions with a datum
Total run-out	Cylindrical protrusions and depressions with a datum

Table 7. AM features for other geometric properties and assemblability evaluation. DOF – degree of freedom.

Geometric property	AM Features proposed
Dimensional accuracy	Same primitives and features used above with different orientations and positioning for accuracy data in x, y & z direction
Minimum feature size	Fine features and primitives (Cubes, cylinders) with decreasing sizes
Repeatability	Per print: Similar features on one GBTA Per batch: Printing GBTA repeatedly with different process and toolpath settings
Surface Finish	Surface features (flat, cylindrical and bicubic)
<i>Assembly considerations (Fit for assembly evaluation)</i>	
Revolute Joint (1 DOF)	Detachable links with holes and a pin of mating dimensions (hinge type joint)
Prismatic Joint (1 DOF)	Detachable solid and hollow cuboid of mating dimensions
Threaded Joints (1 DOF)	Relevant threaded screw pair of variable dimensions
Cylindrical Joint (2 DOF)	Detachable pin and hole of mating dimensions
Spherical Joint (3 DOF)	Ball and socket of relevant dimensions
Planer Joint (1/2/3 DOF)	Flat and/or cylindrical pin in corresponding slots of 1/2/3 DOF of mating dimensions
Snap Joints [Klahn et al., 2016]	Snap and an undercut of basic designs (annular, tapered)

2.3. Case study and conclusions

For the case study, General Electric (GE) LEAP® aircraft engine bracket is considered as application product as shown in Figure 12, for which we want to achieve desired geometric output as per the functional requirement. As described by Carter and others [Carter et al., 2014], the major functional requirement for the bracket is the mechanical strength to bear static and torsional load on the horizontal holes. The geometric requirements for functionality of the bracket will be governed by assembly conditions of vertical holes i.e. static assembly joint (pin and hole) and the horizontal holes i.e. kinematic assembly joint.

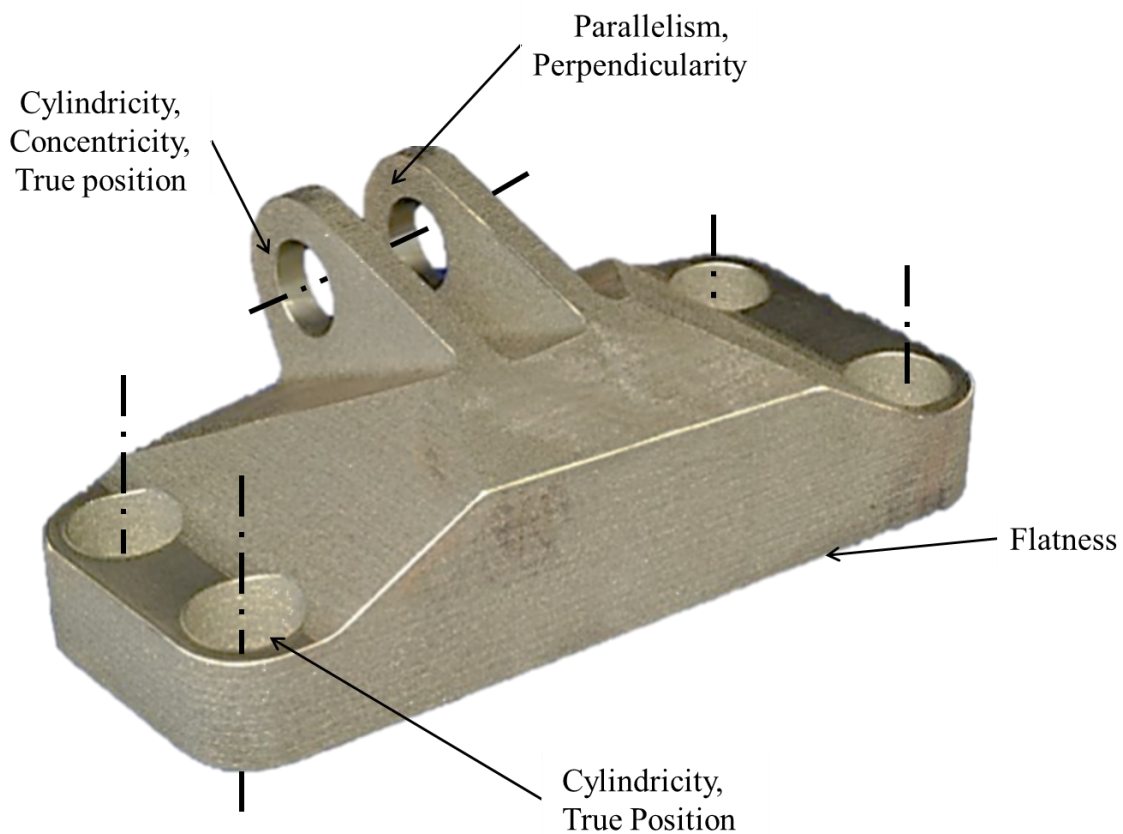


Figure 12. GE LEAP® aircraft engine bracket (Adapted from Carter and others [Carter et al., 2014])

Here, the joint for both vertical and horizontal holes are cylindrical joints (2 DOF). To control the form of the holes cylindricity tolerance is required and concentricity (or a correlative tolerance) is required for the parallel holes with the horizontal axis. Flatness tolerance is required to control

the form of the base, which influences the location of both static and kinematic assembly joints. Parallelism tolerance between the protrusions for the two horizontal holes is required for locating and maintaining functionality of the holes. Perpendicularity or an angularity tolerance may be required to maintain the axial relation between the out of plane holes. A position tolerance is required to locate the four vertical holes. The features on the proposed GBTA design for this specific application product are described in Table 8. Clearly, in this specific application, the geometric properties other than described in functional criteria section in Table 8 are not required. Hence, there is no need to include their corresponding features in the GBTA design. A base plate can be used to mount the features and to act as a datum for relative geometric characteristics and the fit for assembly features must be detachable to perform the limits and fit for assembly evaluation. For reliable results using GBTAs, it is always recommended that GBTA should also go through exactly same post-processing (finishing) operation if there is any for the application product in consideration.

Table 8. Features on the GBTA and corresponding geometric characteristics

Geometric characteristics	Features
Cylindricity and Concentricity	Cylindrical holes of varying diameters with axis perpendicular and parallel to the base plate with axis as datums for concentricity measurement
Flatness	Flat surface parallel to the base plate
Parallelism, Perpendicularity	Flat surface parallel to the side plane of the part and a corresponding datum feature/plane
True Position	Holes and protrusions (pins) located at varying distances from common datums (at least two datums on both orthogonal planes: base plane and side plane)
Fit for assembly (Static and kinematic)	Cylindrical pins of varying diameters (corresponding to the dimensions of the holes) with axis perpendicular and parallel to the base. The holes with an axis parallel to the base will need kinematic fit for assembly testing for motion.

A major assumption that is observed in almost allGBTAs found in the literature is to reach results without manufacturing theGBTAs in various orientations or to not include features on theGBTAs in various orientations. This case study is a good example of such case in which the results for the vertical cylindrical features can be taken (wrongly assumed) for the horizontal holes. However, if we include cylindrical features in horizontal and as well as vertical orientations in aGBTAs the results will not be similar. This is a common problem for products which have similar features in different orientations on the same geometry. In such cases, even if we orient the base of the part according to the optimized parameters, some features will still be aligned in orientations which are not optimal. This notion is well explained and validated by Zhang and others [Zhang et al., 2016] by studying different feature orientations on same geometry and their optimization. This assumption along with other disadvantages of genericGBTAs discussed in the literature section of the Introduction chapter led to the development of a systematic methodology forGBTAs design for normative geometric characterization, for product specific applications, and parametric optimization. This case study also proves to be an excellent example of stage two of theGBTAs selection (Figure 11) in which the process and toolpath parameters are decided according to another predominant output property. In this case study, the process and toolpath parameters governing the mechanical property requirements will also be used to manufacture this specific bracket, which will nullify all the results obtained on the parameters optimized for geometric properties using any genericGBTAs. This proves the need for aGBTAs selection and a systematic design methodology based on feature selection. Hence, it is a paramount step for designed experimentations based onGBTAs to evaluate geometric properties of the AM parts and assemblies. Now, based on the newly proposedGBTAs design methodology, the next section will focus on its implementation on the FFF process's geometric tolerance characterization and assemblability.

3. Parametric optimization for GD&T and size tolerances for FFF process³

3.1. Background and context

The most prominent challenge in FFF process is to achieve the desired geometric properties of the manufactured components [Gibson et al., 2014]. To manufacture high-quality components, which adhere to the required mechanical and geometric properties specified in the CAD model, as well as pass the strength and ‘fit and function’ tests for the assembly components, an experimental investigation of the process is required. Ensuring desired mechanical and geometric properties will not only save the lead-time and re-design time but also save the client time and production cost [Mostafa et al., 2018]. Research for attaining required geometric characteristics is based on applying experimental and analytical methods on the AM process for prediction and analysis of dimensional accuracy and geometric tolerances. Some challenges of investigating the role of geometric tolerances in AM were first mentioned by Ameta and Witherell [Ameta et al., 2015; Witherell et al., 2016]. However, a significant number of researches focused on modeling and minimizing the shape deviations, and geometric tolerances analysis were conducted in the last five years. A methodology of predicting the component accuracy in FFF with a focus on STL settings was published by Moroni et al. to estimate deviation values by calculating volumetric error [Moroni et al., 2014]. This method sets a path for analysis of STL settings but does not include other process parameters and thermo-mechanical aspect into account during the mathematical modeling. In another study [Lieneke et al., 2016], deviations for the FFF process were studied with respect to influencing factors including the component location in x, y, and z directions, and the results were demonstrated in the form of tolerance classes (IT classes). Huang and others [Huang et al., 2014; Huang et al., 2015; Wang et al., 2016] investigated a dedicated statistical approach for shape deviation modeling and prediction. These papers provide an in-depth understanding of the shape deviation from the geometric complexity point of view, using mathematical models based on basic shapes like cylinders and polygons. However, it needs to be taken a step further by

³ Parts of this chapter have been published in:

- B.S. Rupal, K. Ramadass, A.J. Qureshi, “Investigating the effect of motor micro-stepping on the geometric tolerances of Fused Filament Fabrication printed parts”, *Procedia CIRP*, Vol. 92, pp. 9-14, 2020.

conducting parametric optimization to achieve fit and function, such as the inclusion of bead geometry in FFF process.

Another approach found in the literature is based on experimental techniques [Pfeifer et al., 2016; Sood et al., 2009; Equabal et al., 2017] and designed experiments to make models based on the printer-specific results. Shahrain and others [Shahrain et al., 2016] discussed the effect of 13 parameters on various GD&T characteristics in FFF printing and found out that for extruder temperature, infill density and print orientation have the maximum effect on a metrics made with a summation of different GD&T characteristics. Certain other STL based methods like improving the STL conversion algorithms [Paul et al., 2015], error compensation by correcting slice files [Tong et al., 2008] are also found in the literature, which can form a good starting point for total error calculation and compensation. Optimization techniques for accuracy and achieving geometric properties such as I-optimality criterion [Mohamed et al., 2016], variation classification using machine learning [Samie Tootoni et al., 2017], spectral graph theory is also found, which help to optimize the process parameters. Experimental studies using factorial designs [Mohamed et al., 2015] have also explored the dimensional accuracy of certain features and linear dimensional study. Only a few research works have focused on ‘fit and function’ testing in regard to FFF. In one such study [Dantan et al., 2017], a mathematical model based on various defect modes in FFF is made for calculating the prediction values. Point to point deviation was estimated and compensated for minimal deviations.

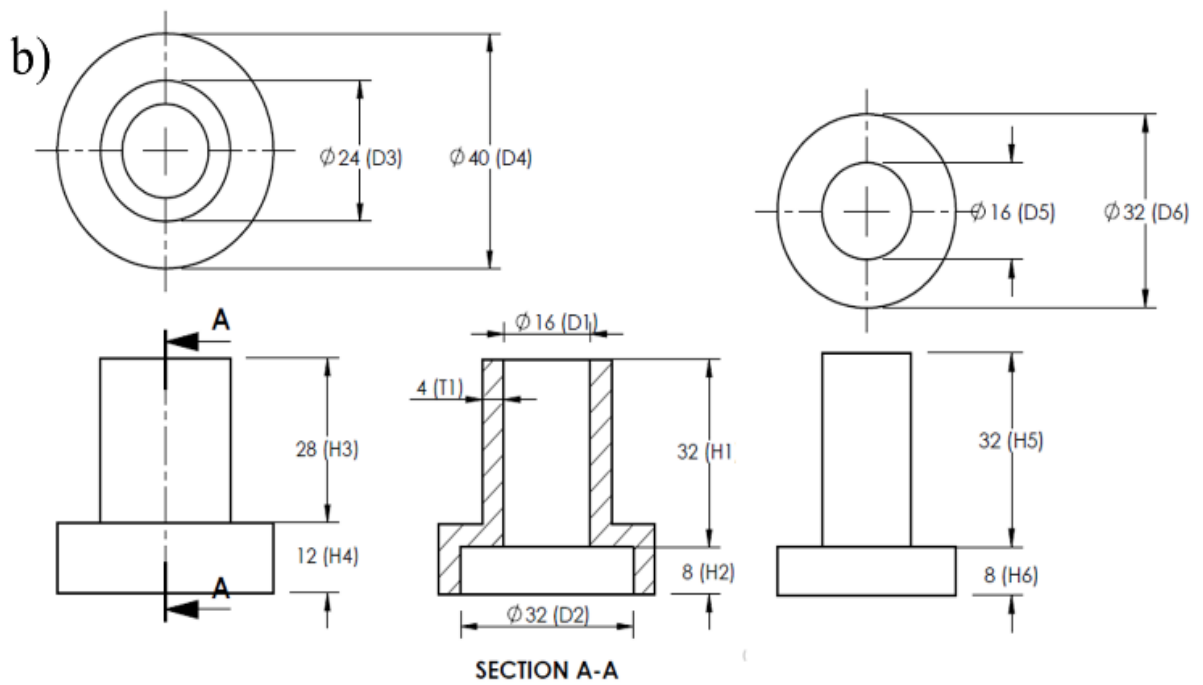
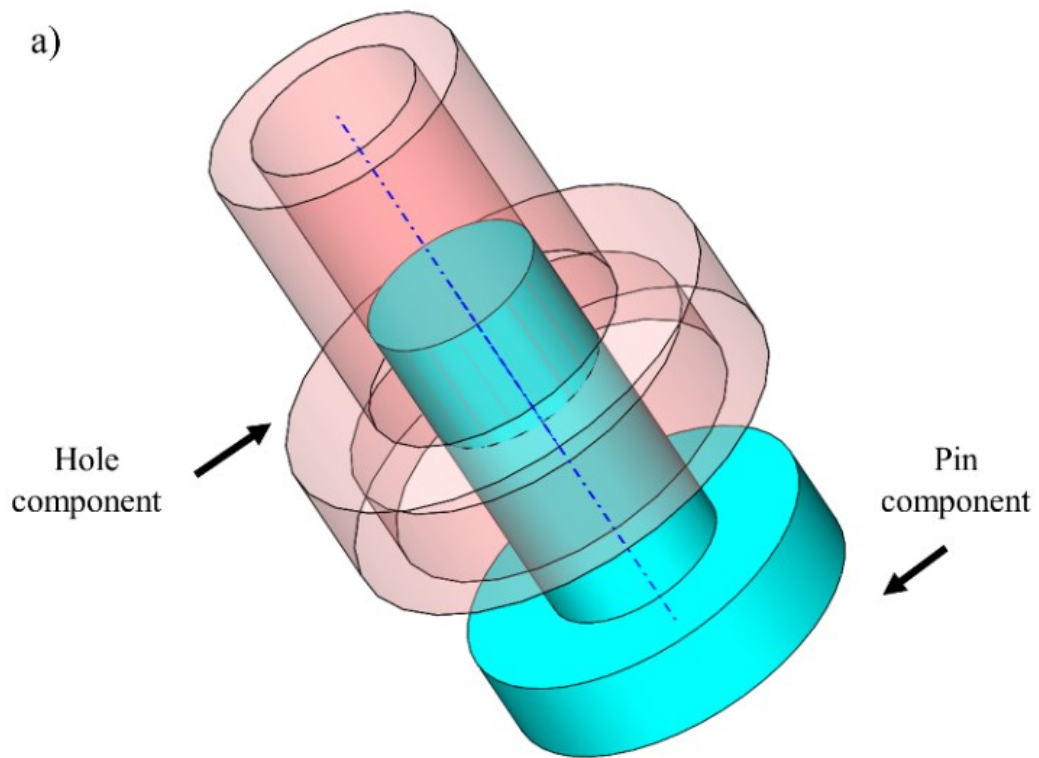
As discussed above, most of the experimental and modeling methods are considering the AM process to be ideal and assume the machine components and operation to be perfect, since no process variable is considered in the above studies. Moreover, the experiments and benchmark artifacts selected for many research works do not give a holistic idea about the geometric characteristics of the AM process considered. For example, a benchmark without cylindrical features cannot give any information about cylindricity tolerance. On the other hand, the analytical and simulation methods do not consider the process variations and uncertainties into account, which leads to non-accurate and non-reliable results. The current chapter will investigate parameters for predicting the accuracy of the printed components conforming to the input CAD model and under required geometric tolerances. Ideally, this accuracy prediction should be reliable enough to give information about the fit and function of the printed assembly components. This objective provides insight into the dependence of the deviations on the various process parameters

and the possibility of errors in the firmware. To do so, an experimental study on FFF printed parts for characterizing geometric tolerances based on Geometric Dimensioning and Tolerancing (GD&T) standards is conducted with an end-goal of ensuring assemblability of printed parts. The factors included in the experimental design include parameters which are not studied before such as material type, the effect of micro-stepping of the gantry motor, but that need consideration for ensuring the geometric tolerances

3.2. Experimental methodology

To characterize the geometric tolerances of the printed components, the first step is to design a geometric benchmark test artifact (GBTA). Various conditions need to be met for benchmark design in order to ensure reliable geometric tolerance characterization. The benchmark selected for this study is shown in Figure 13. The design of the benchmark is based on the feature-based geometric benchmark test artifact design methodology formulated in chapter 2. Cylindrical features are most affected by the triangulation and micro-stepping of the motor. Therefore, a cylindrical pin and hole component is selected to understand this effect. Since the features for the assembly are different from each other in terms of size and form (hollow/solid), pre-defined tolerances fits were not used. A specific tolerance band from the features is not expected, and the size tolerance results are presented in the form of IT grades. Further, the pin and hole components are subjected to an assemblability and 'fit for function' testing.

For selecting the input parameters, literature studies and the experimental results on the FFF printer were considered. Component size is considered as one of the parameters as a previous study [Shahrain et al., 2016] found that it has a significant effect on the dimensional deviation and GD&T characteristics, after fixing the other parameters to optimal values. Moreover, some of the major process variables or printing parameters are already studied in the literature, e.g. bed temperature, infill settings, and print orientation. [Mahmood et al., 2018; Qureshi et al., 2015]. Those parameters are considered constant in this study and have been assigned optimal values for minimum geometric variation. STL setting is also considered as it affects the cylindrical features, and it's necessary to study its interaction with other input parameters. A Taguchi's L9 orthogonal array [Roy et al., 2001] was selected as it is a robust experimental design method. *Lulzbot TAZ- 5* FFF printer was used for printing. The relationship between the input and output variables is depicted in Figure 14.



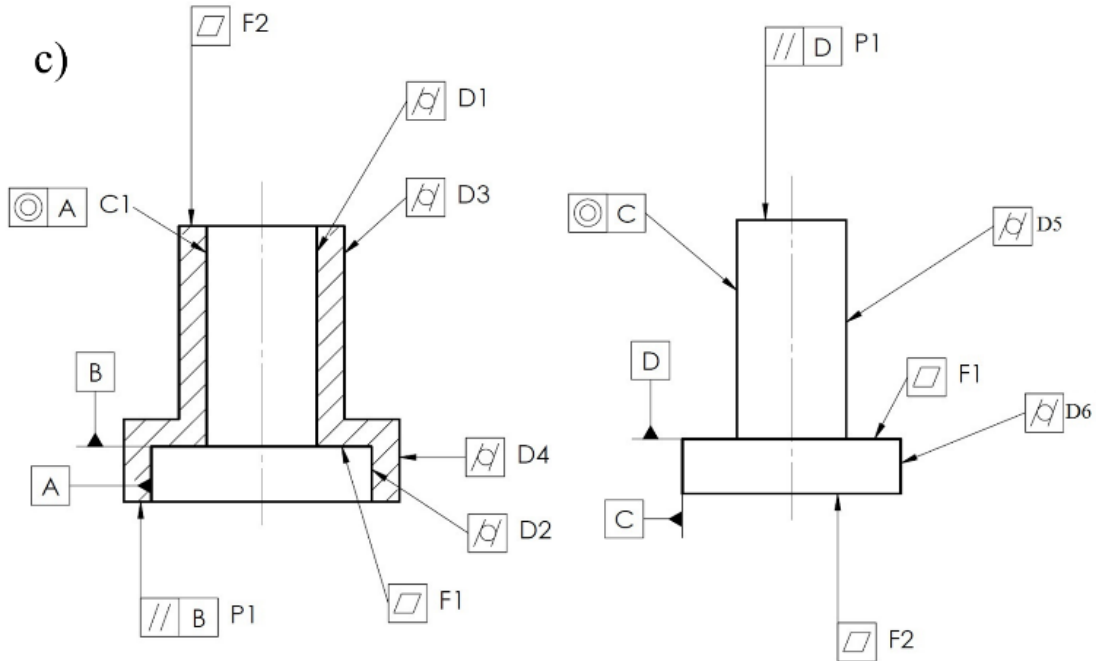


Figure 13. a) The hole and pin benchmark artifact depicted in mating condition for the assembly
 b) The hole and pin benchmark artifact linear dimensions c) Corresponding GD&T characteristics for functionality

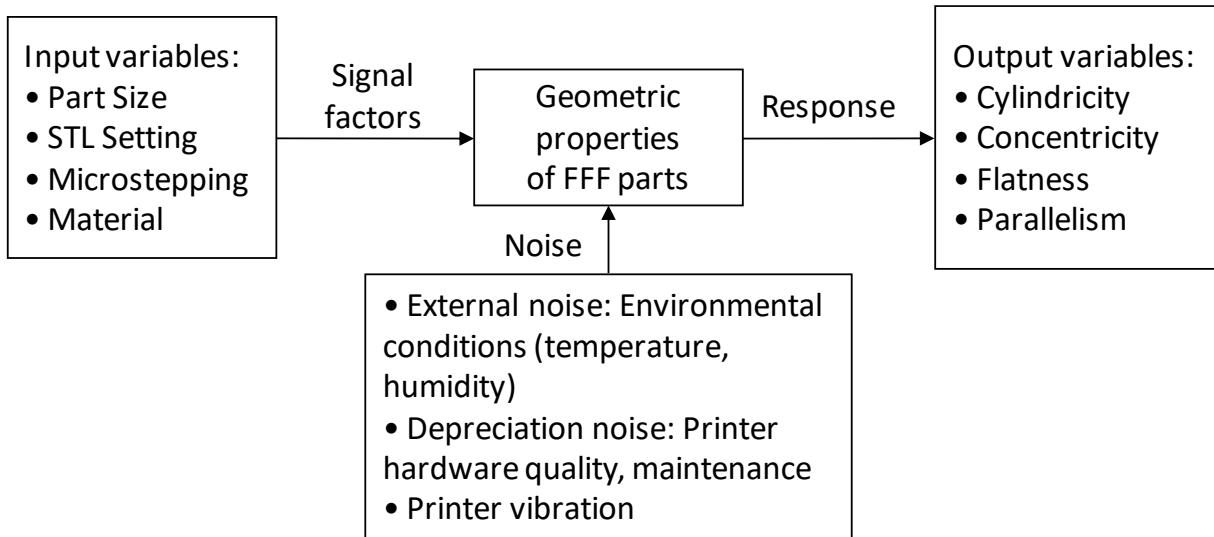


Figure 14. Relationship between the input and output variables

The input parameters for geometric analysis are explained below:

1. *Component Size*: Component size is an important parameter for FFF printers. It will enable the quantification of error related to machine assembly and misalignments, as these are cumulative and affect the accuracy as a function of build volume.
2. *STL Setting*: The triangulation of the CAD file affects the accuracy of the component geometry, especially in curved features such as cylinders. Hence, it affects the dimensional accuracy and GD&T features like cylindricity and concentricity.
3. *Micro-stepping*: The movement of the extruder is solely dependent on the motors, and on the slides. There is further dependent on the micro-stepping of the motor. Micro-stepping defines the minimum motor increment, therefore determining the resolution of the movement and hence accuracy. A NEMA 17 stepper motor is used for the motion control of the extruder. A total of four motors control the motion of the extruder on the print bed. Two motors operate in parallel to move the extruder in Z direction, one in X direction, and one in Y direction. The micro-stepping is altered by changing the motor programming, but the physical setup, kinematic relations of the printer and the motor were not disturbed. The effect of this change in micro-stepping is then studied in terms of geometric tolerances along with other process parameters.
4. *Material*: Different materials have different mechanical, thermal and surface properties, and these properties change with varying temperatures as well. That, in turn, determines the dimensional accuracy of the component manufactured with that material.

The L9 array experimentation was conducted three times for achieving repeatability. So, a total of 54 components were printed: 27 pin benchmark components and 27-hole benchmark components. The printed components, one each from each material, are shown in Figure 15. The output parameters include GD&T characteristics. Four main GD&T characteristics are selected according to the geometry of the assembly. These are cylindricity, flatness, parallelism, and concentricity. The analysis was performed in *Minitab* software; the ranking was obtained for means and signal-to-noise ratio for all the output variables.



Figure 15. Printed components: ABS, PLA, and Magnetic PLA

The data was analyzed for means and signal-to-noise ratio. ‘Smaller is better’ signal-to-noise ratio was selected, as all these characteristics need to be minimized to achieve a dimensionally stable, interchangeable and accurate components which will be later tested for ‘fit and function.’ A Mitutoyo Coordinate Measuring Machine (CMM) was used to measure the GD&T tolerances. The resolution of the CMM is 0.0005 mm. The factors and levels for all input variables are depicted in Table 9.

Table 9. Factors and levels table

Factor	Level 1	Level 2	Level 3
Component	Small	Nominal	Larger
Size	80%	100%	120%
STL Setting	Coarse	Fine	Optimal
Micro-stepping	1/4	1/16	1/4
Material used	ABS	PLA	Magnetic Iron PLA (MAG)

Micro-stepping was kept at two levels (1/4 and 1/16) due to the manufacturer’s hardware limitation in the *Lulzbot TAZ-5* FFF printer. The micro-stepping is altered by changing the motor programming, but the physical setup of the printer was not disturbed. It is to note that surface roughness has not been included in this study as the average surface roughness values are comparatively far lower than the geometric tolerances for the FFF process, parameters, and materials considered in this study [Vahabli et al., 2016; Haque et al, 2019].

3.3. Results and discussion

To start with the data analysis, simple descriptive statistics were performed in ‘Statistica academic’ on the collected data. As the experiments include variation in input settings, the statistical analysis will help to find the geometric variability of the printer. The results for dimensional deviation in the diameters are shown in Figure 16. The maximum dimensional deviation from nominal is observed in the smallest diameter of the hole component, i.e. 0.36 mm for D1. However, for the hole component (D1, D2, D3 and, D4), the deviation from nominal gradually decreases as the diameter increases.

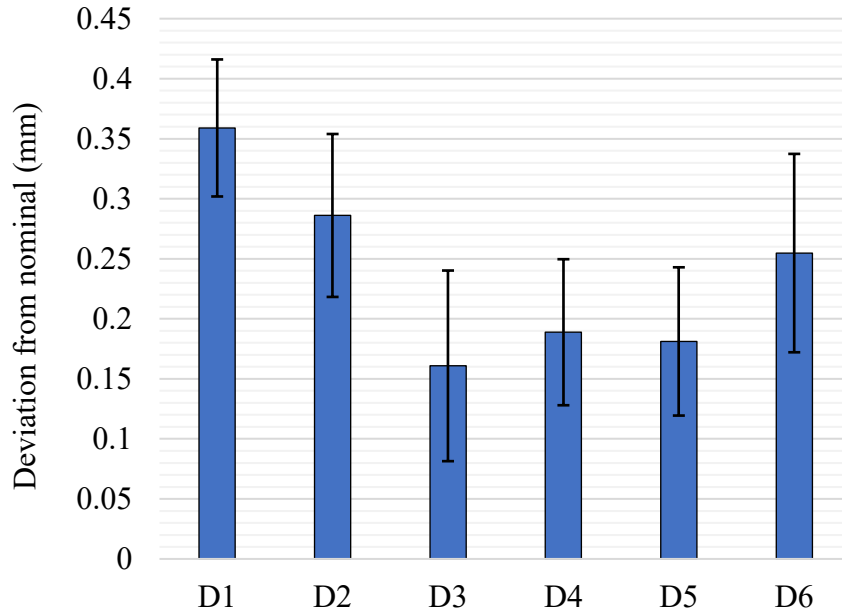


Figure 16. Dimensional deviation from nominal diameter (mm)

For the pin component (D5 and D6), larger deviation from the nominal is observed in the larger diameter feature. The error bars show the standard deviations between the three sets of samples taken for each feature measurement. The value of the standard tolerance grades or IT (International tolerance) grades for nominal sizes is taken from the table 1 of the ISO 286-1 standard [ISO 286-1, 2010] and allocated to the dimensional deviation results obtained in this study. The deviations from the size dimensions represented in terms of the industry standard IT grades are shown in Table 10. It gives a fair idea about the clearance and assemblability of the mating parts provided the geometric tolerances are considered along with the deviations from the nominal dimension.

Table 10. Tolerance zones for mating features along with IT grades

Diameter	Nominal dimension (mm)	Tolerance with IT grades (mm)		
		Minimum deviation	Average deviation	Maximum deviation
D1 (Hole)	16	0.1729 (IT12)	0.3590 (IT14)	0.6008 (IT15)
D5 (Pin)	16	0.0137 (IT7)	0.1812 (IT13)	0.5927 (IT15)
D2 (Hole)	32	0.0114 (IT6)	0.2860 (IT13)	0.4233 (IT14)
D6 (Pin)	32	0.0103 (IT5)	0.2547 (IT13)	0.7239 (IT15)

For cylindricity, the results are shown in Figure 17. For the hole component, cylindricity tolerance decreases from D4 to D1 as the diameter decreases, similarly for the pin diameters. The results for the average flatness for the ‘F1 hole’ (hole component) have a six sigma (six standard deviations) spread of about 100 μm with a mean at 50 μm . However, for the ‘F1 pin’ (pin component), the six-sigma range is approximately within 200-250 μm . The average value for flatness is reduced due to tighter values for hole component values and are around 100 μm with mean value at 70 μm as shown in Figure 18. Similarly, parallelism has a six-sigma spread of 100 μm for the pin component. For average values, the spread is 110 μm with mean value at 60 μm .

The concentricity results show a large spread for both inside and outside features with an average range of 450 μm and mean at 300 μm .

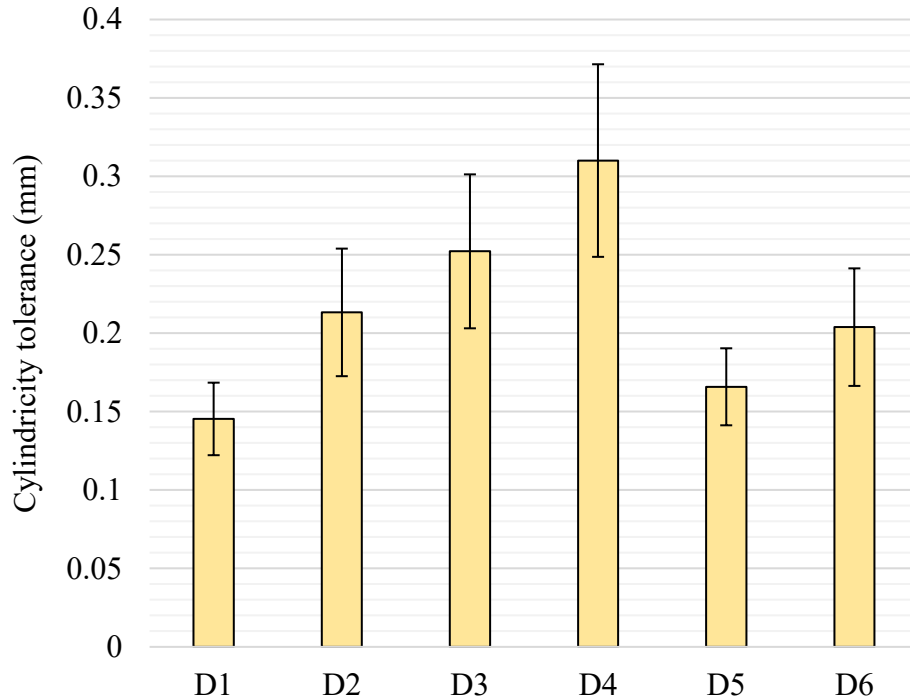


Figure 17. Cylindricity tolerance results (mm) for FFF study

Since concentricity is a composite tolerance, so a higher tolerance band is usually expected. From all the output variables considered, only cylindricity is dependent on component size; the rest of all the variables, i.e. flatness, parallelism, and concentricity are independent of component size. These size-independent GD&T characteristics are summed to form a common output variable called ‘FPC average,’ and the results are shown in Figure 19.

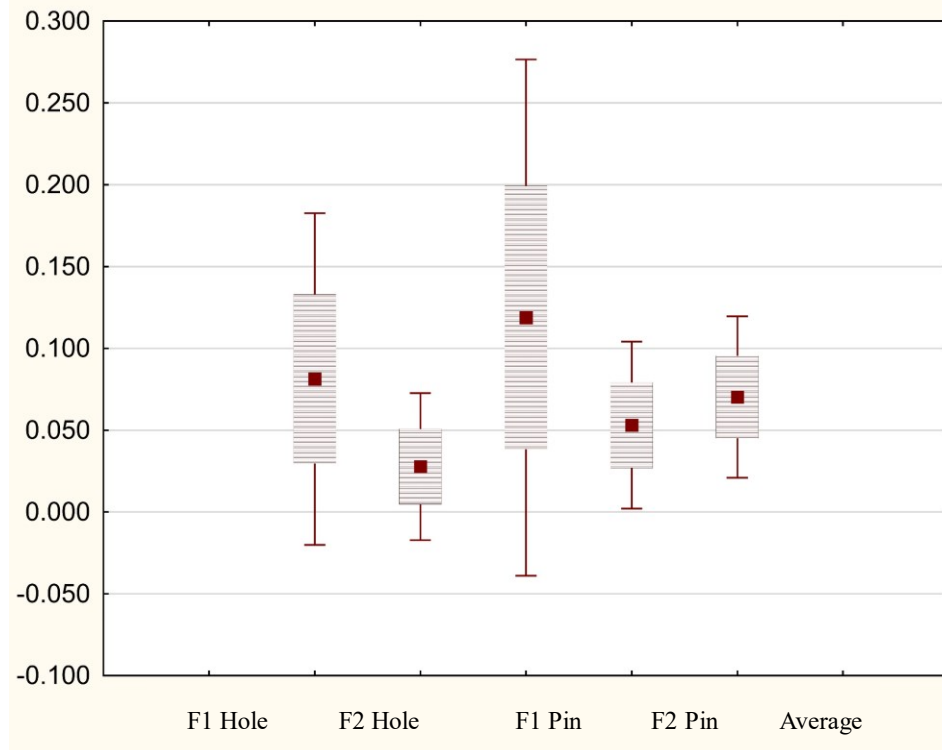


Figure 18. Flatness tolerance results (mm) for FFF study

The six-sigma span of the FPC average is about 140 μm and the mean value at 140 μm . Only the concentricity tolerance needs to be controlled to bring the mean closer to zero and to tighten the six-sigma spread. The metric FPC average will help to reduce the overall GD&T variation by setting the optimal variables for this metric. To understand the above-discussed results and their dependence on the input variables, Taguchi's optimization is performed in Minitab software and is discussed below.

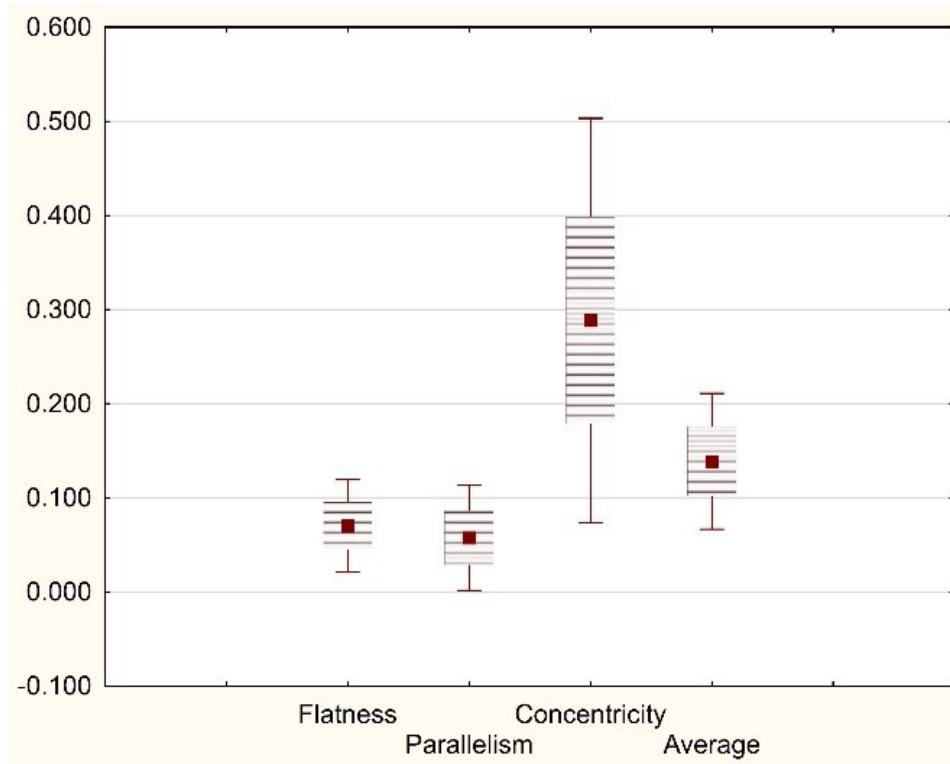


Figure 19. Box and whisker plot for Flatness, Parallelism, Concentricity and FPC average

The results for all the output variables were computed with *smaller the better* signal-to-noise ratio as the aim was to minimize the deviations as well as the GD&T tolerances. As seen in Figure 20, material and size have a maximum effect on the percentage cylindricity. This is in-line with the finding of descriptive statistics regarding the effect of material properties on the outer and inner features of the component.

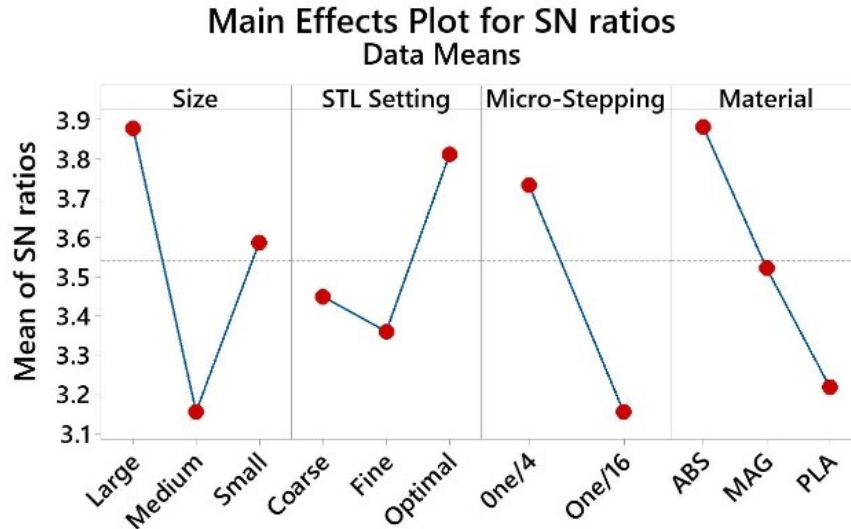


Figure 20. Main effects plot for signal-to-noise ratio for percentage cylindricity tolerance

However, micro-stepping and STL settings also show a large slope in the plots; hence they are important as well and can be used to fine-tune the results for higher accuracy with optimal material and size settings. For the FPC average, as shown in Figure 21, the material is the most significant input parameter, which establishes an explanation for the large difference of 100-150 μm in the six-sigma span of the inside and outside Flatness values.

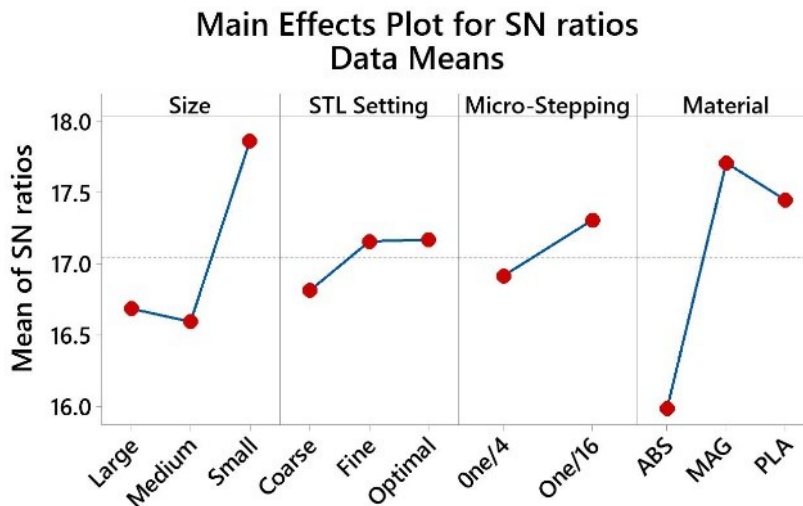


Figure 21. Main effects plot for signal-to-noise ratio for FPC average

Table 11. Signal-to-noise ratio ranking table

Geometric feature	Size	STL setting	Micro-stepping	Material
Cylindricity	1	4	3	2
Flatness	2	3	4	1
Parallelism	3	2	4	1
Concentricity	1	4	3	2
FPC average	2	4	3	1

As shown in Table 11, concentricity stands out from the rest of the GD&T characteristics with size as the most significant factor and material at number two. The reason behind this change of significant factors is that as the size of the cylindrical increases, the effect of the motor resolution and micro-stepping on the geometry of the component decreases and hence concentricity tolerance decreases. The same reason explains the dependency of cylindricity on the size of the component. The metric ‘FPC average’ is also evaluated in the optimization process.

Table 12 shows the optimal settings for different input variables. The optimal settings for minimum deviations and cylindricity are exactly the same; hence for confirmation tests, these settings will be used for a common evaluation of both the variables. Similarly, the settings for flatness and parallelism are quite similar except the micro-stepping setting, which proves the hypothesis that firmware analysis and systematic error from firmware (micro-stepping in this case) affect the geometric output. Also, it is interesting to note that individual results for flatness, parallelism, and concentricity have the optimal at large size setting, but FPC average optimal values are at the small size.

Table 12. Optimal settings table

Variables	Size	STL Setting	Micro-stepping	Material
Cylindricity	Large	Optimal	One/4	ABS
Flatness	Large	Optimal	One/16	MAG PLA
Parallelism	Large	Optimal	One/4	MAG PLA
Concentricity	Large	Optimal	One/16	PLA
FPC Average	Small	Optimal	One/16	MAG PLA

3.4. Conclusions

Printing accurate components with shape and form control in FFF is a complex problem and depends on various process parameters. This chapter presents the effect of the process parameters and material on the geometric tolerances of the printed parts while considering motor micro-stepping as a parameter, which has not been considered before. A Taguchi's experiment was designed and conducted which clearly shows that micro-stepping significantly affects geometric and size tolerances. Also, the size of the component and material selection are the important factors for geometric characteristics, and the characteristics improve with an increase in size.

The benchmark approach discussed in the chapter can be applied to any AM process to check its geometric characteristics, manufacturing assemblability and repeatability. Furthermore, finding the optimal parameters for overall GD&T tolerance minimization and developing methods for CAD compensation with respect to the GD&T quantifier requirements is still an open research area. The research in geometric tolerance quantification and prediction can increase the use of AM in precision manufacturing such as micro-fabrication and precision AM parts.

4. Accurate geometric prediction for FFF process⁴

As discussed in the previous chapter, the primary issue with the experimental testing of the geometric properties is that it is time-consuming, inhibits the 3D printer from printing the actual products, and requires extensive material resources. Furthermore, additional equipment, such as co-ordinate measuring machines (CMM) and laser scanners for testing the geometric behavior, is needed. Analytical and modeling methods on the other hand are more sustainable and do not lead to material wastage and downtime.

However, current modeling methodologies fail to provide an accurate deviation map of the geometric characteristics of the FFF printed parts. This is due to the fact that most models ignore the slicing parameters and no methodology has attempted to incorporate these parameters into the virtual analysis. Since the properties of the printed part are dependent on the slicing parameters as well, it is of great importance to include that parameters in any virtual analysis to predict the output properties. Process parameters related to the slicing of the STL file such as the number of contours, air gaps, hatch spacing, and infill density will be considered for the prediction purposes. For example, it has been proven experimentally that variation in infill has a drastic effect on the mechanical properties [Mostafa et al., 2018] and geometric properties [Shahrain et al., 2016] of the printed part.

The need for a reference to compare the FFF manufacturing errors to, led to the development of ‘Reverse CAD algorithm’. This algorithm provides a ‘theoretical ideal replica of the printed part’ which includes the intrinsic FFF manufacturing errors/stamp such as the layers waviness from the sides, filament pattern curvature from the top and bottom, and part orientation. During the FFF process other uncontrolled manufacturing errors happens due to material viscosity, nozzle and bed temperature effects, warpage, nozzle speed, positioning accuracy, and other uncontrolled errors. By comparing the final manufactured part shape to the original input CAD file is not completely correct as the FFF Stamp/intrinsic errors will always be there. The reverse CAD algorithm can be used to optimize the slicing parameters to minimize the intrinsic errors/stamp, and by comparing the manufactured part to the reversed CAD model the uncontrolled process errors can be optimized.

⁴ Parts of this chapter have been published in:

- B.S. Rupal, K.G. Mostafa, Y. Wang, A.J. Qureshi, “A reverse CAD approach for virtual estimation of geometric and mechanical properties of FDM printed parts”, *Procedia Manufacturing*, Vol. 34, pp. 535-544, 2019.

This research work focuses on quantifying the issues related to the sliced file and its effect on the manufactured part characteristics using virtual methods without experimentation. This will be realized by developing an algorithm which is capable of converting the sliced file (toolpath) back into a solid CAD model called the Reverse CAD model. The methodology for the work is shown in Figure 22. The generic AM process chain is modified. A geometric and mechanical analysis is performed on the Reverse CAD model to check the model for design requirements. If the conditions are met, then the sliced file is sent to print. Otherwise, design changes or parametric variations are made to meet the design criteria. The Reverse CAD algorithm is explained in detail in Section two. The geometric and mechanical characteristics assessment results are discussed in Section three and four respectively. Since this chapter conducts an initial validation of the algorithm, the geometric characteristics comparisons are performed based on deviation maps. Finally, the conclusions and future scope are described in Section five.

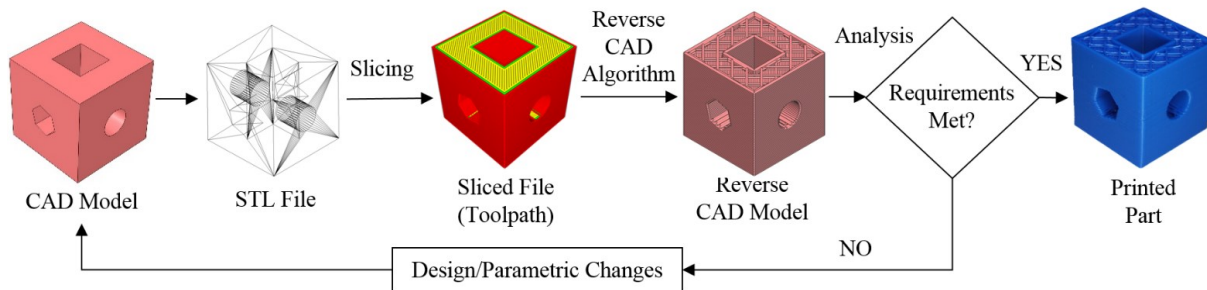


Figure 22. A flowchart depicting the output property prediction methodology based on the Reverse CAD algorithm

4.1. Reverse CAD methodology

The FFF process starts by slicing the CAD file in order to be additively manufactured with respect to the required process parameters using a pre-processing slicer software. The output of the slicing software is a G-code for the extruder nozzle path. The reverse CAD algorithm, which is demonstrated in Figure 24, is written in the MATLAB environment. It reads the output G-code and the constants values; for example, the layer thickness and the road width are fed into it. It then calculates the deposited filament cross section parameters using equations (4.1) to (4.7). The deposited filament is assumed to ellipse, as shown in Figure 23Figure 24, based on previous studies

which used microscopy imaging to analyze the filament profile and used the ellipse to analytically model mechanical and geometrical behavior [Ahn et al., 2002; Bellehumeur et al., 2004; ISO 527-1].

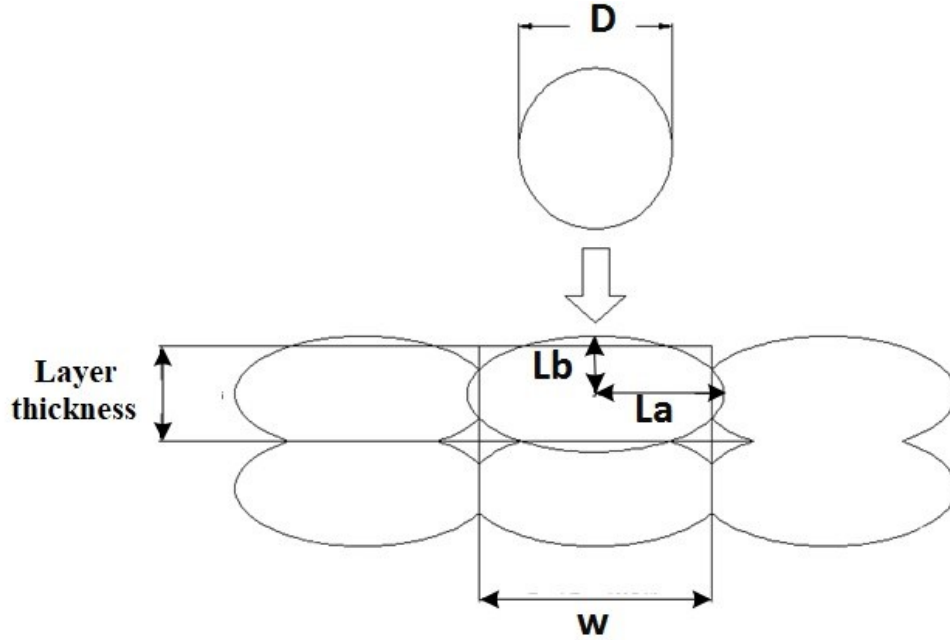


Figure 23. Theoretical model for the filament as an ellipse

The equations (4.1) and (4.2) define the major and minor radius of the deposited filament's shape, i.e. ellipse. The deposited filament has l_a as the major radius and l_b as the minor radius of the ellipse, while w is the road width and r are the overlap ratio between adjacent filaments. lth is the layer thickness. Further, equations (4.3) and (4.4.) calculate the surface areas of the filament before and after deposition. Where S_1 is the surface area of the filament before deposition, where D is the extruder nozzle diameter, and f is the shrinkage value after deposition and cooling off. S_2 is the surface area of the elliptical cross-section of the deposited filament. By equating S_1 and S_2 and using equation (4.1) and (4.2), the ellipse radii and the overlap ratio are computed. The overlap ratio is defined in equation (4.5), and the computed major and minor radius are presented in equation (4.6) and (4.7) respectively.

$$l_a = \frac{w \times r}{2} \quad (4.1)$$

$$l_b = \frac{lth \times r}{2} \quad (4.2)$$

$$S_1 = \frac{D^2 \times \pi}{4} \times f \quad (4.3)$$

$$S_2 = l_b \times l_a \times \pi \quad (4.4)$$

$$r = \sqrt{\frac{D^2 \times f}{w \times lth}} \quad (4.5)$$

$$l_a = \sqrt{\frac{D^2 \times f \times w}{4 \times lth}} \quad (4.6)$$

$$l_b = \sqrt{\frac{D^2 \times f \times lth}{4 \times w}} \quad (4.7)$$

The algorithm scans the code line by line and searches for the different G-codes that correspond to different printing actions. There are two main modes in the FFF process: in the first mode, the extruder moves without printing in a fast approach motion, while in the second mode, it extrudes material with a certain linear speed. If the Reverse CAD model is required without the support materials, the code will discard any path for the support or the interface material. If the second printing mode is detected and the path is either a contour, a raster infill, or a shell, an Application Programming Interface (API) sequence syntax writing function is called in order to export the syntax used by the CAD software to generate a corresponding 3D model for the extruded path. The API collects the starting and end points of the current printing path and writes a syntax to create a plane at the start point and perpendicular to the required path. Then another syntax is created to sketch an ellipse on the previous plane using the previously calculated parameters. After that, a syntax is written for the extrusion boss/base of the created ellipse with an extrusion length correspondent to the difference between the start and end point of the printed line trajectory. The extruded ellipse geometries are combined as one part only at their intersection areas as shown in Figure 24, while the resultant voids between the non-intersecting ellipses are kept in the reverse CAD model.

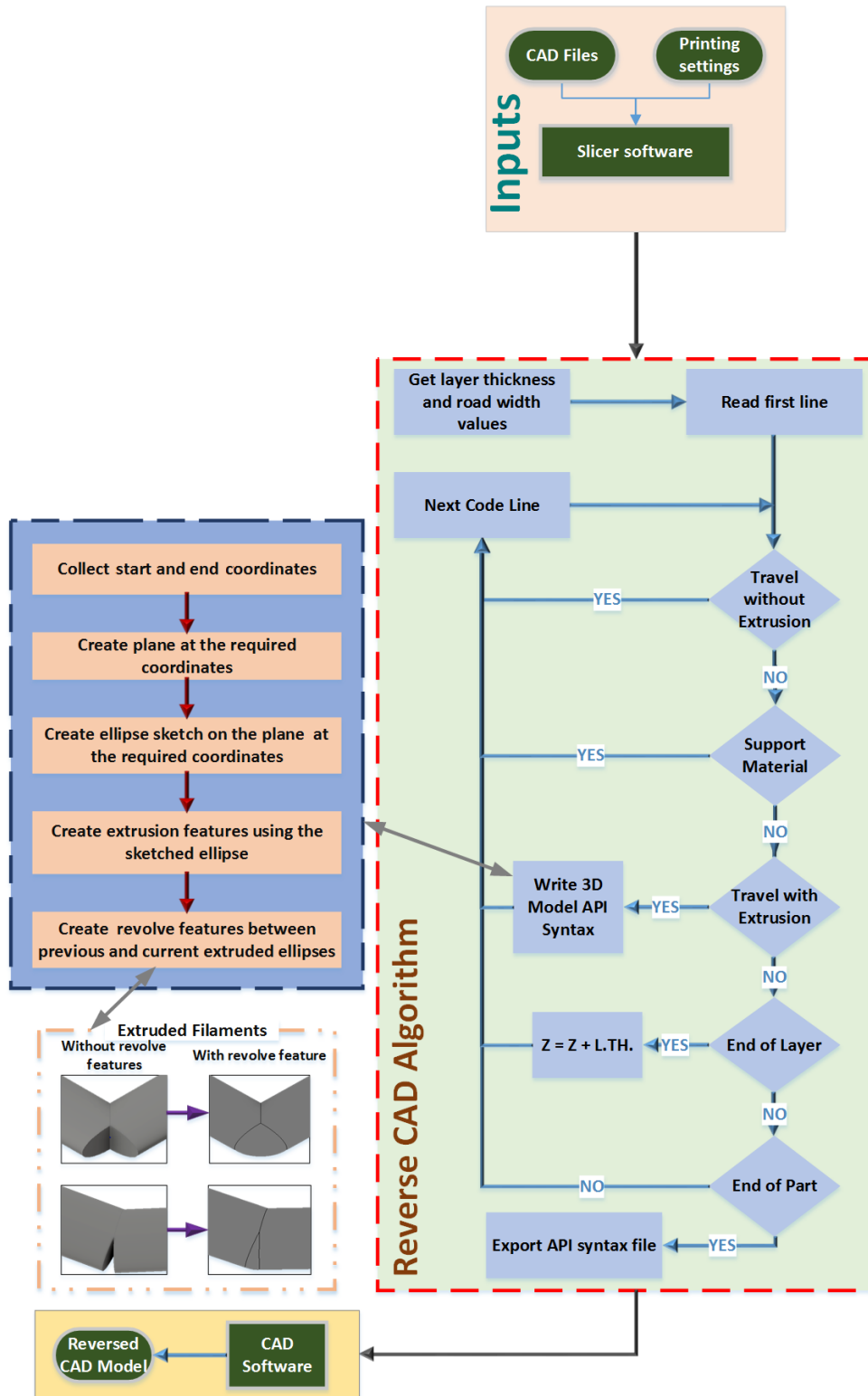


Figure 24. The Reverse CAD algorithm

The last syntax is written to create a revolve feature between the currently printed line and the previous line, fill in the sharp gap developed, and to simulate the filament bending between two tool paths intersecting at an angle. After a layer ends in the G-code, the algorithm shifts the z coordinates in the vertical direction by the layer thickness value. The algorithm exports a file containing sequenced API syntaxes after it determines that the printing of the part is finished in the G-code. In the CAD software, the API launcher is used to open the syntax file and the part is 3D modeled as instructed in the initial G-code. Finally, a CAD file is exported and can be opened with any CAD software and used to analyze the properties of the part.

The time to convert the exported G-code into an API syntax file is negligible compared to the time to convert the API syntax into a reversed CAD model. The time consumed to create a reversed CAD model consisting of 700 features, like extrusions and revolves, with their sketches is around one hour. It was noticed and then experimented that as the number of features per part increase the time consumed to create the next feature within the same part takes longer time, for example the creation time of the of the feature with the sequence number of 100 is one second while the feature with the sequence number 400 is three seconds and the 700th features takes eight seconds. The whole operation was done on a computer of 16 GB memory and Core I7 Processor with 4GHz capacity.

4.2. Results and discussion

CAD models of primitive geometries with small features were selected to demonstrate the working of the algorithm. Reverse CAD models were generated for the designed models using the algorithm. A cube was modeled, saved as an STL file, and a slicing file was created. A sparse infill pattern was selected for the cubical part as well as a 45⁰ raster angle. Similarly, a cylindrical part was modeled and saved as a slicing file. The critical process parameters for both parts are depicted in Table 13.

The slicing files for both the parts were fed into the Reverse CAD algorithm, and the Reverse CAD models were generated. The infills density of the outer shell used is set lower than 100% in order to depict the capability of the algorithm in a better way. Finally, the parts were printed using a Stratasys F370 FFF printer and compared to the Reverse CAD model. The Reverse CAD model, and the corresponding printed parts are shown in Figure 25. The layers, infill spaces, shells, and contours depicted in the Reverse CAD models are the same as in the printed parts. Now

that we have established that the algorithm can generate an accurate virtual model of the part to be printed, we are moving forward with the analysis.

Table 13. Printing Parameters for experimentation

Parameters	Cube	Cylinder
Infill pattern	Sparse	Double sparse
Number of contours	5	4
Raster angle	45 ⁰	0 ⁰
Layer thickness (mm)	0.33	0.33
Number of shells	1	1
Infill density	50%	100%

First, the mass properties of the Reverse CAD models and the final printed parts were compared to obtain confidence in the applicability of the Reverse CAD models for virtual analysis. To check the effect of the slicing parameters on the mass properties of the printed parts, a mass comparison study was conducted. It involved assigning the same material (ABS plastic in this case) to the Reverse CAD model and calculating the mass properties of the model virtually. A comparison between the mass of the initial CAD model (A), Reverse CAD model (B) and the printed part (C) average was conducted, and the results are shown in Table 14. A percentage difference between the mass properties was calculated. The cube's infill pattern was sparse and the cylinder's infill pattern was double sparse. Still, the Reverse CAD predicted the mass properties accurately, regardless of the infill settings. For example, it is clear from the 77% difference that the initial CAD model cannot provide a satisfactory estimation of the mass properties of the printed part, which has a 50% infill density. The difference reduces to only 14.1% when compared with the Reverse CAD model. It is worth mentioning that the mass variability between the same printed parts are within +/- 0.2 grams This type of study can prove critical when the mass of the part is one of the important design criteria. The difference between the properties of the material assigned in the software and the actual material is the reason for the 10-15% difference between the Reverse CAD model and the actual part mass properties.

Table 14. Mass comparison Table

Mass comparison (grams)	Cube	Cylinder
Original CAD Model (A)	11.97	9.17
Reverse CAD model (B)	7.711	8.618
Printed Part (C) (Average)	6.758	7.738
Percentage difference ($ C-A *100/C$)	77.12	18.50
Percentage difference ($ C-B *100/C$)	14.10	11.37

A geometric deviation analysis was performed on the Reverse CAD files, and comparisons were conducted with the initial CAD file to check for possible geometric deviations before printing the part. This not only helped to identify the regions with more geometric deviations, but it also allowed the designer to reorient the part and consider the slicing parameters to reduce the geocentric deviations. The geometric deviation analysis was performed by using SolidWorks academic version. First, the CAD model was opened in SolidWorks. Then the Reverse CAD file was imported into the same workspace using ‘Geomagics for SolidWorks’. After that, both models were aligned perfectly with each other and the ‘deviation analysis’ tool was used to calculate the results. Two cases of different part orientations were considered on the cylindrical part to conduct the analysis. In the first build orientation, the major axis of the cylinder was oriented at 45° with respect to the base build plane (refer Figure 26 a) For the second build orientation, the axis of the cylinder was rotated 90° with respect to the build plane (refer Figure 26 b). The corresponding geometric deviations for both the orientations are also shown. Geometric deviations from the range of -0.200 mm to +0.200 mm can be seen in both cases on different locations depending on the orientation. In case 1, the major deviation region is the smaller cylindrical hole perpendicular to the major axis, since the staircase effect is more prominent in that region. In case 2, the staircase effect is seen on top of the part and the lower side of the cylindrical holes. Further detailed and controlled geometric deviation analysis with parametric variations can prove useful for minimizing geometric deviations and parametric optimization for improving the geometric properties.

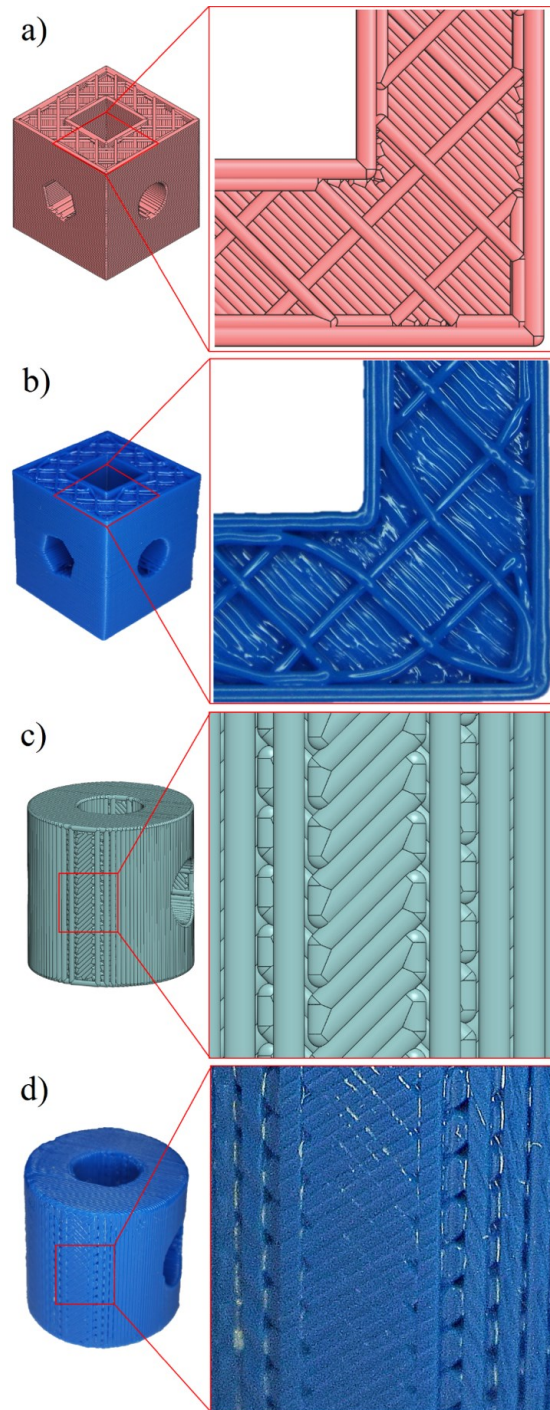


Figure 25. a) Cubic Reverse CAD model: isometric and zoomed-in view, b) The printed cubic part: isometric and zoomed-in view, c) Cylindrical Reverse CAD model: isometric and zoomed-in view, d) The printed cylindrical part: isometric and zoomed-in view

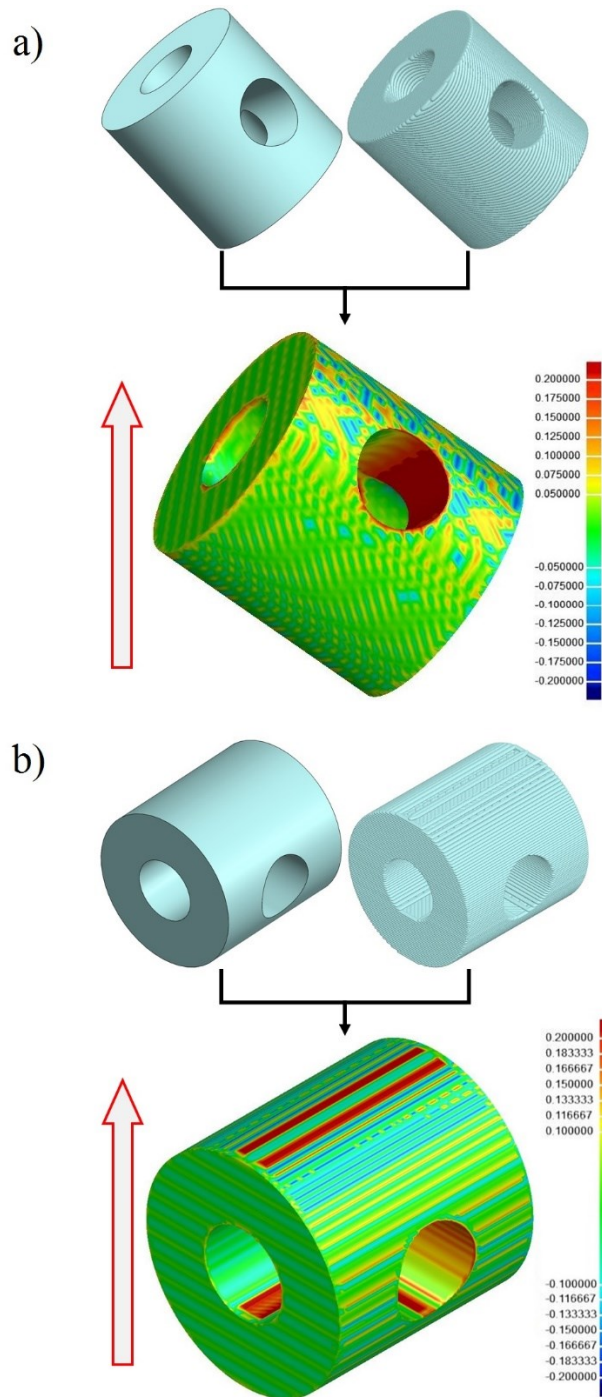


Figure 26. Geometric deviation analysis for the CAD model vs. Reversed CAD model of the cylindrical part, a) Build orientation 1: cylinder axis aligned to print bed, b) Build orientation 2: cylinder axis parallel to print bed

4.3. Conclusions

This chapter proposes an innovative tool for simulating the geometric and mechanical properties while using the current generation of open source/commercially available CAD/CAM software. This is based on a Reverse CAD algorithm, which reconstructs a CAD model from the sliced file. The Reverse CAD model is the virtual replica of the part to be printed with specific printer and machine parameters, for example, layer thickness, and infill density. The algorithm facilitates accurate modeling and analysis of the FFF printed part behavior. The application and efficiency of the algorithm are validated by geometric comparison, mass comparison, and geometric deviation analysis using different process parameters and printers. The limitation of the algorithm as of now is the computation speed, as the number of features increase in the CAD model, the computational speed decreases. However, the computational speed increases simultaneously to layer thickness, since it takes fewer loops to cover the same volume.

5. Normative GBTA design and characterization for LPBF process⁵

Based on the methodology developed in chapter 2, the geometric benchmark test artifact (GBTA) was designed to fulfill two major objectives:

- To perform the tri-planar GD&T quantification of the metal AM process,
- To study the effect of the base plate removal on the GD&T characteristics.

To achieve the first objective all major GD&T characteristics were quantified with a range of features and sizes, and the three principal planar directions were considered for the GD&T quantification for the normative quantification of the process. The features on the GBTA are selected as per the feature based GBTA design methodology developed in chapter 2, which gives systematic guidelines for selecting features as per the geometric tolerance characterization requirement. The ability to manufacture minimum feature sizes and overhangs was also considered. To fulfill the second objective, i.e., to characterize the effect of the removal of the base plate, GD&T quantifiers were measured before and after removal of the base plate.

Features on the GBTA were decided based on the GD&T requirements for the normative quantification of the geometric tolerance characteristics of the metal AM process. The bounding box size of the GBTA was decided based on the build volume of the LPBF system on which it had to be manufactured. Since the build volume was 250 x 250 x 300 mm, the size of the GBTA base was kept at 200 x 200 mm and then features were spread on that surface. In the case of LPBF, the raster direction changes with the change in orientation of the part in the AM machine. Therefore, the orientation of part has a significant effect on the geometric properties of the features. There are two different ways that this variation can be studied and characterized: 1) Manufacturing the features in different orientations on the same GBTA; or, 2) manufacturing the complete GBTA in different orientations. The former method is used in this study because for the latter method, the support structure design for the features in different orientations can vary significantly and, as a

⁵ Parts of this chapter have been published in:

- B.S. Rupal, M. Secanell, A.J. Qureshi, “Geometric Benchmark Test Artifact for Laser Powder Bed Fusion Process: Design and Preliminary Results”, 2nd Conference of NSERC Network for Holistic Innovation in Additive Manufacturing (HI-AM), June 2019, pp. 1-7, Vancouver, BC, Canada.
- B.S. Rupal, T. Singh., T. Wolfe, M. Secanell, A.J. Qureshi, “Effect of base plate removal on tri-planar geometric tolerances of SS 316L benchmark manufactured on laser powder bed fusion process”, *Materials Journal*, Vol. 14, issue 13, pp. 1-30, 2021.

result, it would not allow for a robust measurement and comparison of the benchmark artifacts samples. Therefore, the GBTA being used for this study is built by manufacturing features in different orientations on a common base. The features to be present on the GBTA base are shown in Figure 27 and are explained below:

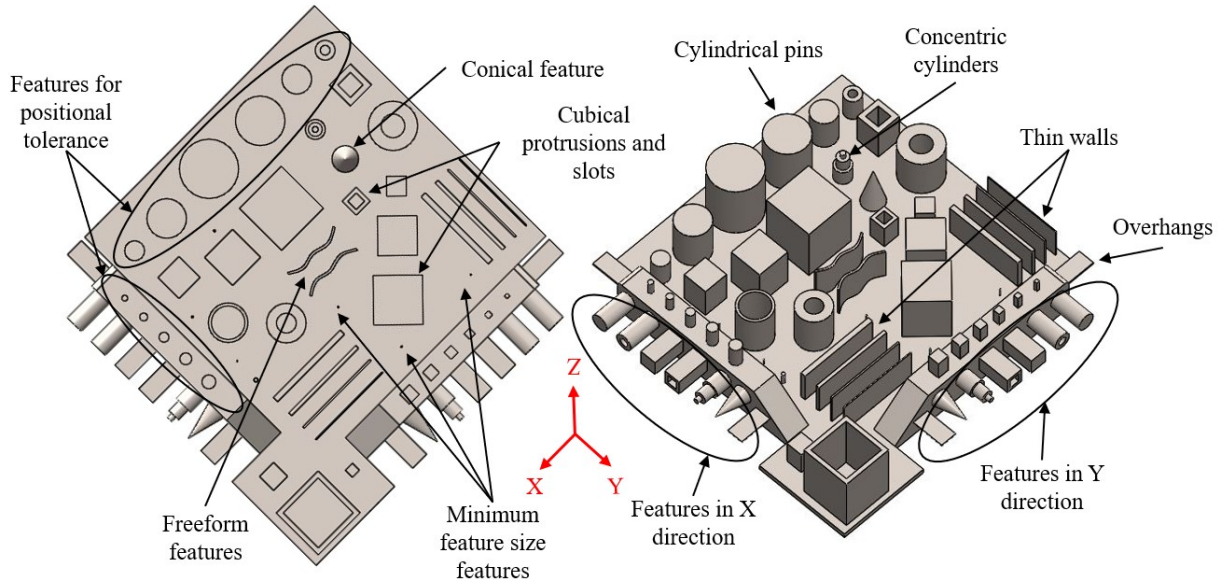


Figure 27. Nominal GBTA design and corresponding features. Left: Top view; Right: Isometric view.

1. Cuboids: Hollow and solid cuboids selected to quantify straightness, flatness, perpendicularity, parallelism. Since these are large volume features the effect of the process on the deviations will be different as compared to the small volume features such as thin walls.
2. Thin walls: Thin walls of varying dimensions to quantify straightness, flatness and the effect of residual stresses on the GD&T quantifiers for thin features.
3. Cylindrical features: Solid and hollow cylindrical features placed with axes in all three principal directions (X, Y and Z) to quantify circularity, and cylindricity.
4. Axially stacked cylinders: Stacked cylinders for measuring concentricity, and runout in X, Y and Z directions.
5. Conical features: For measuring circularity of features other than cylindrical form.
6. Positional features: Features positioned at a specified distance from each other to find positional tolerance zones of features with respect to each other.

7. Profile: Profile features with curves to quantify profile of a surface and profile of a line tolerance.
8. Minimum size features: Minimum size features with diameters and external sizes ranging from 0.5 to 2 mm. It will help to check the ability of the metal AM process in consideration to manufacture minimum sized features.
9. Thin overhangs: Thin overhang features to understand the effect of support and base removal on thin and fragile features.

In addition to the GD&T specifications and the other geometric quantifiers, it was required that the design consider the metal AM process constraints. The GBTA features were placed such that the maximum area on the base plate was covered to understand the spatial variation. The effect of variation in feature size on the geometric tolerances is also an important aspect to consider as the size tolerances has a significant influence on the design for metal AM in precision applications. Further the features are shown and explained in a greater detail in figures A1 and table A1 in Appendix A, which show the numbering of the features on the GBTA, and the relevant geometric tolerances of the features

5.1. Experimental procedure

Three newly designedGBTAs were manufactured with the *Renishaw AM250* LPBF process. The STL file of the GBTA is converted to a sliced file by specifying the process parameters, such as layer height, hatch style, and support structure, using the manufacturer provided software (Renishaw QuantAM). The process parameters are decided as per previous experience and manufactured using best practices. The process parameters for the manufactured parts were not varied and kept constant to investigate the variation in the process. The process parameters for the manufactured parts were kept constant to investigate the variation in the process and are listed in Table 15. The build chamber was sealed and then argon gas is introduced to maintain an inert environment for the laser-based manufacturing. The constant argon gas flow acts to keep the laser lens clean, reduce any oxygen or nitrogen entrapment, and moderate the vapor flow of the processed metal powder. Stainless steel SS 316L grade powder from *Renishaw*TM is used as a raw material for the manufacturing. The powder reaches the build platform through a channel and lands on one side of the build plate, which is bolted on top of the build platform. A silicon recoater

spreads the metal powder evenly on the build plate and a 200 W laser then melts the powder as specified by the input STL file. The build platform moves down one-layer height equal to the layer thickness and the powder is spread using the recoater for the next layer. Upon completion of the build, the part is left in the chamber to cool down to room temperature for one hour and then removed. One of the manufactured samples, as manufactured and attached to the build plate is shown in Figure 28. To understand the as-built geometric properties of the GBTA, the manufactured samples were assessed without any kind of post-processing.

Table 15. Machine Parameters and Manufacturing Parameters for the Experimentation

Machine Settings	Value	Manufacturing parameters	Value
Layer thickness	0.050 mm	Powder material	Stainless Steel (SS 316L)
Laser power	200 W	Powder particle size	0.015 – 0.045 mm
Base plate size	250 x 250 x 15 mm	Hatching style	Chessboard style
Scan speed	600 mm/s	Hatch spacing	0.150 mm
Laser beam diameter	0.07 mm	Interlayer angle	67 degrees

5.2. Measurement procedure

The features on the manufactured samples were measured for various GD&T characteristics using a Mitutoyo Crysta-Plus M443 Co-ordinate measuring machine (CMM). The CMM has a resolution of 0.0005mm. For the measurements with the base plate, the GBTA was stationed on the CMM table with fixtures to restrict its movement. The measurement was conducted keeping in mind the tight tolerance zones of the LPBF process under consideration, so reducing measurement variability was the priority. For each characteristic measurement, at least ten data points were taken on the CMM and each measurement is repeated thrice to achieve repeatable readings.

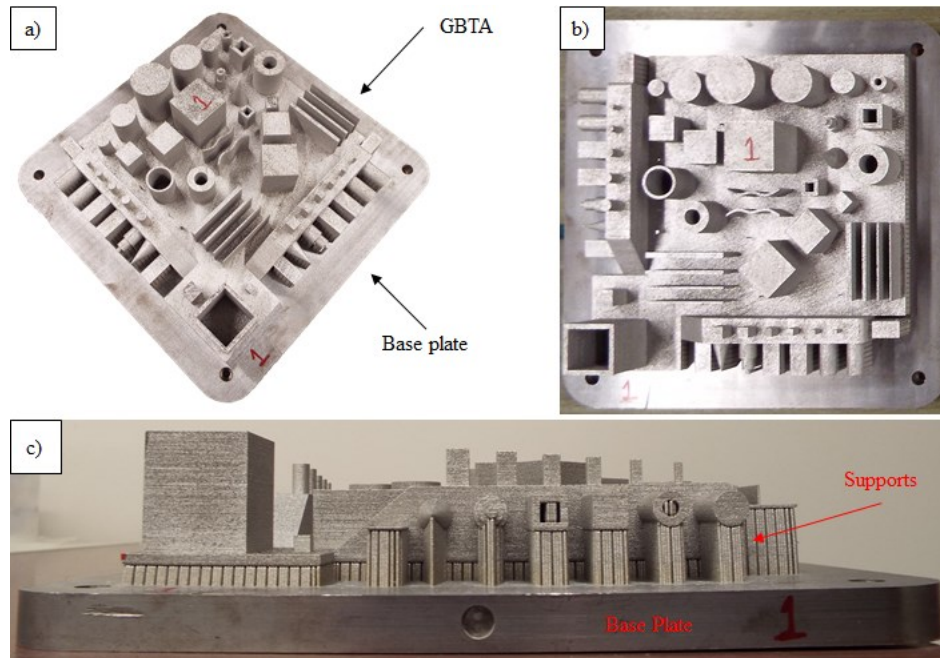


Figure 28. a) Isometric view of the GBTA, b) Top view of the manufactured GBTA showing the ‘front side’ of the LPBF system, gas flow direction and recoater direction, and c) Side view of the manufactured GBTA showing the depicting and the base plate

Such as for one flatness tolerance zone for a feature, ten data points were collected on the surface to calculate it. The measurement process for this study is divided into four major geometric categories i.e.: circle, cylinder, line, and a surface. The procedure adopted for measurement for each geometry is listed below [BS 7172]:

- Circle: It is measured using 10 equally spaced points around the circular cross section.
- Cylinder: It is measured using total 15 points with 5 points equally spaced distributed at three cross-sections of the cylinder at height h_1 , h_2 and h_3 . (Refer Figure 29)
- Line: It is measured using 10 points equally spaced along the length of line to cover at least 90% of the length of the line.
- Surface: It is measured using 10 points with their random distribution over the surface to cover the maximum area of the surface.

The schematics of the measurement strategy is shown in Figure 29. The red dots represent the locations where the CMM probe will record the measurement data.

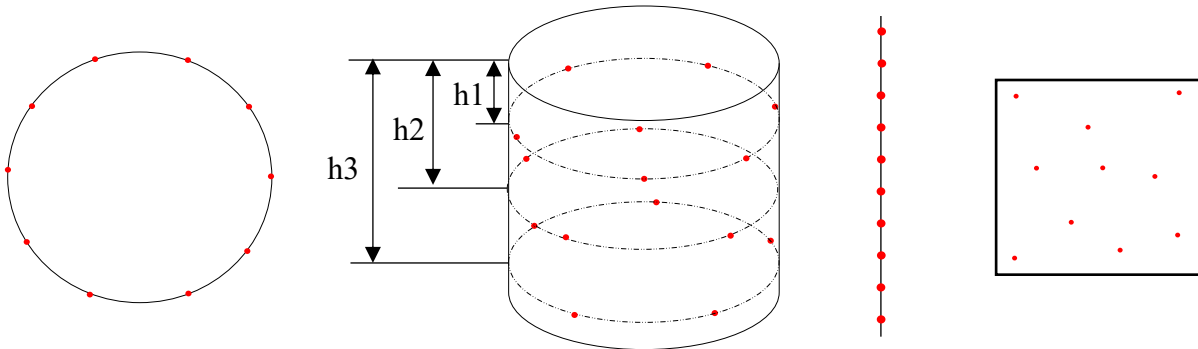


Figure 29. Measurement strategy for different features. The red dots represent the locations where the CMM probe will record the measurement data.

The method of least squares was used to define planes and cylinders in the CMM for computing the GD&T tolerance zones. A coordinate system is defined to perform the measurements of the GBTA. There are two coordinate systems in the CMM. One is the coordinate system of CMM itself. It defines the motion of the probe in 3 directions referred to as X, Y and Z direction for the CMM. The second is the part coordinate system that is defined using the GBTA. In the CMM, surface-line-line method is used to set the part coordinate system [Hocken et al., 2012]. Part co-ordinate system is depicted in Figure 30. The top surface of the base of the GBTA on which most of the features are built is defined as the XY plane. The features categorization as per the GD&T are shown in Table 16. The results are discussed in the last section of the chapter as per the GD&T characteristic.

For a second round of measurements without the base plate, first the base plate was removed from the GBTA using a band-saw. The support structures were also removed manually using hand tools. The GBTA after the removal of the base plate and support structures is shown in Figure 30. And for fixing the GBTA after the removal of the base plate on the CMM table, special fixtures were used. These fixtures were designed as per the GBTA dimensions and manufactured using polymer 3D printing.

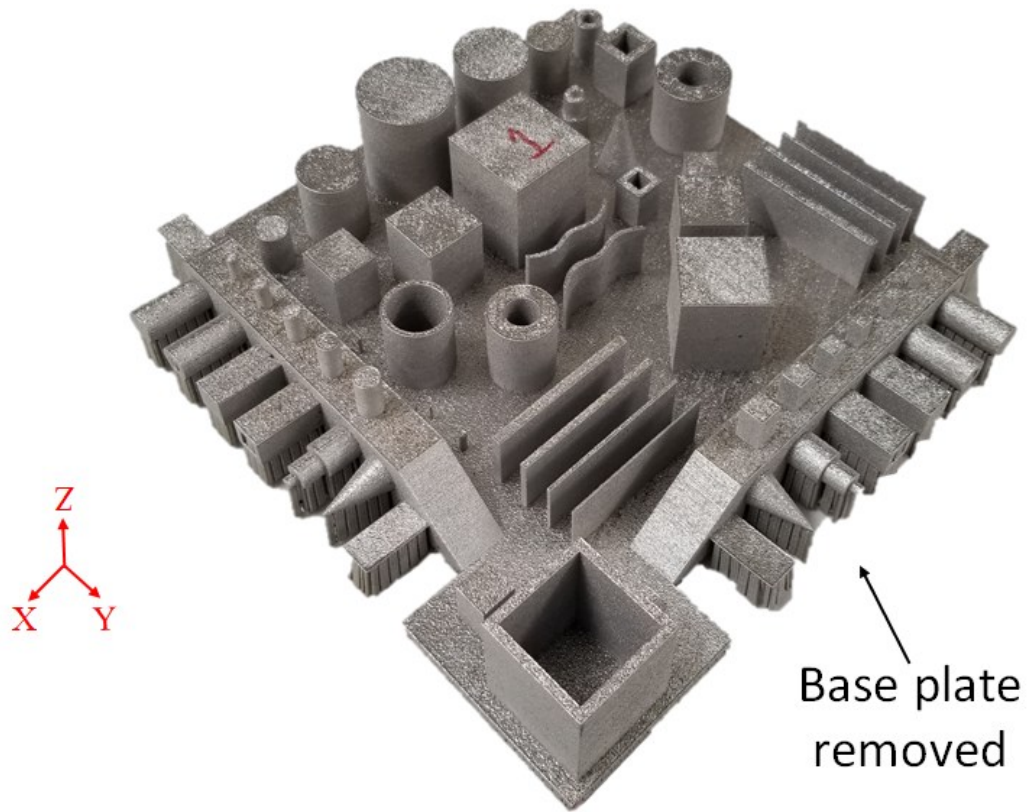


Figure 30. GBTA after the removal of the base plate. a) Isometric view, b) Side view showing warped features

Table 16. Feature categorization based on GD&T characterization

#	GD&T characteristics	Features Categorization
1	Straightness	Features with straight line – flat surfaces of cuboids and thin sheets.
2	Flatness	Features with flat surfaces - cuboids, top surface of cylinders.
3	Perpendicularity	Flat surfaces of cuboids and thin sheets with respect to a planar surface as a datum feature.
4	Parallelism	Features with flat surfaces parallel to a planar surface as a datum feature
5	Angularity	Angular features with respect to a planar surface as datum feature.
6	True Position	Cylindrical and planar features with respect to a datum coordinate system.
7	Circularity	Cylindrical features – Circular periphery on outer surface of cylinders and hollow cylinders.
8	Cylindricity	Cylindrical features.
9	Concentricity	Stacked cylindrical features
10	Circular run-out	Stacked cylindrical features
11	Total run-out	Stacked cylindrical features

5.3. Numerical simulation

To assess the ability of the thermo-mechanical simulation tools, and to predict GD&T without experimentation, a thermo-elastic finite element model was implemented in Autodesk Netfabb Local Simulation. First, the part and support structures were imported to Autodesk Netfabb Local Simulation. Then, a process parameter file (PRM) was generated by conducting a micro-scale simulation using the experimental parameters for SS 316L material. The micro-scale simulation involves a non-linear thermo-mechanical simulation in which the element dimensions are equal to the melt pool dimensions. Elements of the currently fused powder and solid metal are kept fine to make sure that the temperature gradient, nodal deviation and stress values are captured precisely.

Now the thermal history and the micro-scale mechanical simulation results are fed into the process parameter file which is then used to calculate part scale simulation results and part scale temperature history. The process parameters used were the same as the ones used in the experimental study and are described in Table 15. The simulation parameters shown in Table 17. Temperature dependent material properties for SS 316L were based on data from references [Hodge et al., 2014; Peng et al., 2018]. The PRM file is used for conducting a macroscale simulation of the GBTA part [Gouge et al., 2019]. The boundary conditions for the macroscale model were as follows:

- Mechanical boundary conditions: The bottom nodes of the base plate were fixed, i.e., a zero displacement is imposed in all directions. At the other boundaries, a zero normal stress boundary condition is used.
- Thermal boundary conditions: A convective heat transfer boundary condition is considered between the powder and the environment. The heat loss coefficient value of 20 W/m²/K is used [Zhang et al., 2017].

The LPBF process governing equations are explained in the following sub-section.

5.3.1. Governing equations and boundary conditions

A sequentially coupled analysis is conducted in which the temperature field is solved first and then used to perform the mechanical analysis. The major mode of heat transfer is conduction through the base plate, which is initially at ambient temperature and is mechanically held by fixing the bottom face at zero displacement. Free convection and radiation are used for heat transfer from the surface of the model. These boundary conditions aim at reproducing the conditions observed during manufacturing. For removing the base plate, the boundary condition of zero displacement is shifted to the center-bottom of the GBTA so that it can be held stationary from the center and can still give reliable warpage/deviation information.

For obtaining the temperature field, $T(x, y, z, t)$, the 3D transient heat conduction equation is solved, i.e.,

$$Q(\mathbf{x}, t) - \nabla \cdot \mathbf{q}(\mathbf{x}, t) = \rho C_p \frac{dT}{dt} \quad (6.3)$$

where ρ is the material density, C_p is the specific heat capacity, t is time, T is the temperature, Q is the internal heat generation per unit volume (Goldak's 3D Gaussian ellipsoidal distribution [Gouge

et al., 2018]), x is the relative reference coordinate, and \mathbf{q} is the heat flux. The heat flux is given by:

$$\mathbf{q} = -k\nabla T \quad (6.4)$$

where k is the thermal conductivity of the material.

The heat flux on the surface accounts for both convection and radiation heat loss. Convective heat loss is estimated using Newton's law of cooling, i.e.

$$q_{conv} = h(T_s - T_a) \quad (6.5)$$

where h is the heat transfer coefficient for convection, T_s is the temperature on the surface, T_a is the ambient temperature.

Radiation heat losses are estimated using Stefan-Boltzmann's law, i.e.,

$$q_{rad} = \varepsilon\sigma(T_s^4 - T_a^4) \quad (6.6)$$

where ε is the emissivity of the material, and σ is the Stefan-Boltzmann constant.

The initial thermal condition is that the temperature of the material is T_a .

The mechanical response is governed by the steady-state linear elastic equation,

$$\nabla \cdot \boldsymbol{\sigma} = 0 \quad (6.7)$$

where $\boldsymbol{\sigma}$ is the stress and is related to strain using Hooke's law:

$$\boldsymbol{\sigma} = \mathbf{C}\boldsymbol{\varepsilon}_e \quad (6.8)$$

\mathbf{C} is the material stiffness tensor. The total strain is calculated based on the small deformation theory and is given below:

$$\boldsymbol{\varepsilon} = \boldsymbol{\varepsilon}_e + \boldsymbol{\varepsilon}_p + \boldsymbol{\varepsilon}_t \quad (6.9)$$

where $\boldsymbol{\varepsilon}_e$ is the elastic strain, $\boldsymbol{\varepsilon}_p$ is the plastic strain and $\boldsymbol{\varepsilon}_t$ is the thermal strain. The thermal strain is calculated using the thermal expansion equation:

$$\boldsymbol{\varepsilon}_t = \alpha [T(x, y, z, t) - T_{ref}] \quad (6.10)$$

where α is the thermal expansion coefficient and T_{ref} is the reference strain-free temperature. The plastic strain is calculated using the von-Mises yield criterion and the Prandtl-Reuss flow rule as given below.

$$\Delta\boldsymbol{\varepsilon}_p = \Delta\boldsymbol{\varepsilon}_q \boldsymbol{\alpha} \quad (6.11)$$

$$\boldsymbol{\alpha} = \left(\frac{\partial f}{\partial \boldsymbol{\sigma}} \right)^T \quad (6.12)$$

$$f = \sigma_m - \sigma_y(\epsilon_q, T) \leq 0 \quad (6.13)$$

Where the change in plastic strain ($\Delta\varepsilon_p$) is calculated using the change in the von-Mises strain ($\Delta\varepsilon_q$) for each time-step and the flow vector (α). Flow vector is calculated using the yield function (f). Where σ_m is von-Mises stress and σ_y is yield stress. The total strain values are used to calculate the nodal displacements using strain-displacement relationships. The base plate is fixed at the bottom to prevent rigid body motion.

The input STL along with supports is shown in Figure 31 a) and the mesh strategy is shown in Figure 31 b). After a solution has been obtained, the predicted displacement field is used to construct a deviated GBTA part. The deviated STL files are imported to *GOM Inspect* for extracting GD&T quantifiers for a one-to-one comparison with the experimental results. Figure 32 shows the process of constructing fitted features on the deviated STLs from simulations and extracting the GD&T characteristics. The deviated STL file is first converted into point cloud. Standard geometric shapes are then fitted into the individual features of the deviated point cloud such as cylinder or plane. GD&T definitions are then used to find the tolerance zones on these fitted features. The GD&T results from simulation (both with and without base plate) are discussed along-side experimental results in the next section for analytical comparison and physical interpretation.

Table 17. Simulation parameters

Simulation parameter	Value
Heat source absorption efficiency (%)	35
Analysis type	Thermal and mechanical
Structural plasticity	ON
Mesh approach	Layer based
Maximum mesh adaptively levels	5
Coarsening generations	1
Layers per mesh element	20

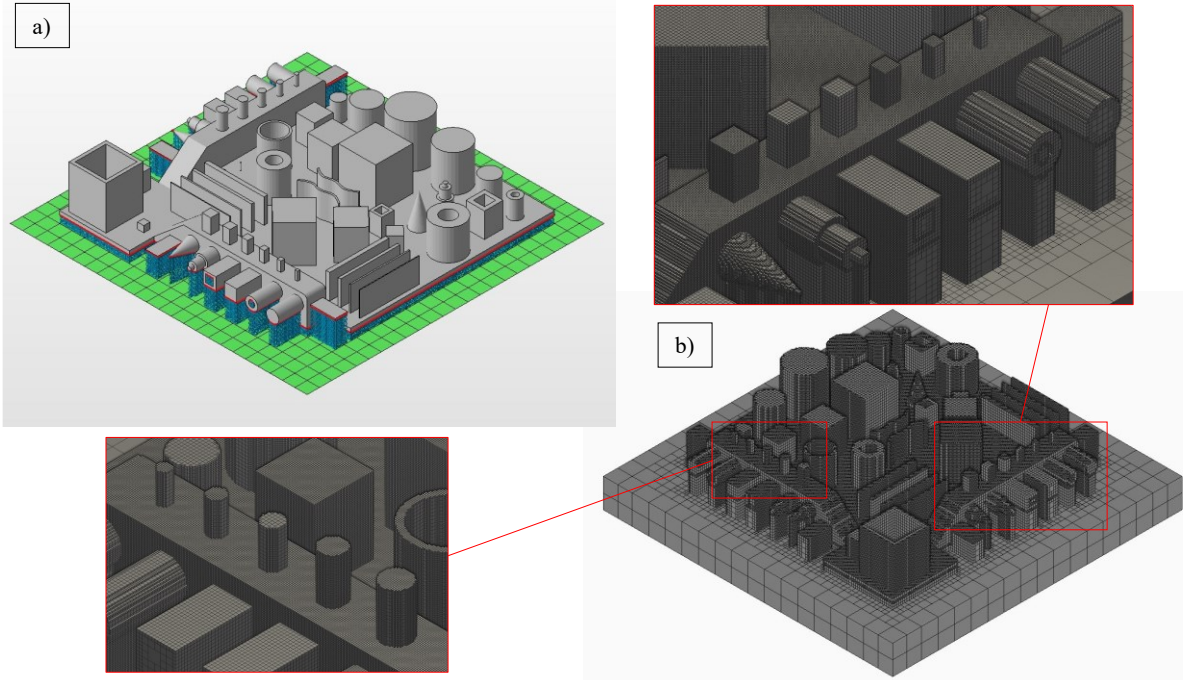


Figure 31. a) GBTA with supports (in blue), b) Layer based adaptive coarsening mesh

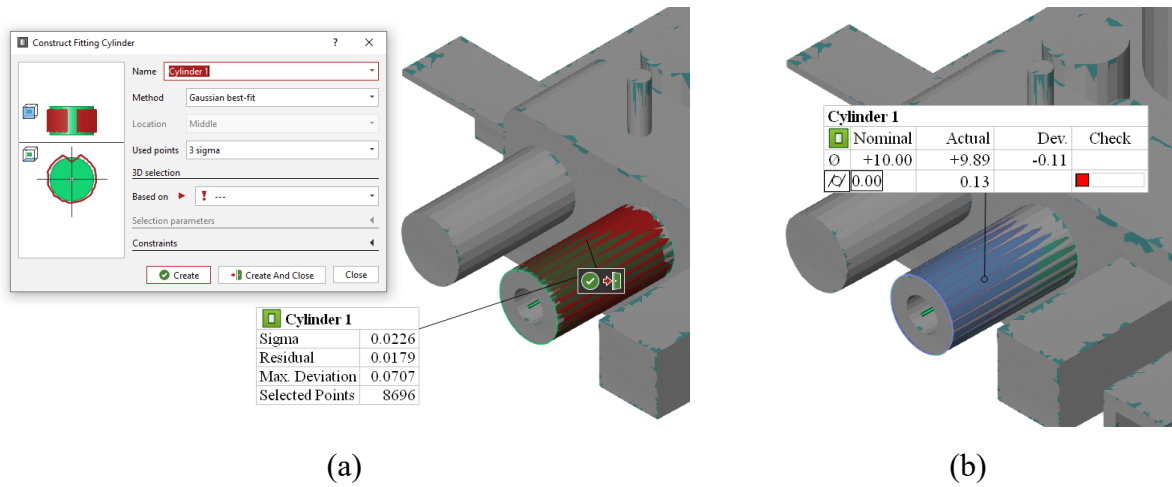


Figure 32. Extraction of GD&T a) Construction of fitting feature on deviated STL, b) Extraction of GD&T characteristics based on the constructed feature

5.4. Results and discussions

The measurement data from the experiments and predicted deformed geometry from simulations is used to extract GD&T characteristics. One of the key reasons to run the numerical simulations is to predict the stress distribution and nodal deformations which are discussed below.

The equivalent von Mises stress in the manufactured part with the base plate intact is shown in Figure 33. The maximum stress region is shown by a red arrow in Figure 33. The minimum stress regions are on the base plate itself, and on some of the features which are overhanging with ample support structures to hold them such as the overhanging thin sheet pointed out by the green arrow in Figure 33. This occurs because the previously manufactured material retains the thermal expansion, it results in compression in the layers manufactured afterwards and puts the already manufactured layers into tension which then distorts inwards. After the part is manufactured and has reached room temperature, it contracts (shrinks) leading to overall residual stresses in the part. This thermal expansion-contraction phenomenon of the LPBF process is similar to the thermal characteristics during the welding operation [Michaleris, 2011]. However, when the base plate and the support structures are removed, the residual stress is relieved and the average stress values decrease in the GBTA as seen in Figure 34. It is to note that the regions of the maximum and minimum stress regions are also inverted.

The deviation maps with and without base plate are shown in Figure 35 and Figure 36. It is seen that the maximum deviation values have increased about three times from 0.346 to 0.904 mm. This is because the residual stresses are released from the part after the base plate and support structures are removed and in turn the resultant deviations rise. An important aspect to note here is that although stress distributions and deviation maps give a fair idea about the residual stress regions, deviation regions, and regions susceptible to defects, they cannot provide quantitative information about the geometric tolerances and assemblability of the manufactured part. So apart from analyzing and minimizing the deviation residual and residual stresses, post-processing analysis to GD&T is needed. Using numerical simulation results, the GD&T for each feature are extracted and compared with the experimental results. The GD&T characteristic data from the experimental and simulation results, with and without the base plate are presented in the following sub-sections to have a comparative analysis and discussion. Further, their interlinkage with the regions' residual stresses and deviation maps is also discussed.

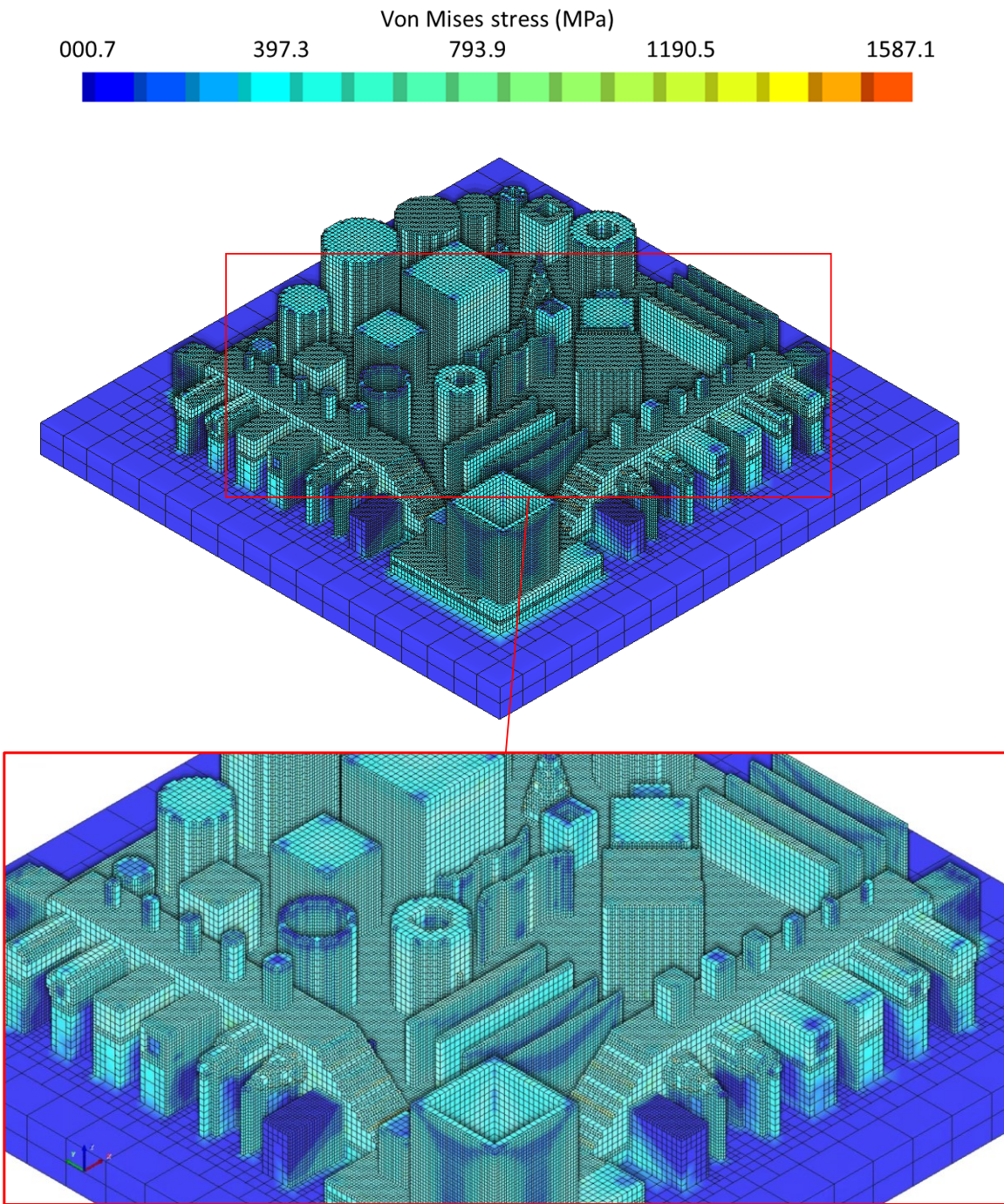


Figure 33. von Mises stress distribution of the GBTA with the base plate intact.

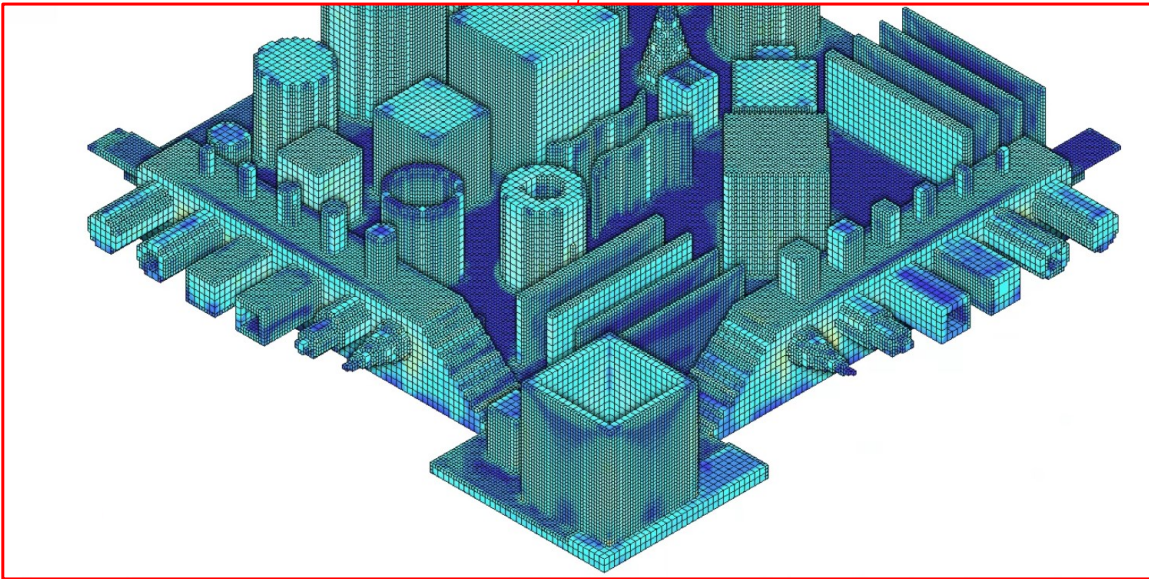
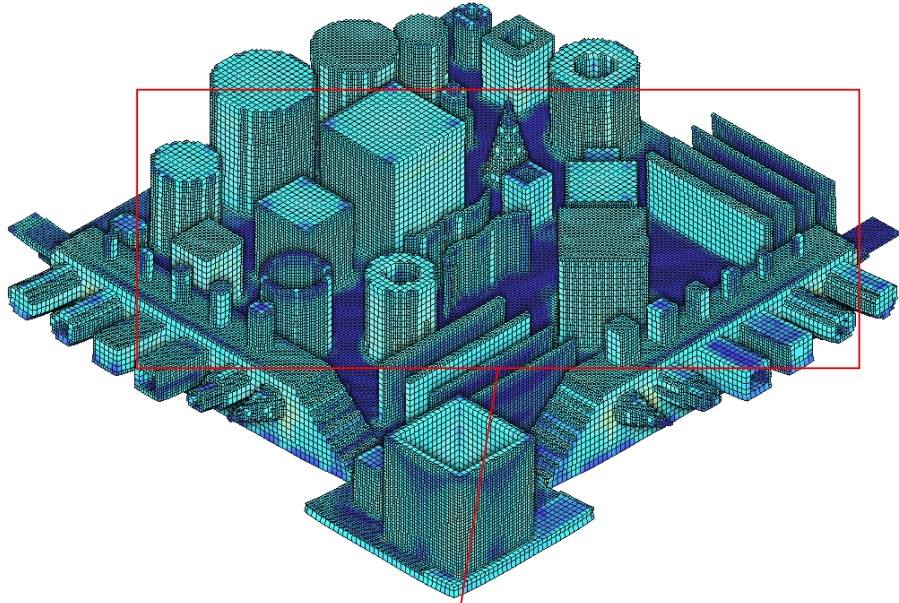
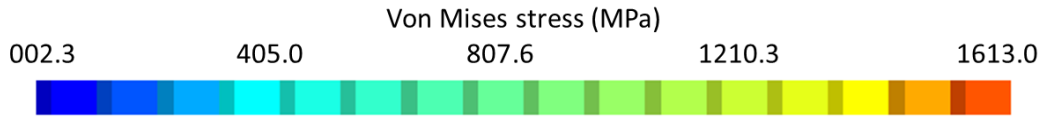


Figure 34. von Mises stress distribution of the GBTA after removal of the base plate

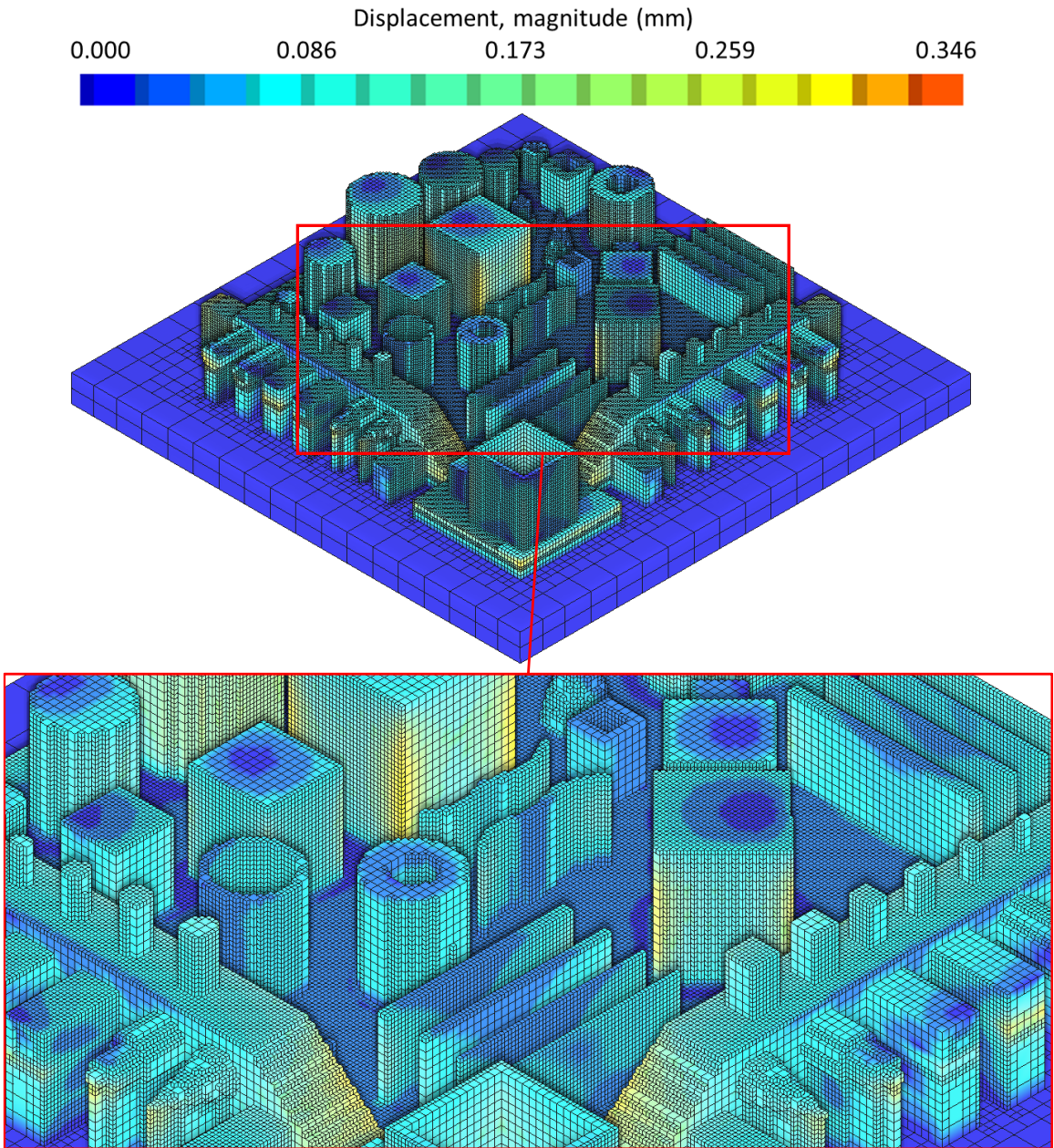


Figure 35. Overall deviations of the GBTA with the base plate intact

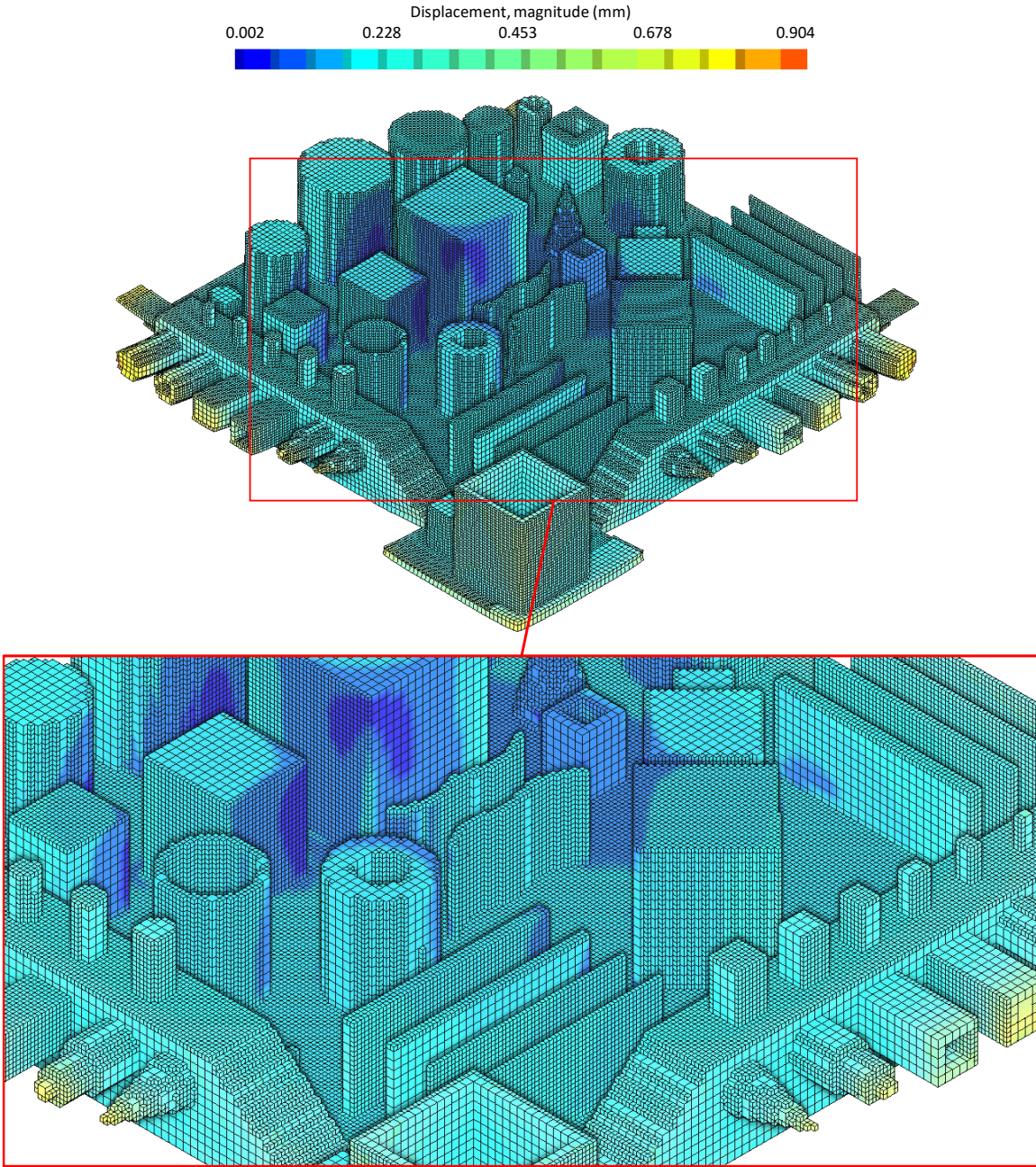


Figure 36. Overall deviations of the GBTA after removal of the base plate

5.4.1. Straightness

The straightness tolerance is computed for the features and categorized as per the feature orientation to the reference planes – XY, YZ, and ZX. Results for features parallel to reference plane XY are shown with bars labelled as XY in the Figure 37. A similar approach is used for YZ and ZX. For the experimental measurements, the sample space contains 13 features with feature

axis aligning with XY plane and 8 each for YZ and ZX planes. For example, the first XY bar in Figure 8 shows the experimental results for average tolerance zone for the 13 features aligned to XY plane with the base plate intact on the GBTA.

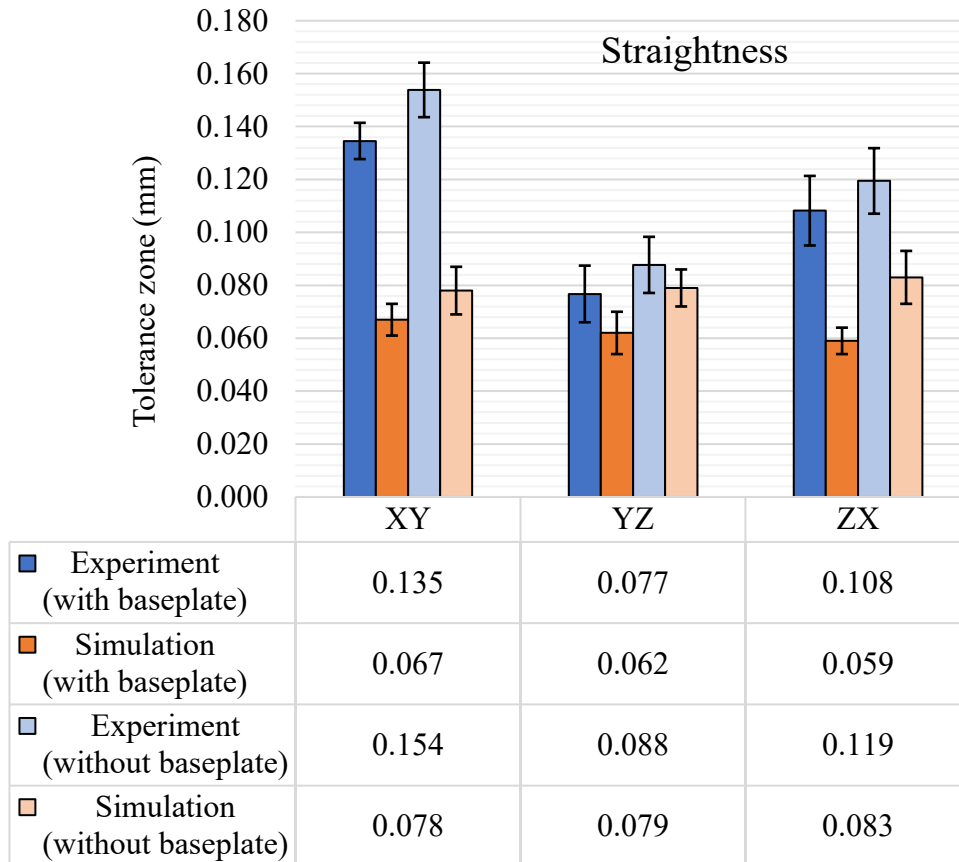


Figure 37. Straightness tolerance results with and without base plate

Experimental results show that the straightness tolerance is anisotropic with respect to the reference planes since the results are different in all three principal planar directions along with variation in standard deviations. The straightness tolerance is higher in the XY planar direction because the measurements are performed on as-built parts without any post-processing, therefore the effect of hatching cannot be ignored on this plane. The effect is increased by the chessboard (or checkerboard) style hatching, in which the laser movement is multi-directional, and it creates a crisscross waviness on the surface. The hatching effect is maximum on surfaces parallel of XY plane as it is the plane on which the laser moves while the part is building. In general, the

straightness tolerance results spike by 0.015 to 0.020 mm in all three planar directions after the removal of the base plate, which is anticipated as the residual stresses are released after the base plate removal which in turn increase the deviations. Even with a larger curvature on the base feature of the GBTA after the removal of the base plate, the form tolerances such as straightness are less affected, as they are independent of datums. The largest straightness tolerance zone was observed on a thin sheet in XY plane. It is 0.158 mm with base plate and 0.183 mm without the base plate. The large tolerance zone resulted due to the low thickness value, i.e., 0.500 mm of the sheet, which lead to larger deformations during the rapid cooling of the part throughout the process.

Figure 37 shows that the predicted straightness tolerances by numerical simulation. The simulation results closely follow experimental results in the YZ plane. However, the simulation does not capture the anisotropy in the deviations and the therefore overpredicts the tolerance zone in XY plane. It is hypothesized that the reason for the major variation in the straightness tolerance of XY plane is that the surface waviness due to the hatching is not captured well by the simulations. The difference in results is in the same range than the generic surface waviness values for LPBF manufactured SS 316L parts [Barari et al., 2017]. The difference in experimental results in YZ and ZX plane is also not completely captured by simulations. Since straightness is a form tolerance and the boundary conditions have a maximum effect on the form tolerances, the ‘uniform heat loss condition’ could be one reason for this similarity in simulation results for YZ and ZX planes. The standard deviations for the straightness tolerance of XY plane are almost the same for experimental and numerical results, with and without base plate. The difference in both standard deviations is only ± 0.001 mm.

5.4.2. Flatness

The sample space for flatness tolerance contains 20 features for the XY plane, 25 features for the YZ plane and 24 features for the ZX plane. The flatness results for both experiments and simulations are shown in Figure 38, with a comparison between with and without base plate removal.

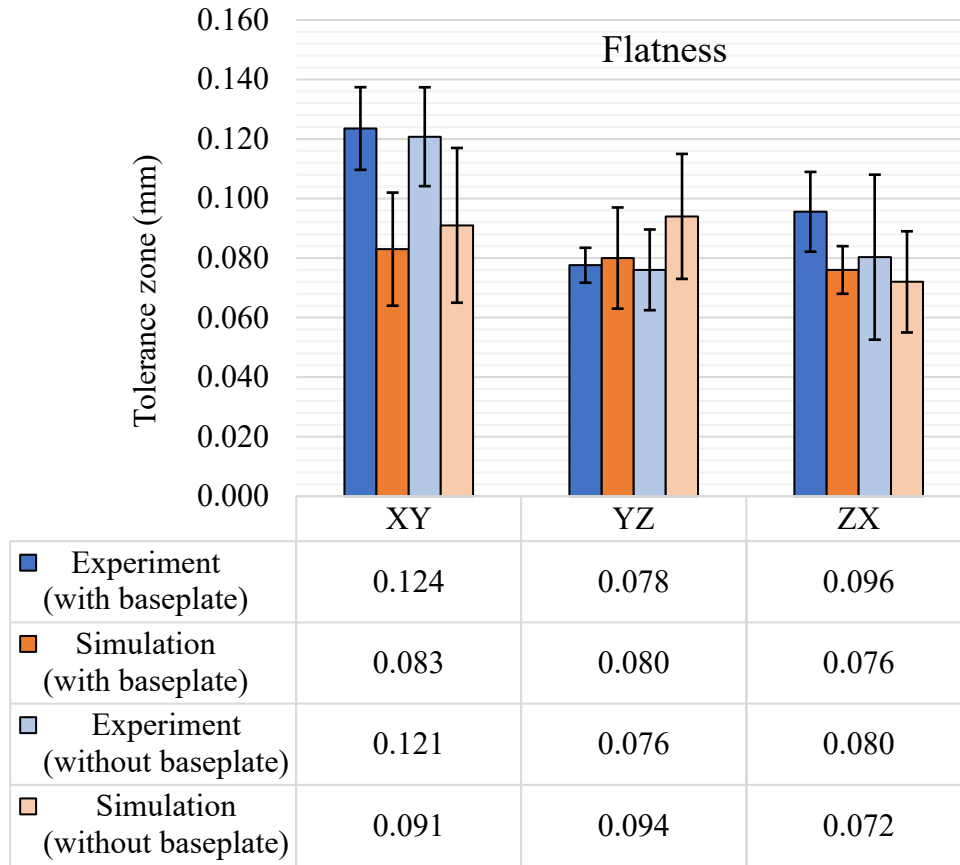


Figure 38. Flatness tolerance results with and without base plate

Much like straightness results, anisotropy of experimental results is observed for flatness tolerance as well. The largest tolerance bands with and without base plate are observed for the XY plane and the smallest for the YZ plane. Maximum tolerance bands are observed for the XY plane for both with and without base plate conditions. It is because the XY plane is the building plane, which also bears the effect of in-plane shrinkage during the building of the part. Further, the release of the residual stress with the removal of the base plate also affects the XY plane to the highest degree as the base feature of the GBTA is parallel to the XY plane, on which all the features are mounted. Since flatness tolerance is spread over the complete region of the feature, even the minor curvatures and warpage due to the removal of the base plate affect the tolerance zone. A large standard deviation in results for the ZX plane without the base plate is observed, i.e. standard deviation of 0.056 mm. This could be due to the recoater direction which is perpendicular to the

ZX plane and affects the layer edges during the building, hence reducing the surface quality of the ZX walls.

Looking at the simulation results in Figure 38, an overall lower range of flatness tolerance is observed as compared to experimental results except for the YZ plane. For both experiments and simulations, the standard deviation of the results increases with the removal of the base plate. It shows that with the removal of the base plate some of the surfaces are warped to a larger extent leading to a rise in standard deviation. Such as features 4, 5, 18 and 19 show an approximate rise of 0.020 mm in flatness for the XY plane after the removal of the base plate as they are closer to the edge and are most affected by the warpage of the GBTA base feature. An interesting result to notice is the standard deviation of the ZX plane with the base plate reduces to 0.016 mm from 0.026 mm. The possible reasoning behind this could be that the features which had larger flatness tolerance bands experienced warpage in such a way after the base plate removal that the flatness values dropped.

5.4.3. Circularity

The measurements are done for different cylindrical and conical features with their axis aligned to respective reference axial directions – X, Y, and Z. The tolerance zones are computed for these categories of features, and is represented in the bar chart in Figure 39. The sample space contains 6 features each for X and Y axes direction and 26 features for Z-axis direction. The larger number of features in the Z direction are varying in size and volume to get a detailed account of the circularity variation in the principal build axis, i.e. Z-axis.

For experimental results, the circularity tolerance zone with the base plate intact is around 0.104 mm for all three axial directions. However, the standard deviation is highest for the Z-axis i.e. 0.040 mm and without the base plate is even more at 0.052 mm. In the Z direction, the standard deviation is maximum without the base plate results at 0.052 mm. One reason is the effect of the removal of the base plate and the other reason is a large number of features in the Z direction. However, since circularity is measured on features with diameters, the change in diametric value also leads to a change in circularity. Trends for circularity vs. diameter in the Z-axis direction are shown in Figure 40. Similar results are observed for experimental circularity tolerance after the removal of the base plate.

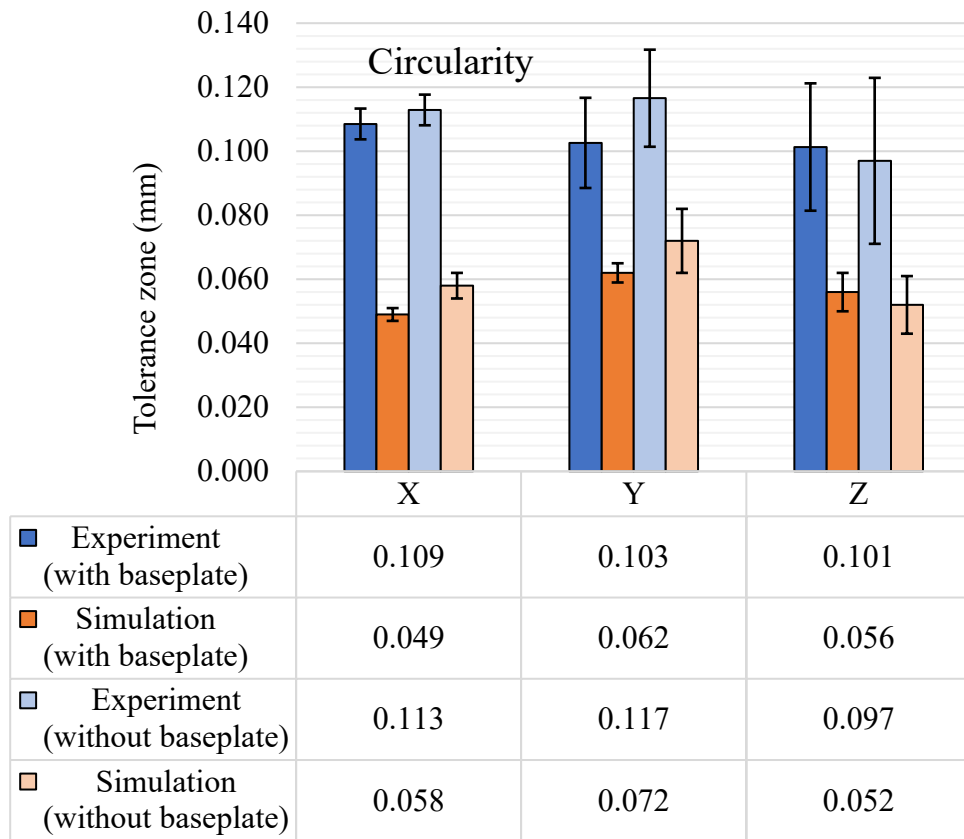


Figure 39. Circularity

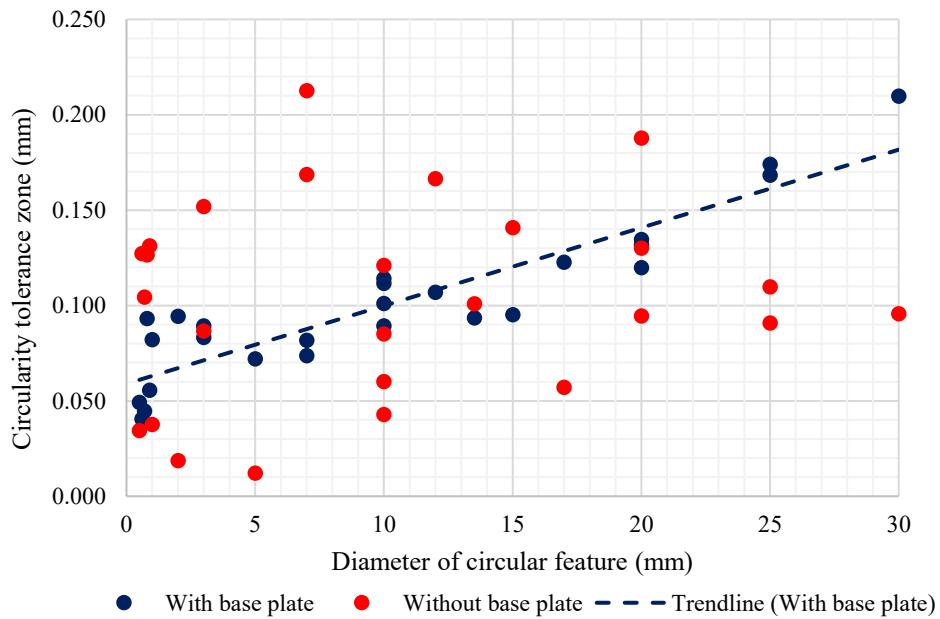


Figure 40. Diameter vs circularity (Experimental)

For circularity with the base plate, a clear relationship is observed, i.e. the circularity tolerance zone increases with the increase in the diameter. It is also depicted by a linear trend line. However, after the removal of the base plate large variations are observed especially with smaller diameter features, and a clear trend cannot be found.

In the simulation results, the overall mean shift of around 0.040 mm is observed in all directions for results with and without base plate. The major reason for this mean shift could be the generic under-prediction observed in the deviation simulation and the inability of the simulation to capture the meso level surface variations. Apart from this mean shift and low standard deviation the simulation results follow a very similar trend to experimental results especially for results after removal of the base plate. Unlike experimental results, no trends are observed in the simulation results for the dependence of circular feature diameter with the circularity tolerance.

5.4.4. Cylindricity

The sample space contains 6 features each for X and Y direction and 25 features for Z directions. The diameter of cylindrical features varies from 0.5 mm to 30 mm. Cylindricity tolerance results are shown in Figure 41. Unlike circularity, the directional results after the removal of the base plate are not in a similar range for the three principal axial directions. The results in axial direction X show the highest peak in the experimental cylindricity tolerance zone as well as a standard deviation hike. One reason for this huge variation is the large support structures which decrease the dimensional fidelity of the features, and along with the residual stress release, another reason could be the cantilever effect due to the nature of the geometric form of the feature [Li et al., 2017]. The effect of the diameter was also studied for cylindricity tolerance zones, and the results are shown in Figure 42. A linear trend is observed with the cylindricity tolerance zone getting wider with an increase in the diameter of the cylindrical feature. Even with a few outliers with small diameter features, both sets of results (with and without base plate) show a similar trend. The results without the base plate are offset with an additional 0.040 – 0.050 mm.

Simulation results for cylindricity with the base plate intact are in close range with the experimental results. Unlike the large rise of the cylindricity observed in X-axis direction for the experimental results without the base plate, the simulation does not show any such anomaly. A rise in cylindricity for the features in the X direction (such as features 2, 3 and 6) is still observed

in simulation results similar to experimental results due to the removal of the base plate and support structures. However, the rise in the cylindricity tolerance with the removal of the base plate is still lower as compared to the tolerance increase seen in other form tolerances. This is because Cylindricity tolerance is based on the form of the cylindrical features but not on the orientation, and with the removal of the base plate maximum effect is seen on orientation as compared to the form of cylindrical features. Unlike experimental results, no trends are observed in the simulation results for the dependence of cylindrical feature diameter with the cylindricity tolerance.

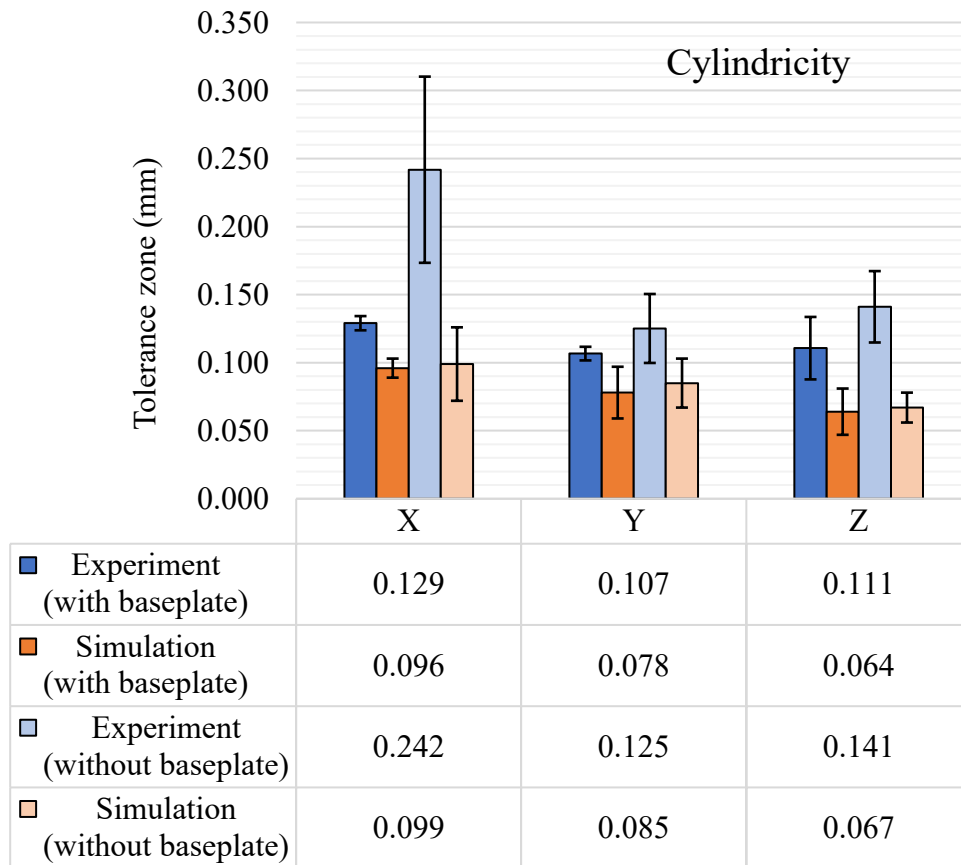


Figure 41. Cylindricity

Overall, analysis of results for the form tolerances shows a generic increase in tolerance zones after the GBTA is removed from the base plate. It can directly be linked to the release of the residual stress within the GBTA. Also, the increase in standard deviation suggests similar reasoning. Apart from that the process parameters and laser-material interaction have also a

significant effect which will become clearer when the results will be analyzed for a set of process parametric variations. As of now, it can be stated that for the selected process parameters and SS 316L material the form tolerances are generally in the range of 0.050 to 0.130 mm with a few exceptions such as the spike in Cylindricity in X-axis direction after removal of the base plate.

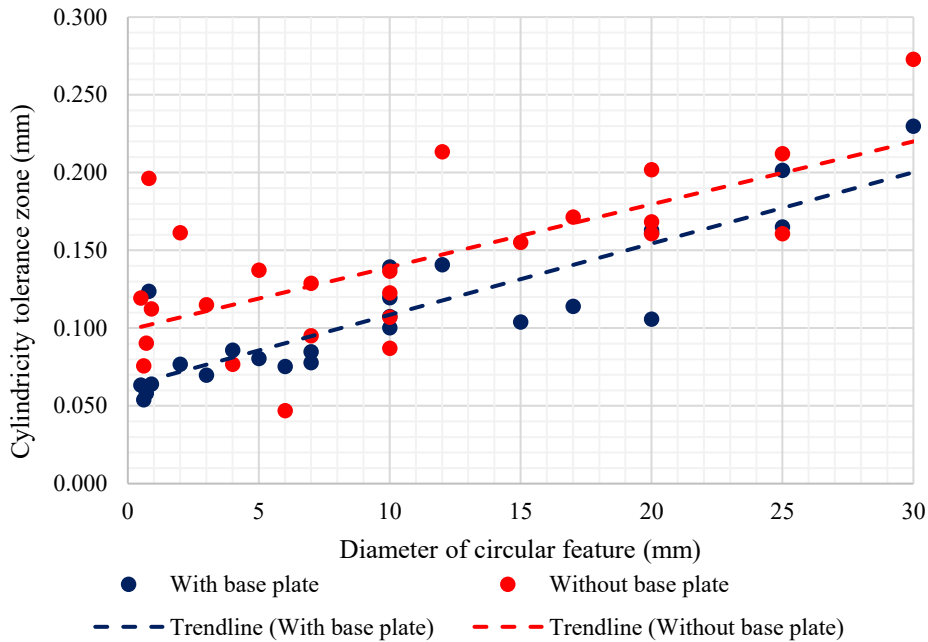


Figure 42. Diameter vs cylindricity (Experimental)

5.4.5. Perpendicularity

The GBTA contains 16 features for the XY plane and 18 features for each of the YZ and ZX planes on which perpendicularity is measured. The perpendicularity tolerance zone results are shown in Figure 43. For experimental perpendicularity, the standard deviation increases by a factor of two when the base plate is removed. It shoots to 0.054 mm from 0.024 mm. The maximum experimental tolerance bands are observed in the XY plane. The simulation results for perpendicularity are in very close range with the experimental results with few exceptions. The major variation consistently observed in the perpendicularity results is that the perpendicularity is minimum in the YZ plane for the experimental results but for simulation results, it is for the ZX plane. Also, the simulation results in the YZ plane overshoot the experimental results, which is not the usual case in all other tolerance characterizations and simulation results. Since perpendicularity

is an orientation tolerance, the flatness of the datum plane affects the tolerance zone which is seen in both experiments and simulations. The variation in the flatness of the datum planes also propagated the tolerance zone to the perpendicularity results. This could be the major reason for the inconsistencies and variations in the results.

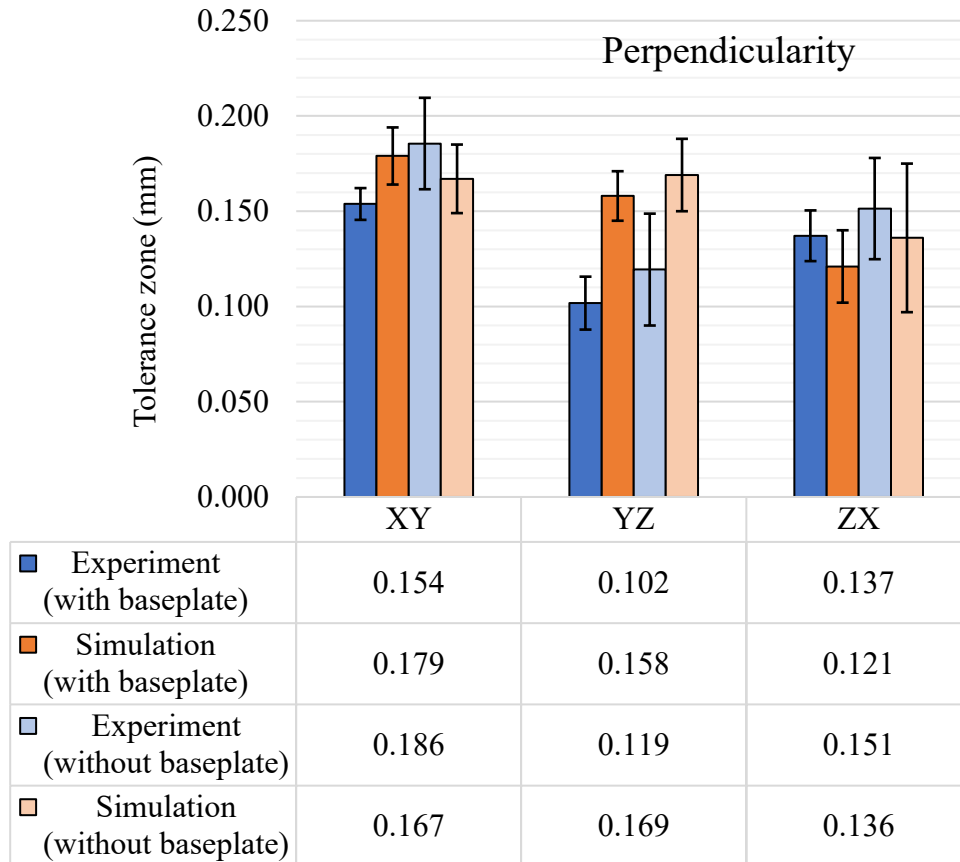


Figure 43. Perpendicularity

5.4.6. Parallelism

The sample space for parallelism tolerance contains 15 features for the XY plane and 13 features each for YZ and ZX planes. Parallelism results from both experiments and simulation are shown in Figure 44. The experimental results show the anticipated increase of tolerance zone after the removal of the base plate. The standard deviations values are different for each planar direction but the average standard deviation for the three planes remains similar for both with and without base plate results. The results with the base plate for XY and YZ are comparable however there is a rise of around 0.020 mm in the ZX plane. The results without the base plate show the highest

average tolerance zone of 0.215 mm for the YZ plane. In general, the small-sized features show a larger parallelism tolerance zone with the base plate intact. However, after the removal of the base plate, the tolerance zone variation in the small features is less than the tolerance zone variation in the large features.

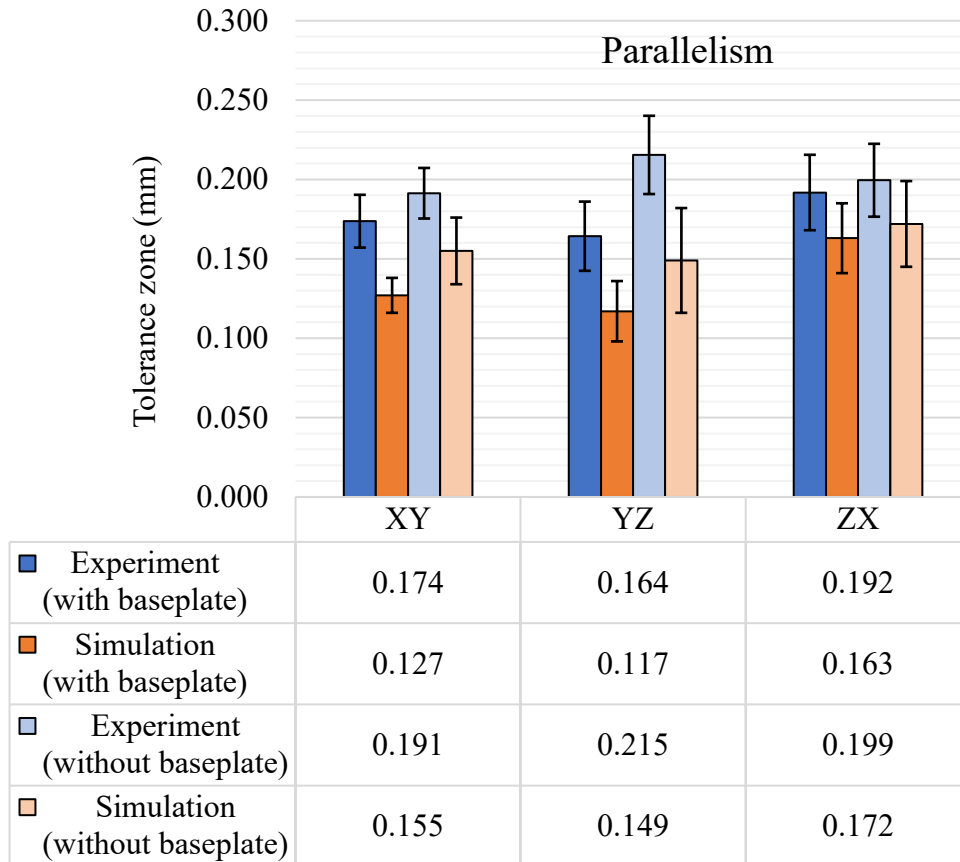


Figure 44. Parallelism

So, the increase in the average tolerance zone after the removal of the base plate is mostly due to the larger size features as they are susceptible to more warpage and deformation with the release of the stress. The simulation results show a very similar trend for variation between the planes especially for results with the base plate. The planar variation exactly follows the same trend with the highest ZX plane tolerance zone with a similar standard deviation, however, the zone is 0.036 mm smaller than the experimental results. The same variations are not observed in the results without the base plate. Also, the standard deviation for results without the base plate rise by 0.014 mm from experimental to simulation results.

5.4.7. Angularity

Angularity measurements are done for two planar features that are at 40 degrees angle to the XY plane and are shown in Figure 45. The experimental angularity increases after removing the base plate. For simulations, the rise in tolerance zone after the removal of the base plate is similar at 0.003 mm. However, the average tolerance zone is higher by 0.008 mm i.e., at 0.091 mm with the base plate compared to 0.083 mm experimental value.

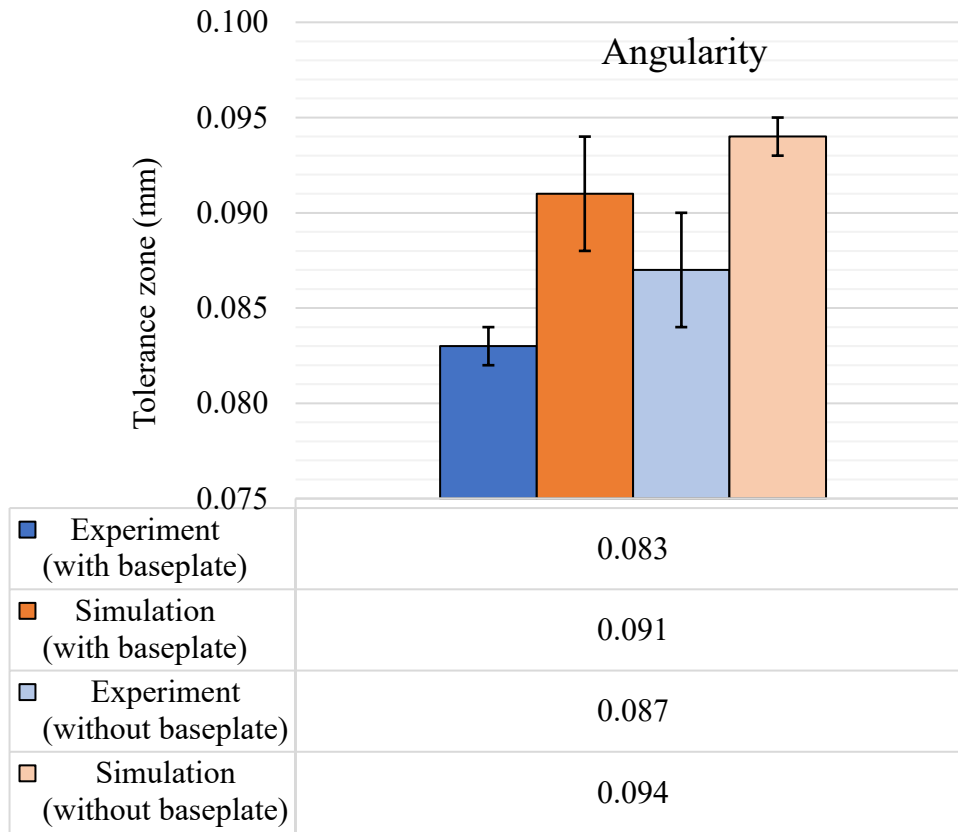


Figure 45. Angularity

5.4.8. Concentricity

Concentricity tolerance is an important location tolerance for deciding the location of one cylindrical feature with respect to another and plays a major role during assembly operations. The concentricity results are shown in Figure 46. Experimental concentricity results for the base plate intact and without the base plate follow similar trends with maximum tolerance zone in Y-axis and minimum in Z-axis. It is to note that among all the GD&T characteristics discussed above,

concentricity has the largest tolerance zones. It is due to the composite nature of the concentricity tolerance, as it also depends on the form of the cylinders and the axial shift of the cylindrical features with respect to each other. Even with two features per axis and three measurements per feature, the standard deviation is large. The simulation results also follow suit with average concentricity tolerances highest along the Y-axis and minimum along the Z-axis with an increase in tolerance zone after the removal of the base plate. The standard deviations for the simulation results are also closely following the experimental results.

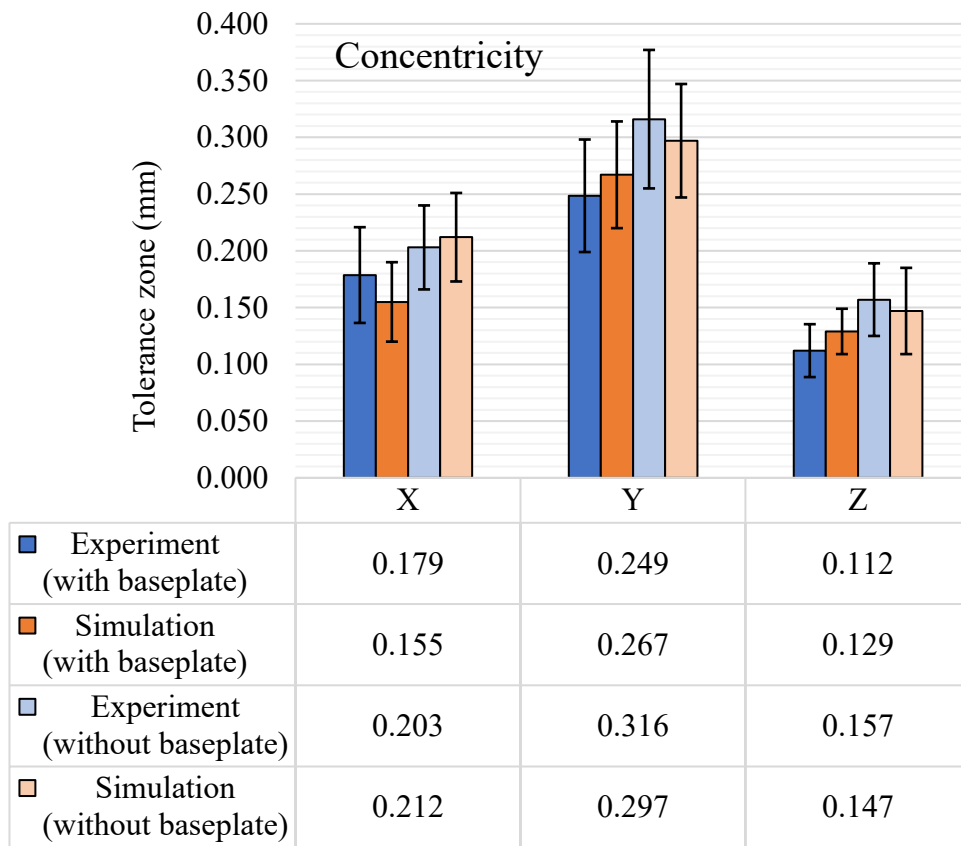


Figure 46. Concentricity

5.4.9. Position

The GBTA features were positioned evenly on the base to study the position tolerance both for planar and axial positions and the results are shown in

Figure 47. The planar position variation is highest in the YZ plane for all the results. The YZ plane is perpendicular to the recoater direction and the recoater movement and powder spreading could

be the most significant reason for these large tolerance zones. A similar trend is observed in the simulations as the simulation solver also considers the recoater direction and the recoater interference. With the rise in the tolerance zone, the standard deviations also get wider for the YZ planar direction results. For axial position tolerance, cylindrical features were used across the entire GBTA, and the results are shown in Figure 48. The experimental and simulation results are consistent in variation trends across the axis. In axial position, the Y-axis tolerance zone is highest for both experimental and simulation results. Simulation results have underpredicted the position tolerance for both planar and axial features. The standard deviations are much higher than any standard deviations observed for other GD&T characteristics, which is because the tolerance values are quite higher than other tolerance characteristics for some of the positional features. The exact reasoning behind this large shift is still unknown but most logical speculation is recoater direction effect and the micro-mirror orientations governing the laser beam.

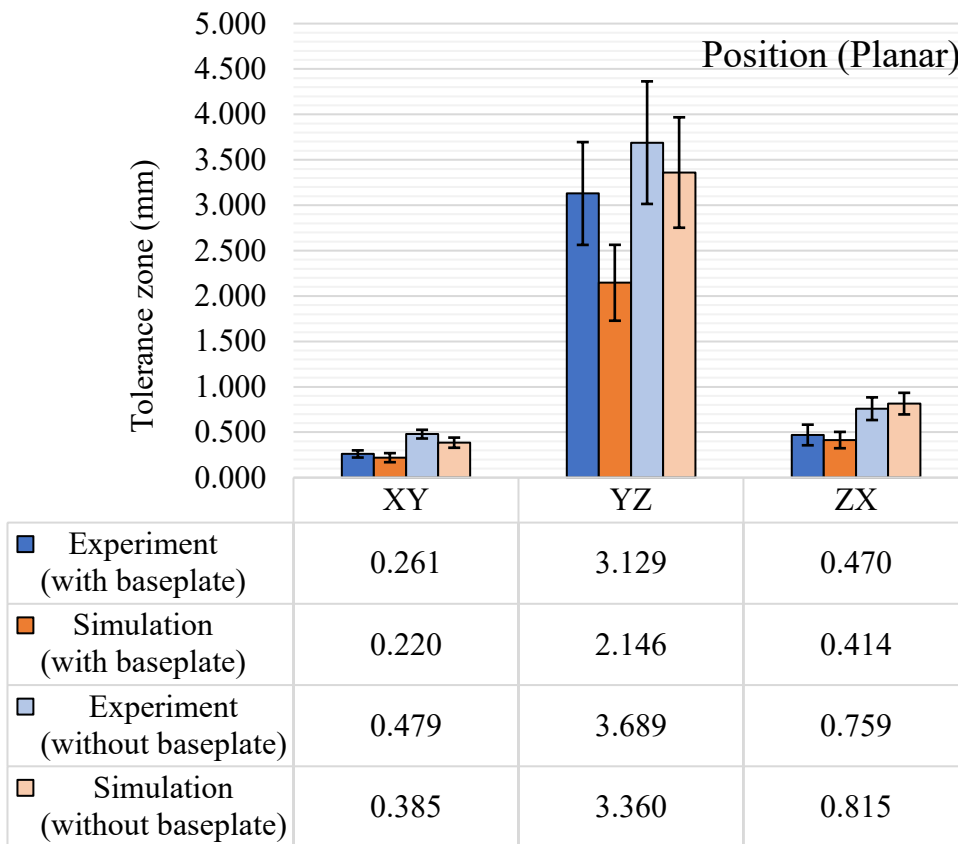


Figure 47. Position tolerance (Planar)

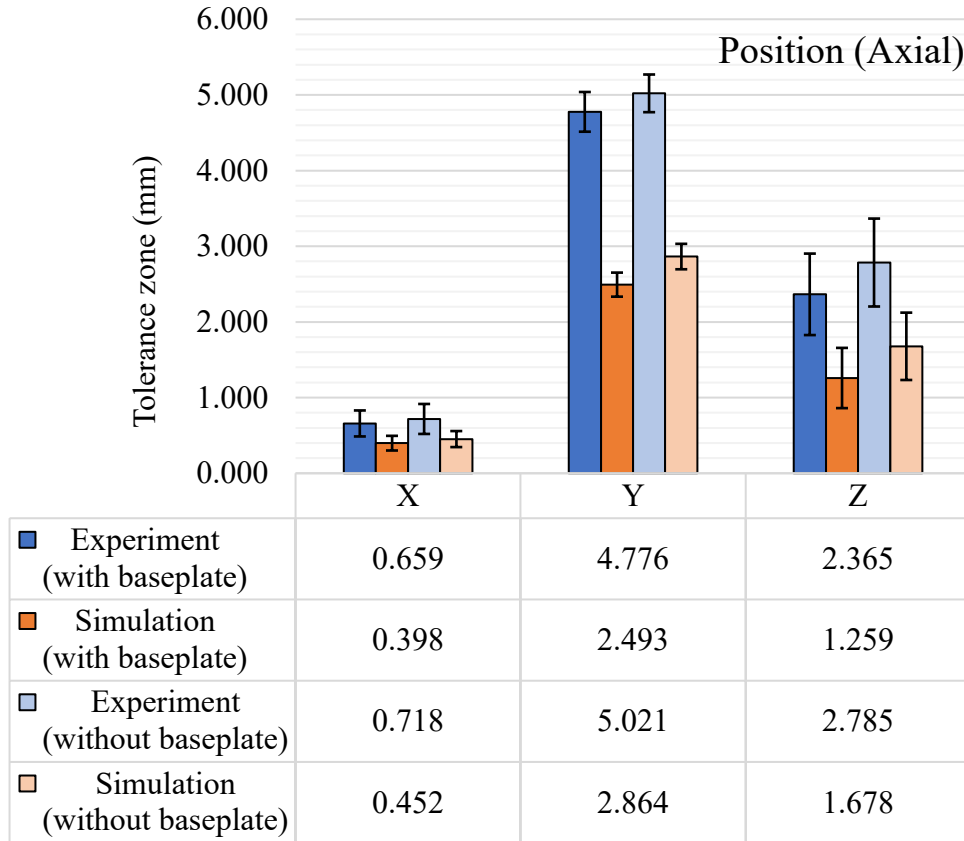


Figure 48. Position tolerance (Axial)

5.4.10. Runout tolerances

Circular runout and total runout tolerance results from both experimental and simulation are shown in

Figure 49 and Figure 50 respectively. Circular runout, in theory, a more precise way of measuring the circularity as it considers all the points on the periphery of the circular feature that is measured.

That is why almost all the circular runout tolerance zones shown in

Figure 49 are 0.050 – 0.100 mm more than the respective circularity tolerance result (Figure 39).

The average tolerance band for experimental circular runout is 0.197 mm with the base plate intact.

After the removal of the base plate, the average value reached 0.217 mm. The standard deviation

also increases from 0.099 mm to 0.109 mm. The maximum runout is observed for Y-axis features,

and the same trend is observed in simulation results. However, the simulation results for circular

runout show a downward mean shift of around 0.010 mm in average tolerance values and the

standard deviation is also reduced by at least 0.030 mm. The average change is mostly due to the

drop in the values in direction of the Y and X-axis. And for experimental results due to the removal of the base plate, surface defects come into play, which is not the case in simulations. This effect is not significant in total runout results as it considers the complete feature, and the effect diminishes as compared to the tolerance zone of the complete feature.

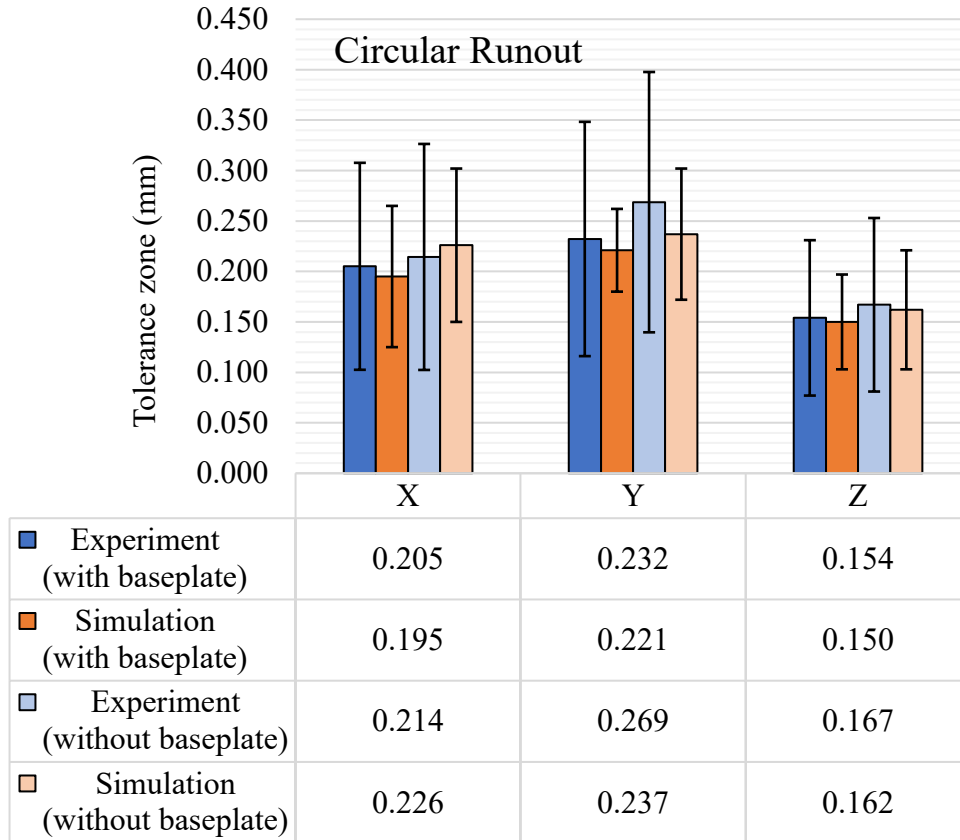


Figure 49. Circular Runout

As shown in Figure 50, the results for total runout are quite higher than the circular runout and even higher than concentricity results except for Y-axis features. For total runout, the experimental and simulation results are quite similar for with and without base plate results, i.e., 0.214 mm and 0.224 mm, respectively. And the standard deviation increases from 0.021 mm to 0.026 mm. Similarly, for simulation results, the average tolerance values increase from 0.214 mm to 0.219 mm and standard deviation values rise from 0.018 mm to 0.025 mm. The trend of difference in total runout tolerance as per axis is similar to the trends observed in circularity and concentricity.

The trend is similar to the trend observed in circular runout and concentricity and the major reasons for this are the support removal and warpage due to residual stresses.

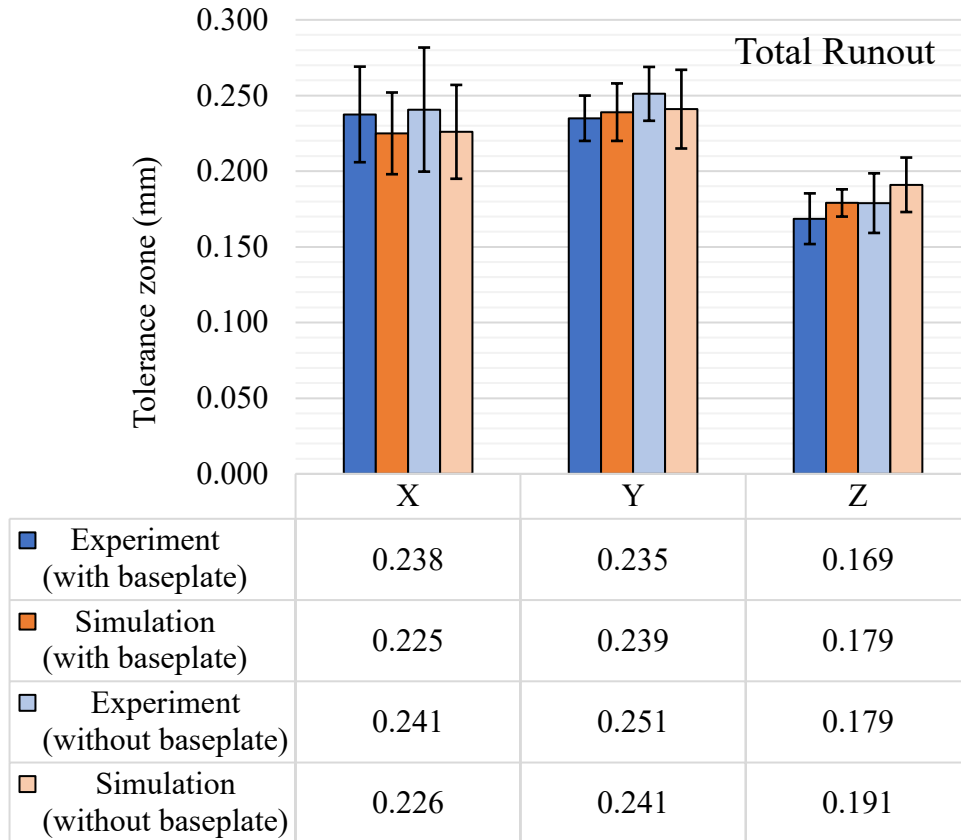


Figure 50. Total Runout

5.5. Conclusions

A new feature-based design of a geometric benchmark test artifact (GBTA) for LPBF is presented which can characterize major geometric tolerance characteristics in three principal planar directions. The GBTA was manufactured using stainless steel (SS 316L) on an LPBF process and subjected to geometric tolerance measurements. The measurements were conducted on the GBTA in two stages: first is with the base plate intact and then after the base plate is removed.

The geometric tolerance zones for features aligned with principal planar and axial directions were presented. The variation in the geometric tolerance zones with the orientation and sizes were discussed. The circularity and cylindricity tolerance zones show a direct proportionality linkage to the diameter of the feature. The orientation of the features leads to a wide range of

variation in geometric tolerance results, the average form tolerance increases after the removal of the base plate. The orientation and position tolerances also show an increase but, in some cases, the combined effect of the stress relief from removal of the base plate and the variation in the tolerance zone of the datum features minimize the overall tolerance variation. The results prove the need for a directionality-based analysis of geometric tolerances and the need to consider the removal of the base plate. The simulation results are used to understand the generic deviation maps with and without the base plate. Further, simulations are utilized to extract GD&T for a quantitative comparison with the experimental GD&T results. It will help to characterize GD&T for complex and large parts without directly moving to experimentation.

The results not only justify the new GBTA design and its features, but also gives a quantitative outlook on the variation of the geometric tolerances as per tri-planar orientation, sizes, and base plate condition. It also shows that minimizing the residual stress and overall deviations do not lead to minimum tolerance zones for various geometric characteristics that dictate the functionality of the part. However, custom features and analysis are required to ascertain if the given tolerance specifications are met. The simulation results are not in 100% agreement with the experimental results. More research is therefore required to make sure that simulations can precisely predict the geometric tolerances for the LPBF process and can consider the uncertainty of the process. It is hypothesized that the geometric tolerances will be affected by the selection of process parameters, a process parameter optimization for specific geometric tolerances is still required.

6. GBTA based GD&T and assembly prediction for LPBF process⁶

The previous chapter gave a detailed account of how to design and characterize a normative GBTA leading to generic GD&T quantification for an LPBF process. However, product-specific geometric tolerance characterization and prediction can still not be addressed with the normative GBTA. So, this chapter will dive into product-specificGBTAs and their applicability to characterize specific GD&T leading to assemblability checks. On top of that, a predictive approach called ‘skin model shapes’ is utilized for the first time for predicting GD&T and assemblability for LPBF processes. The ‘skin model shapes’ is a methodology for generating a large number of geometric samples for analyzing the shape deviations or in this case geometric tolerances. The overall schematic of the research approach is shown in Figure 51.

The methodology starts with the assembly benchmark test artifact (ABTA) design. Then the designed benchmark is subjected to two phases of skin modeling technique. The observation phase skin models are generated using deviated mesh from the results of high-fidelity numerical simulation of the LPBF process. These skin models are then compared with the prediction phase models which are generated using the deterministic and random deviations of the process in consideration. The comparison is then conducted based on the total deviation of the skin model from the nominal shape. The generation variables of the prediction phase samples are then updated to tune these models as per the observation phase samples. The objective of using prediction phase samples is to avoid the long and cumbersome numerical simulation of the LPBF process which sometimes takes days to generate a few samples. On the other hand, prediction phase samples are based on simple mathematical relations and can be generated in huge numbers within a few seconds. These prediction phase samples can be then used for GD&T and assemblability studies. Further, the designed benchmark is manufactured using the LPBF process and geometrically characterized for comparison and validation of the methodology.

⁶ Parts of this chapter have been published in:

- B.S. Rupal, N. Anwer, M. Secanell, A.J. Qureshi, “Geometric Tolerance and Manufacturing Assemblability Estimation of Metal Additive Manufacturing (AM) Processes”, *Materials and Design*, Vol. 194, pp. 1-15, 2020.
- B.S. Rupal, N. Anwer, M. Secanell, A.J. Qureshi, “Geometric Tolerance Characterization of Laser Powder Bed Fusion Processes Based on Skin Model Shapes”, *Procedia CIRP*, Vol. 92, pp. 169-174, 2020.

6.1. Assembly benchmark test artifact (ABTA) design

The first step in the quantification of the assembly behavior of AM components is to quantify the geometric behavior of individual components in the assembly, followed by an assembly tolerance analysis and assemblability study on the mating assembly components. The ABTA design is conducted based on the two-stage GBTA design methodology formulated in chapter 2 and following the guidelines of [ISO/ASTM 52902, 2019]. The first stage in the methodology is the normative design stage in which the GBTA is designed so that it provides a normalized generic geometric GD&T information about the AM process being considered.

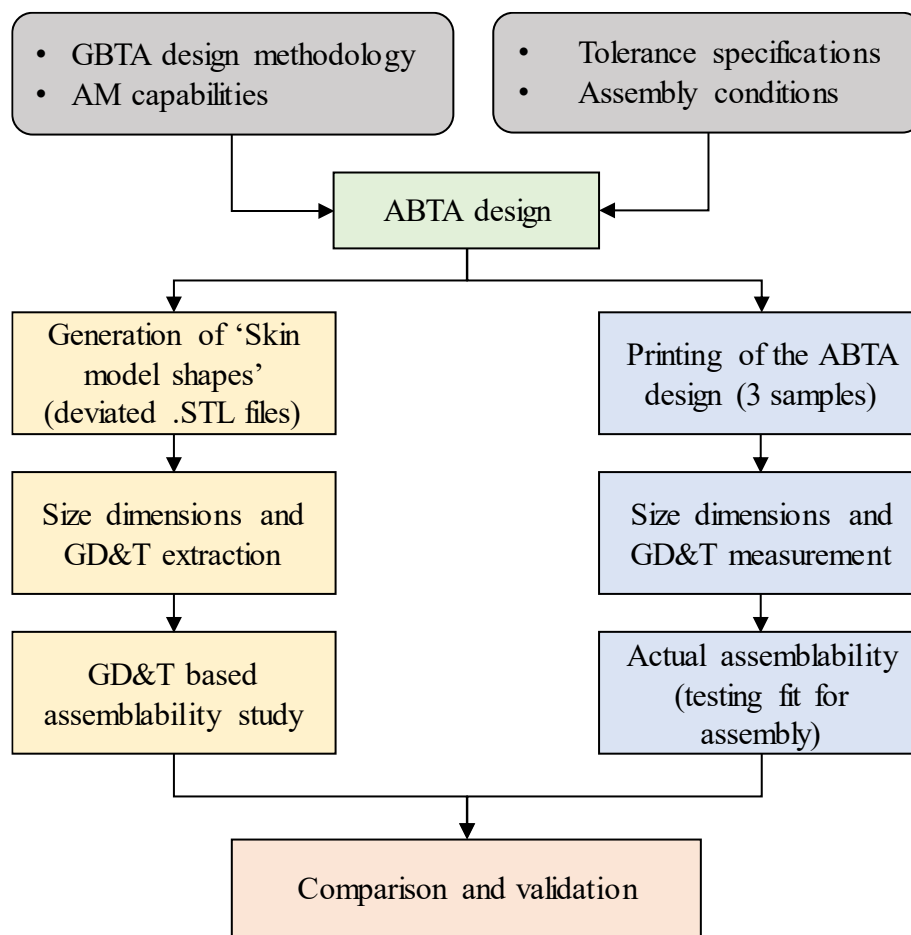


Figure 51. Overall schematic of the research approach for GD&T and assembly prediction for LPBF process

In the second stage, the GBTA design is customized to the requirements of a target product with given geometric and functional specifications. In this case, the second stage design conditions will be used. The aim is to conduct the assemblability study of the AM process under consideration as per GD&T characteristics using common assembly joints. As per the systematic GBTA design methodology developed in chapter 2, the new ABTA design should fulfill the following criteria.

6.2. ABTA design criteria

- 1) ABTA must conform to the manufacturing size constraints (design size and build volume) of the metal AM process under consideration.
- 2) ABTA must enable physical testing of the components considering basic assembly mates in the design, such as revolute, prismatic, and spherical joints, and ‘fit for assembly’ analysis. Some of the common features for ‘fit for assembly’ consideration is described in Table 18, along with suggested geometric features.
- 3)

Table 18. Assembly joints for AM and GBTA features for the same

Assembly joint	GBTA features considered
Revolute Joint (1 DOF)	Detachable links with holes and a pin of mating dimensions (hinge type joint)
Planer Joint (1/2/3 DOF)	Flat and/or cylindrical pin in corresponding slots of 1/2/3 DOF of mating dimensions
Prismatic Joint (1 DOF)	A detachable solid and hollow cuboid of mating dimensions
Threaded Joints (1 DOF)	Relevant threaded screw pair of variable dimensions
Cylindrical Joint (2 DOF)	Detachable pin and hole of mating dimensions
Spherical Joint (3 DOF)	Ball and socket of relevant dimensions
Snap Joints (1 DOF)	Snap and an undercut of basic designs (annular, tapered)
DOF: Degree of freedom	

- 4) ABTA must include features including exclusive metal AM capabilities such as topology-optimized features (unit-cells and organic shapes) as they have a significant effect on the final geometric tolerances.

- 5) Accommodate feature selection based on the process parameters of the AM process, such as minimum layer thickness and metal powder particle size, to decide the minimum feature size and provide accompanying process parameter data.
- 6) Provide functional geometric specifications on the features to quantify tolerance bands in terms of GD&T quantifiers such as cylindricity, flatness, and true position tolerance from corresponding features on the ABTA.
- 7) Enabling quantification of features as per geometric standards [ISO 1101, 2017], [ASME Y14.5, 2019], and AM specific standards [ISO 17296-3, 2014] and [ASME Y14.46,2017].
- 8) Relatable to the actual assembly components build on the metal AM processes to extrapolate the applicability of the GBTA study to real products.
- 9) Must be designed while keeping in mind the ease, accessibility, and capability of measuring the features with precise metrological equipment such as a coordinate measuring machine (CMM) or high precision laser scanner. It will further depend on the minimum feature sizes and the spatial distance between the features on the ABTA. The choice of the measurement equipment should be specified based on the expected tolerance bounds and specifications.
- 10) Must be able to extract systematic and random deviation modes from the metrology of the ABTA, which affect the assembly of the components.
- 11) Imparting static and kinematic assembly ‘fit for function’ testing as per the given geometric requirements.
- 12) The features on the ABTA must consider the interlinkage between design for assembly and design for additive manufacturing. Such as degrees of freedom of the parts/features, placement of parts, and orientation.
- 13) It must avoid support structures on the assembly features to correctly study the effect of the process parameters without the interference of supports on the geometric tolerances.

Based on these design criteria, an ABTA was designed, as shown in Figure 52. In this ABTA, only revolute joint and planer joints are considered as these two are the most common assembly joints in AM assemblies [Sossou et al., 2018]. Two revolute joints are included to reduce the degrees of freedom and to study the positional variation between the two revolute features and their effect on the assemblability.

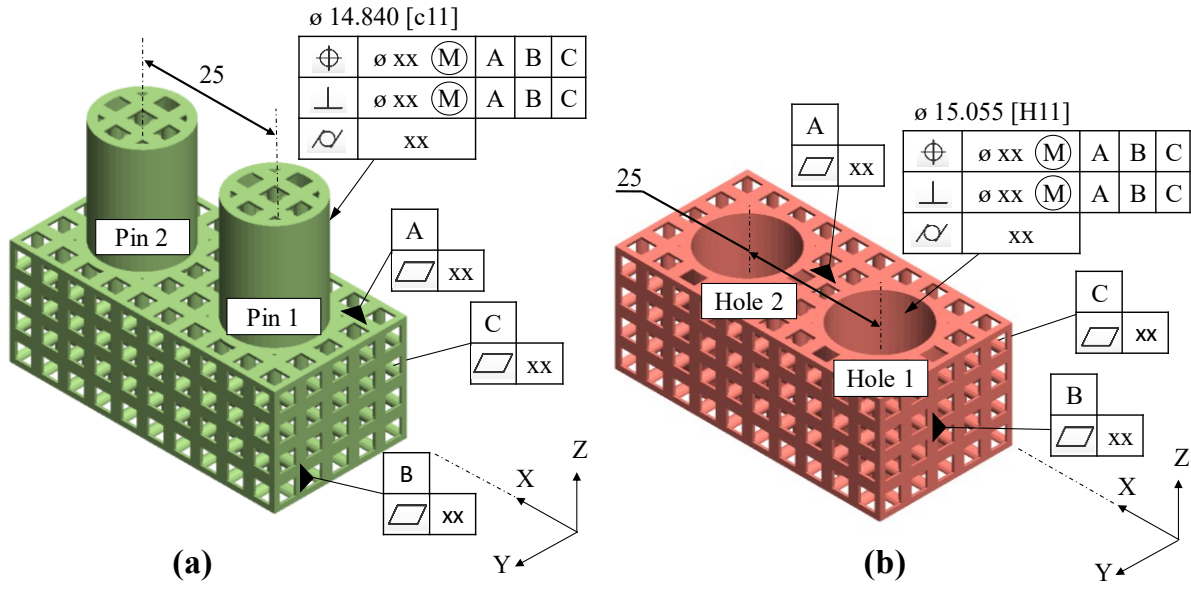


Figure 52. Pin component (a) and hole component (b) of the ABTA along with the functional dimensions and GD&T characteristics. Units: mm.

For the pin component of the ABTA or ‘pin-ABTA’ shown in Figure 52 (a), the functionality-based GD&T characteristics considered are:

- The flatness of the Datum A plane (assembly direction from top face)
- Perpendicularity of the pin axis with Datums A, B, and C
- Cylindricity of the pins
- Position tolerance of the pins with respect to Datums A, B, and C

And for the hole component of the ABTA or ‘hole-ABTA’ shown in Figure 52 (b), the GD&T characteristics considered based on functionality are:

- The flatness of the Datum A plane (assembly direction from top face)
- Perpendicularity of the hole axis with Datums A, B, and C
- Cylindricity of the holes
- Position tolerance of the holes with respect to Datums A, B, and C

The linear overall dimensions of the hole-ABTA are 50 x 25 x 20 mm (L x B x H). For the pin-ABTA same dimensions are used, and the pin height is 20 mm. A generic hole basis clearance fit of H11/c11 was specified to the hole and pin for determining size-based assembly limit and fit for the cylindrical features as shown in Figure 52. However, the LPBF process cannot take

tolerance data into account, and the only input is the STL file. So, the mean tolerance value of the tolerance zone is used to generate a nominal diameter for the STL files. i.e. 14.840 mm for the pin diameters and 15.055 mm for the hole diameters. The GD&T characteristics of the ABTA are also presented in Figure 52. A maximum material condition is used along with the true position tolerance to facilitate assembly. The GD&T specifications for the ABTA for geometric tolerance allocation are decided based on the prediction phase skin model shapes analysis, which is discussed in the next section.

As shown in Figure 52, the mating plane designated as Datum A on the ABTA is a surface containing voids due to lattice structures. Although these add value through topology optimization and weight reduction potential, they add complexity to the part manufacturing process and the expected geometric tolerance. Standard lattice unit cells [Dong et al., 2017] are considered for applying this complexity to the ABTA. The zoomed-in view of the lattice structure on the ABTA and the corresponding unit cell is shown in Figure 53. *ANSYS SpaceClaim Direct Modeler 19.2 Academic* is used to convert the solid ABTA geometry into a lattice structure by using facet shell command and simple cubic lattice infill. The thickness of the shell is 1.5 mm, infill percentage is 37.7%, length of the unit cell is 5 mm, and thickness of the unit cell beam is 1 mm, the dimensions are shown in Figure 53.

The lattices, such as the one used here, which directly become the part of the geometric boundaries and must directly conform to the part specifications, are known as ‘macro lattice structures’ [Ameta et al., 2018]. To conduct measurements and tolerance study of these macro lattice structures, the concept of total supplemental surface (TSS) is used from ASME Y14-46 [ASME Y14.46, 2017]. The flat supplemental surface used in this study and the measurement schematic is shown in Figure 54. For flatness measurements of the lattice surface Gaussian best fit algorithm is used on the measured points using the CMM probe. With more complex lattice structures, organic shapes and minimal surface unit cells (such as Schwartz D), the planar surface area becomes negligible, which makes the measurements difficult. Moreover, suitable algorithms are still not developed, which can lead to reliable results from highly complex geometric surfaces [Ameta et al., 2018]. Therefore, the cylindrical assembly features are not subjected to lattice topology.

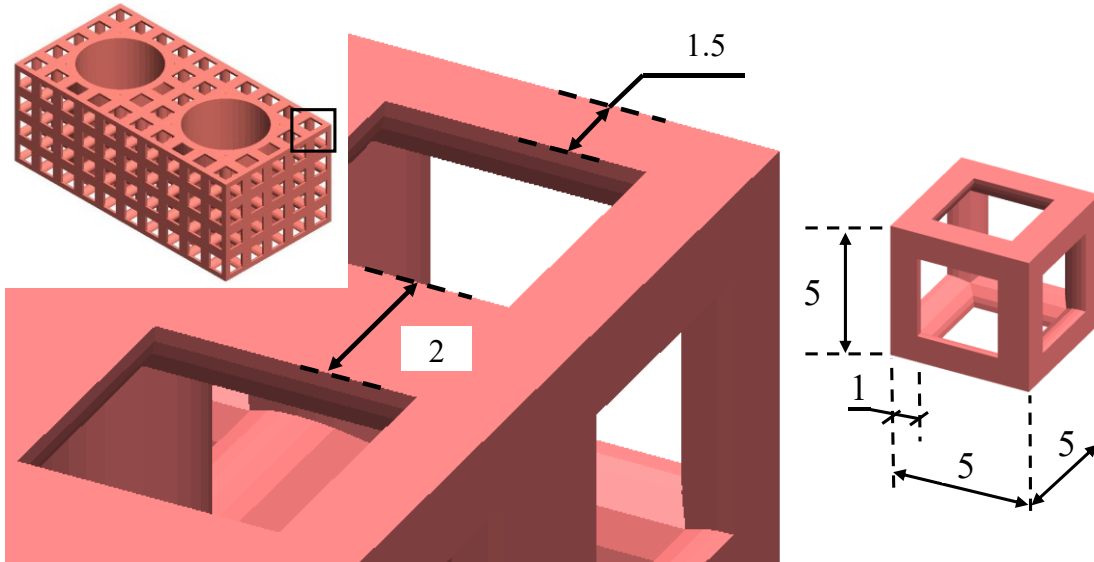


Figure 53. Zoomed-in view of the hole component of the assembly GBTA to show important dimensions. A unit cell of the simple cubic lattice used in the assembly GBTA is also shown on the right. Units: mm.

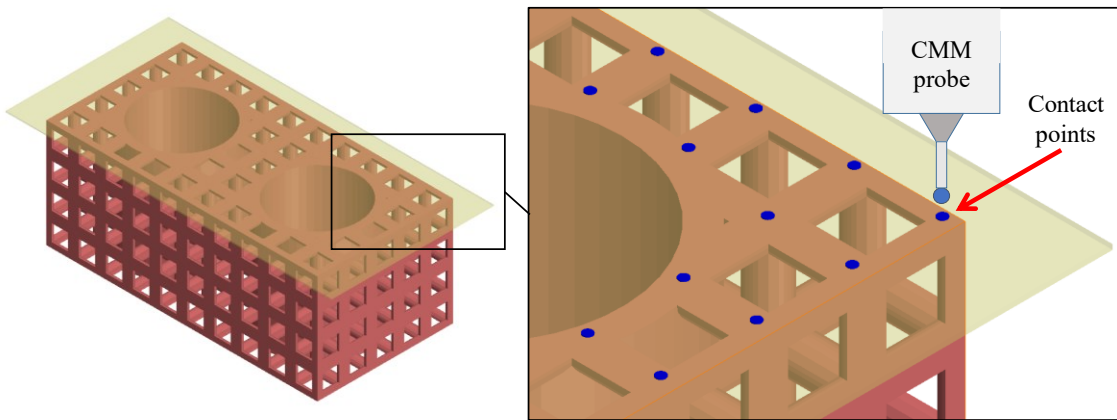


Figure 54. Usage of supplemental surface for topology optimized flat features. Inset shows the contact points on the surface which are recorded by the CMM probe to measure flatness

6.3. Skin model shapes based tolerancing

A skin model is defined as ‘a model of the physical interface between the workpiece and its environment’ [Schleich et al., 2014]. A skin model considers the nominal shape of the part and the geometric deviations from various sources such as simulation data, experimental data, or random deviations modeling different aspects of the process. These deviations are added to the

nominal part geometry represented by a 3D point cloud. Considering the deviations, each point has deviated in the direction of the surface normal vector, and the magnitude of the deviation is dependent on the selected systematic or random deviation parameters. The samples generated from these deviations also called the skin model shapes, are used to conduct the geometric tolerance and assemblability study. The skin model shapes are generated in two stages. First is the prediction stage: In the early design stages, geometric deviations of the part to be manufactured are not yet known. Therefore, the skin model should incorporate assumptions on systematic and random deviations to predict potential deviation modes for given specifications. The second stage is the observation stage: during later design stages, manufacturing process simulations and even prototypes of the part may be available. Thus, a skin model should consider the given observations (mostly simulation results) and simulate possible outcomes of the production process based on a few samples.

As per the design stage of the part, the skin models are generated based on the prediction and observation stage. After the comparison of results from both the phases, the prediction stage skin models are updated to make sure that the design specifications are met, such as maximum/minimum deviation ranges and geometric tolerance bands. In this case, it is done by comparing the maximum, average, and minimum deviation in the ABTA of the observation phase skin model shapes with the prediction phase skin model shapes. MATLAB routines are written to conduct the prediction and observation stage skin model simulation based on the workflow shown in Figure 55. The following paragraphs describe the brief process for generating the prediction and observation phase skin model shapes for the LPBF processes.

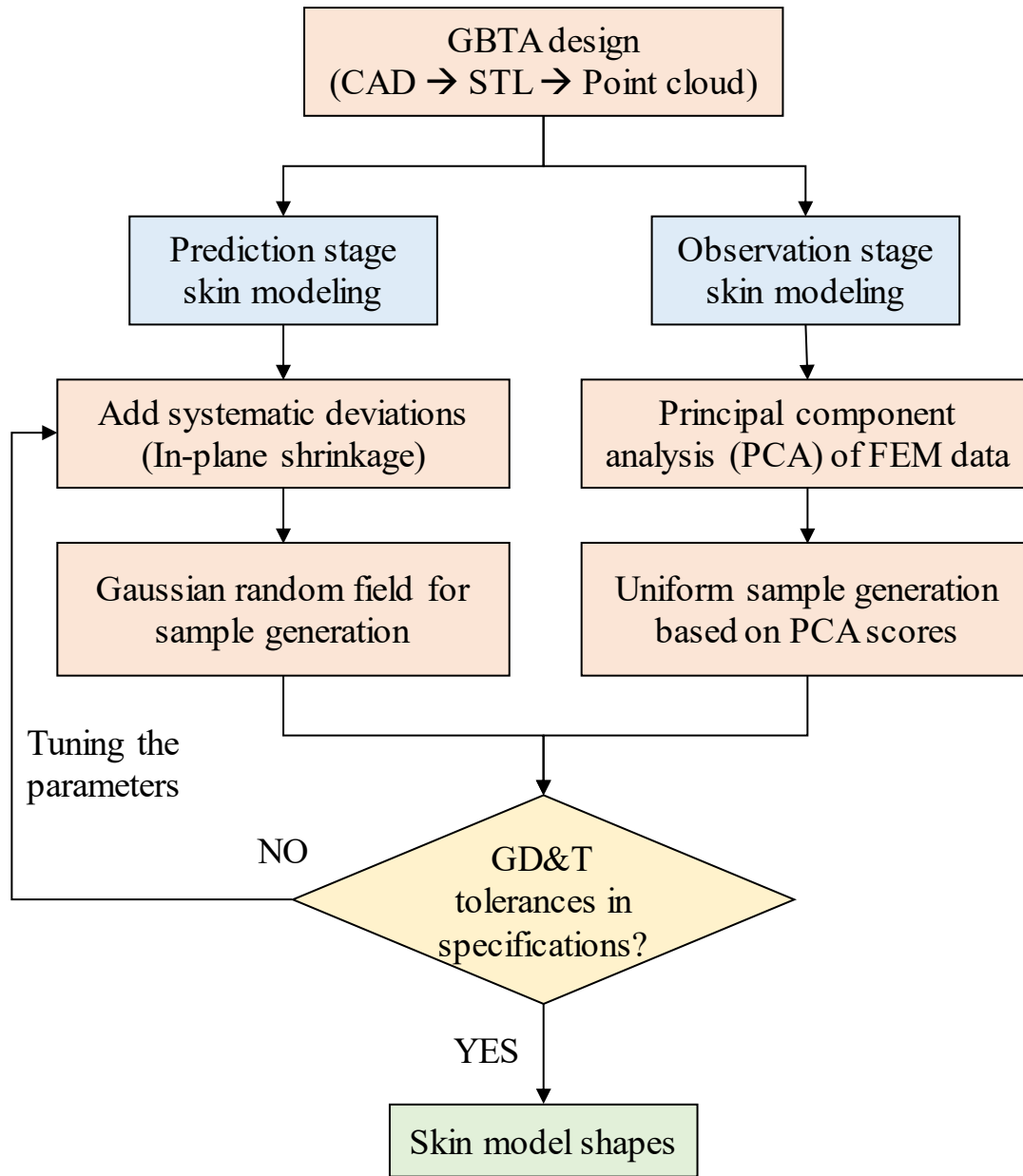


Figure 55. The skin model shapes generation workflow

6.4. Prediction phase sample generation based on in-plane shrinkage

In the prediction stage for LPBF, systematic deviations based on specific shapes are not included as the manufacturing process is relatively new, and there is no detailed literature/data on the systematic deviation modes for metal AM concerning various geometric shapes. Moreover, the systematic deviations vary with changes in the machine architecture and process parameters as well. Therefore, the prediction phase is launched by populating the deviation fields with

quantitative bounds from expert knowledge and previous experience that serves as initial seeding data. The data may be obtained from previous metrology data from other samples tested with similar systems, generic factors, such as shrinkage factors reported from standards or best practices, or simulated data from a given model. In this specific example, a shrinkage factor is applied globally as per the in-plane deviation methodology and then updated as per the observation phase results. The shrinkage factor is added to the nominal point cloud (generated from the input STL file using MATLAB function *stlread*), and the new point cloud is used for further modeling. The mathematical relationship for adding systematic deviations including the shrinkage factor as described above to the nominal point cloud has been described in detail in [Zhu et al., 2018] and are given as:

$$[X_s] = [S_p][X] \quad (6.1)$$

where,

X = A point from the point cloud of the nominal STL, i.e. (x_i, y_i, z_i)

S_p = In-plane shrinkage matrix, $\begin{bmatrix} s & 0 & 0 \\ 0 & s & 0 \\ 0 & 0 & 1 \end{bmatrix}$ where 's' is the in-plane shrinkage factor

X_s = Resultant point with added in-plane shrinkage, i.e. (x_{si}, y_{si}, z_{si})

Following this, random field theory-based random deviations are generated using an assumed correlation function. A squared exponential correlation function is used, which calculates correlation based on the Euclidian distance between adjacent points and an assumed correlation length. The correlation function used is

$$M_{cr} = \exp\left(-\frac{d_{ij}^2}{l_{cr}^2}\right) \quad (6.2)$$

where,

M_{cr} = Correlation matrix

d_{ij} = Euclidian distance between two adjacent points in the point cloud X_s

l_{cr} = Correlation length

Finally, the correlation matrix is calculated, which is combined with a Gaussian random field and the shrunk point cloud (X_s) to generate the final prediction phase samples. The traditional prediction phase skin model shape procedure presented in detail in [Schleich et al., 2014], has been modified for application in metal AM.

6.5. Observation phase sample generation based on thermo-mechanical simulations

Observation stage deviations are based on the simulations of the manufacturing process under consideration for a given geometry. The temperature-dependent material properties of Inconel 718 and the thermal and elasticity governing equations for numerical implementation are based on previously published research [Gouge et al, 2019]. A summary of the governing equations and the formulation is provided in 5.3.1.

6.5.1. Implementation and input parameters

The LPBF process governing equations are solved using *Autodesk Netfabb Ultimate Academic 2019*, which outputs a deformed STL file as an output for further geometric analysis. Table 19 shows the process parameters used for thermo-mechanical simulation. These process parameters have been chosen to reflect the specifications and capability of the experimental system used in the validation phase, as described in the experiments section.

Figure 56 shows the nodal deviation data obtained from the simulation of the Inconel 718 material on the LPBF process. Simulation time for the sample of pin-ABTA is about 5h 25 minutes, and for hole-ABTA is 113 minutes on a single-core CPU. Computation time is one of the significant limitations to generate multiple samples for performing a geometric tolerance study. The nodal deviation data is exported as an STL file for further analysis. For capturing the variability in the process, a total of 20 simulations were run for both pin and hole-ABTAs to generate a training set. The variations were performed by systematically changing the process parameters, i.e., layer thickness (30-70 μm), hatch spacing (100-200 μm), laser power (200-300 W), and scan speed (500-1000 mm/s) [Uddin et al., 2018]. For each deviated sample, the point-to-point Euclidian distance from the nominal geometry is calculated and saved in the form of a matrix.

Following this, a Principal Component Analysis (PCA) was performed on the deviated STLs obtained from the simulations to find the main variation modes and the corresponding PCA scores. Samples are then generated from the PCA scores by performing inverse transform sampling. A normal distribution with a mean equal to zero and unit standard deviation is set into inverse cumulative distribution functions (ICDFs) of the PCA score distributions. Now the resulting deviation point cloud samples are added to the nominal point cloud and used for comparison with prediction phase skin model samples.

Table 19. Simulation parameters of LPBF process

Parameter	Value
Material used	Inconel 718
Laser power	200 W
Heat source absorption efficiency	35%
Laser beam diameter	0.063 mm
Travel speed	1800 mm/s
Layer thickness	0.04 mm
Hatch spacing	0.05 mm
Re-coater time	5 seconds
Interlayer rotation angle	225°
Plate fixture	Fixed at the center of the build plate
Plate size	100 mm x 100 mm x 20 mm
Heat loss coefficient	2.5×10^{-05} (W/mm ² C)
Ambient temperature	25° C
Heat treatment	None
Analysis type	Thermal and mechanical
Meshing style	Layer height based adaptive voxels
Layers per element	20
Maximum mesh adaptive levels	5
mesh coarsening generations	1
Structural plasticity	ON

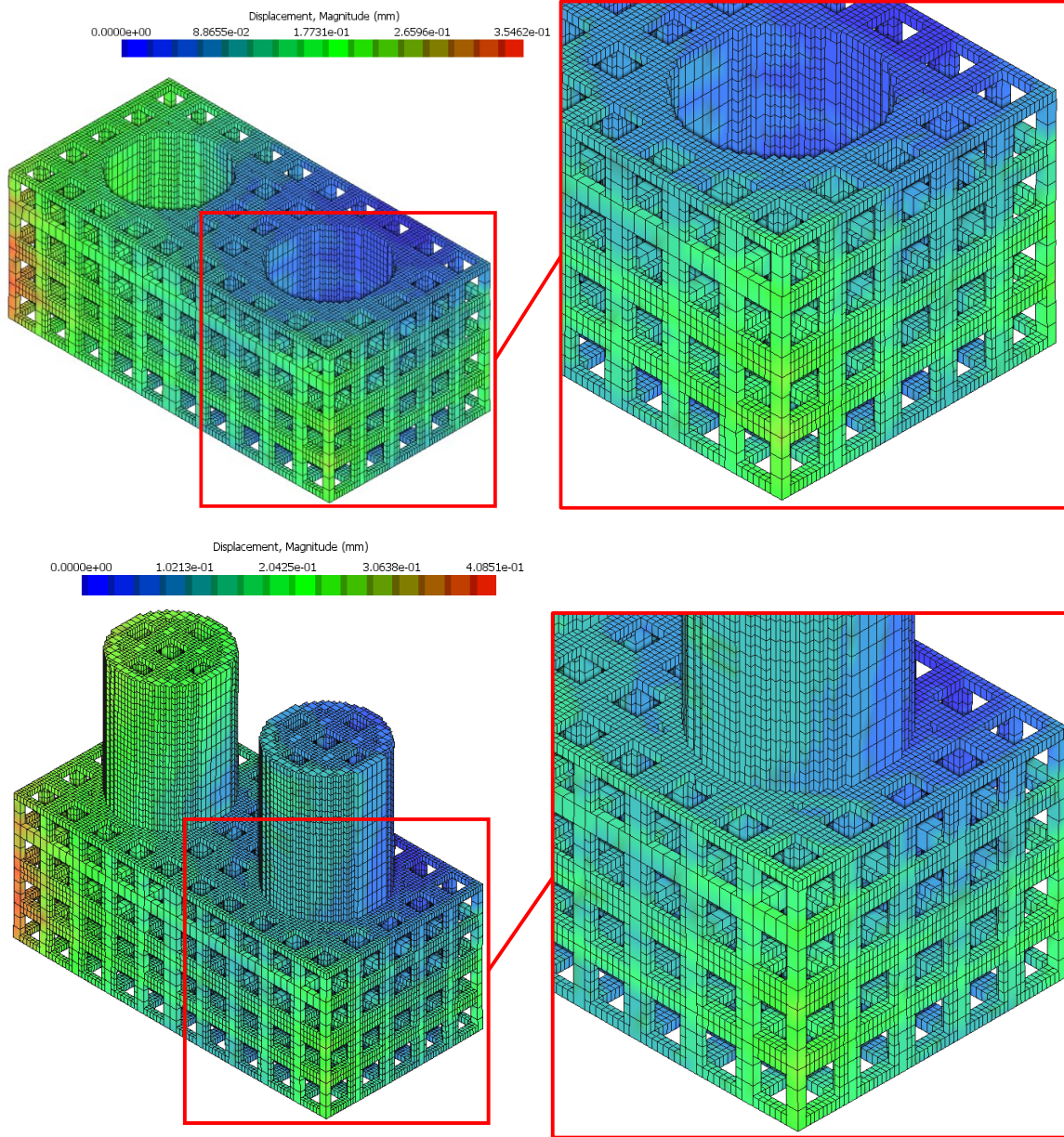


Figure 56. Deformations obtained from the simulation of the LPBF process

6.5.2. Deviation comparison and variable selection

As described in the previous section, the observation phase provides the deviations generated by thermo-mechanical simulations, which are used as input to the prediction phase to update the prediction of the deviations. To do so, first, a matrix of point-to-point Euclidean distances between the input STL and the deviated STL from the simulation is obtained. From this point-to-point analysis, the maximum, average, and minimum deviations are calculated and stored in a deviation

matrix. The same procedure is repeated for all the simulated samples. Now, the variables of the prediction phase modeling are updated until the difference between the maximum, average and minimum deviations of prediction and observation phase are within $\pm 5\%$ at each point. In this case, the shrinkage value was varied from 0.90 to 0.99, and finally, 0.98 was selected. Similarly, for random deviations, a standard deviation of 0.02 mm was chosen with zero mean.

6.5.3. GD&T extraction from deviated STL files

The deviated STLs obtained from observation phase samples and the updated prediction phase samples are now used for GD&T characterization and further geometric analysis. The STLs are converted to point clouds using MATLAB function *stlread*. The point cloud is fed into MATLAB routines, which are programmed as per the GD&T definitions from ISO 1101 [ISO 1101, 2017]. For example, for calculating flatness, the point cloud of the flat feature is first separated from the point cloud of the complete sample. Now, flatness is the distance between two parallel planes containing all points on the given feature. So, the points on the feature are subjected to linear regression to generate the datum plane and then the maximum and minimum distance of the points on the feature is calculated from the new plane, which leads to the flatness tolerance zone. Similarly, other GD&T characteristics are extracted from the model. For a detailed account of GD&T characteristic extraction from 3D point clouds, the readers can refer to Schleich and others [Schleich et al., 2015]. Figure 57 shows GD&T characteristics annotated on one prediction phase sample, against the nominal GD&T characteristics selected for tolerance allocation purposes. Extracting the GD&T from a large number of samples will lead to statistical GD&T based tolerance analysis for AM.

6.6. Experimental Procedure

A laser powder bed fusion (LPBF) system was selected for experimentation of the newly designed ABTA. The LPBF process specifications, as well as the process parameters, are shown in Table 20. Three samples of the ABTA were manufactured on the LPBF process. Each sample was individually manufactured on a separate build plate. After manufacturing, the ABTAs were removed from the base plate using a wire-EDM machine. The manufactured samples on the build plate and removed from the build plate (after assembly) are shown in Figure 58.

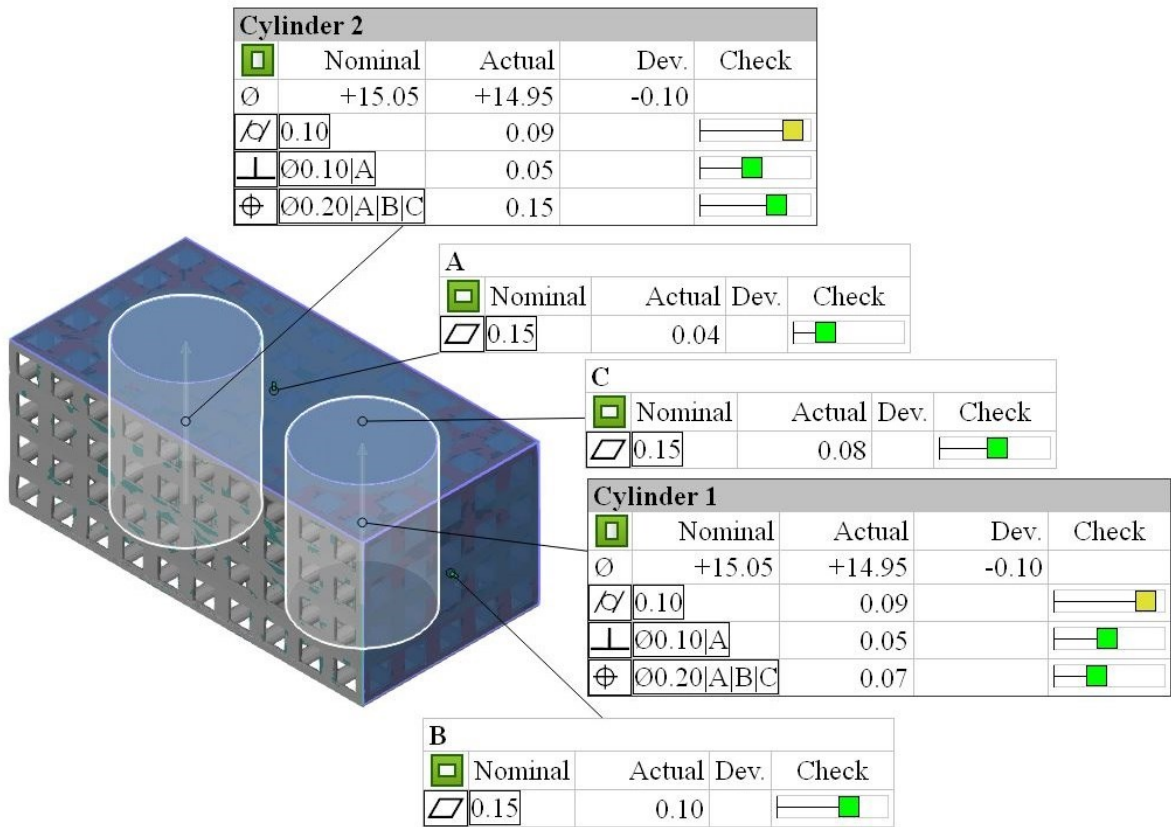


Figure 57. Depiction of various geometric tolerances for the hole component of the ABTA

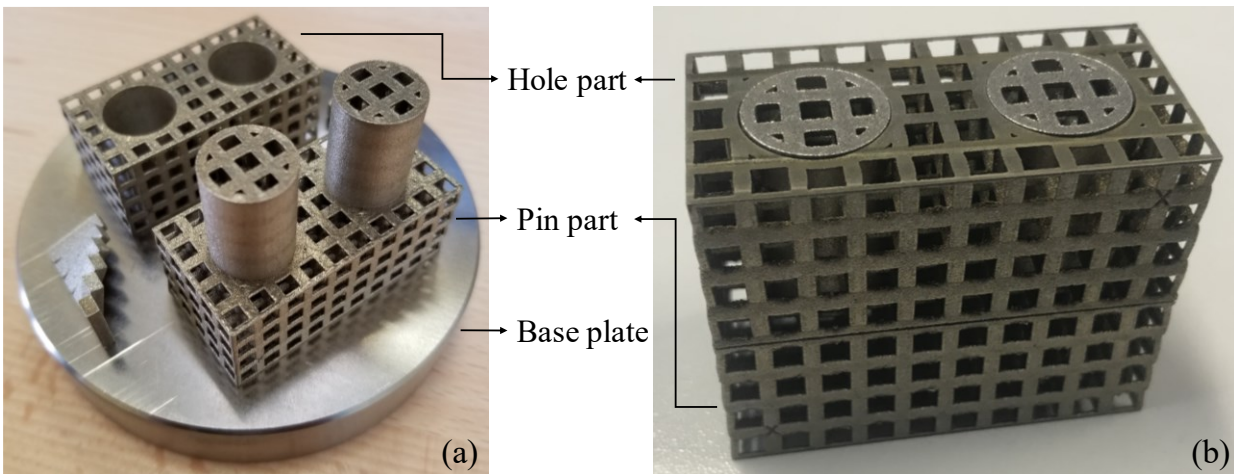


Figure 58. Manufactured ABTA on the build plate (a) and removed from the build plate and (b) assembled as per the specified orientation

Table 20. LPBF process specifications

Parameter/Entity	Value/Description
Machine specifications	
LPBF process used	AddUp FormUp™ 350
Platform size and shape	Circular with diameter 100 mm
Platform thickness	10 mm
Material used	Inconel718
Powder make	Aubert & Duval Pearl Micro Ni718
Powder size distribution	10 – 53 μm
Process parameters	
Layer thickness	40 μm
Part location	Centre of the platform, at $z = 0$ mm
Platform temperature	25° C (Controlled room temperature)
Support structure	No supports
Trajectory reference	Generated by following the build axes
Melting strategy parameters	
First offset (skin operator)	50 μm
Second offset (core operator)	40 μm
Scan mode	Two way
Hatching parameters	
Laser power	210 W
Vector spacing	50 μm
First layer	45° to the horizontal axis
Alternate layer	- 45° to the horizontal axis
Contour parameters	
Orientation	Clockwise
Direction	Out to in
Laser power	190 W
Contour spacing	60 μm
Number of contours	2

After the parts are manufactured, the pin-ABTA and hole-ABTA were measured for size dimensions and geometric tolerances using a CMM. The parts were fixed on the CMM, and a touch probe was used for measurement purposes. A SEIV Renault CMM was used (Guyancourt, France) with a scanner consisting of two sensors: a Kreon Aquilon KA50 laser sensor and a Renishaw TP2 touch probe. The uni-directional measurement repeatability (2σ) of the touch probe is $0.35\ \mu\text{m}$ and the resolution of the CMM is $0.2\ \mu\text{m}$. The measurements were conducted three times for each quantifier to minimize measurement variations and to calculate standard error as well. A minimum of 15 points are taken on the flat surface and flatness was calculated. For cylindrical features, a minimum of 10 points are taken for calculating cylindricity tolerance. Diametric values were deduced using the point cloud data-set recorded for cylindricity calculation. It is to be noted that surface roughness measurements were not considered in this study as the surface roughness for LPBF manufactured Inconel 718 is significantly lower than the form and orientation deviations analyzed in this study. The average surface roughness range is $0.0165\ \text{mm}$ [Whip et al., 2019] and the average tolerance range found in this study is around $0.100\ \text{mm}$ with minimum tolerance around $0.04\ \text{mm}$. Moreover, waviness which is a superimposition of surface roughness [ASME B46.1, 2009] is already included when the parts are measured for form tolerances using a CMM.

After CMM measurements, the ABTAs were tested for fit for assembly with a 100% clearance fit achieved on all three manufactured parts. It was done without any post-processing operation on the manufactured parts. The results from the CMM measurements, the relevance of the skin model shape samples with the geometric tolerance estimation, and assemblability are discussed in the next section.

6.7. Results and discussions

Skin model shape and experimental results are considered for a comparative analysis for validation. After the generation of the observation phase and updating the deviation parameters in the prediction phase, a total of 1,000,000 skin model shapes were generated for each phase for both the pin and the hole ABTA components. The samples were then processed in MATLAB for extracting the dimensional and geometric tolerances as per the GD&T. A comparison of the functional size dimensions (diameter values) is conducted and is shown in Figure 59. The nominal values of both the hole and the pin diameter are $15.055\ \text{mm}$ and $14.840\ \text{mm}$, respectively and are

shown with a red line on the results plot. Both of these values were overestimated with respect to the experimental measurements on the manufactured samples. In the case of the pin component, the observation results are on average 0.090 mm higher than the prediction phase results, whereas in the case of hole components, the average overestimation was of 0.110mm. This corresponds to an error in the size prediction of the size features of 0.75% for the holes and 0.62% for the pin. In addition, in both cases, the prediction results conform to the given assemblability specifications.

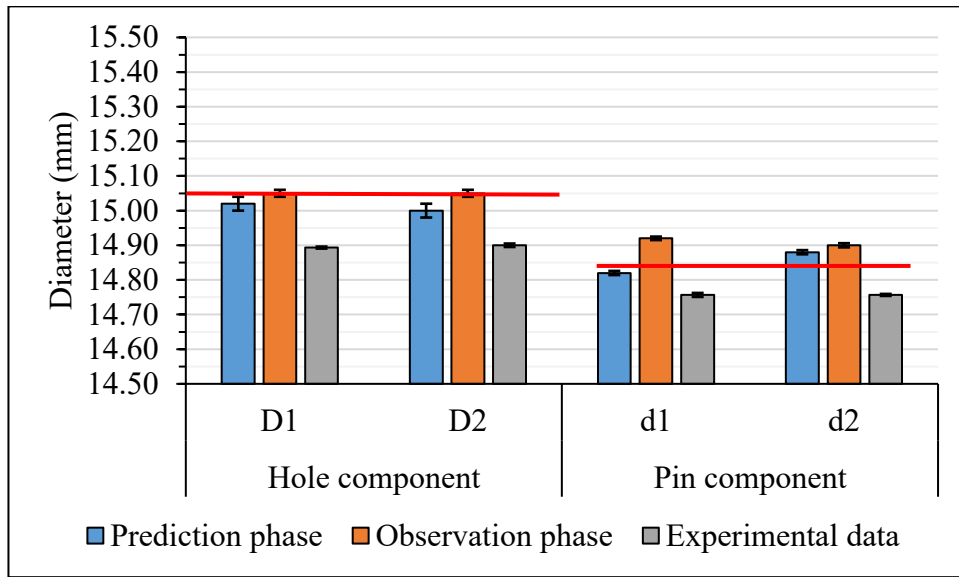


Figure 59. Comparison of diameter values from skin model shapes and experimental data for hole component and pin component, where the horizontal red lines indicate nominal dimensions.

Cylindricity results are shown in Figure 60. The average cylindricity from the prediction phase is 0.056 mm; the cylindricity calculated from the observation phase is 0.070 mm, and from the experimental results, it is 0.054 mm. Overall, the prediction phase tolerance is within a bound of 0.010 mm of the experimental values. Also, the average of the standard deviations of the prediction phase samples, i.e. 0.014 mm, is quite similar to the experimental results, which is 0.008 mm.

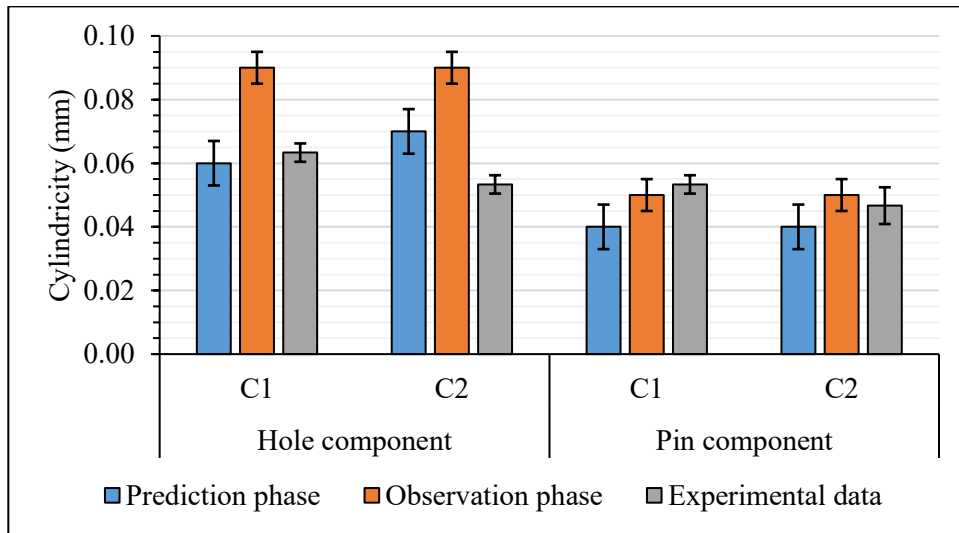


Figure 60. Comparison of cylindricity tolerance from skin model shapes and experimental data for hole component and pin component

Flatness results are shown in Figure 61. Overall, the average flatness is 0.120 mm in both the prediction phase and experimental results; however, it is 0.110 in observation phase results. The average of the standard deviations in experimental and observation phase results is 0.016 and is 0.019 in prediction phase results. The flatness results for the hole component are underpredicted by both the prediction and observation phase samples, especially in the XY plane (on datum A). The reason for this could be the use of lattice unit cells instead of a flat uninterrupted geometry. It has been found from LPBF experiments that lattice cells and cavities lead to more deviations as compared to a flat feature. However, this effect is not precisely captured by the LPBF simulations, especially in the hole component.

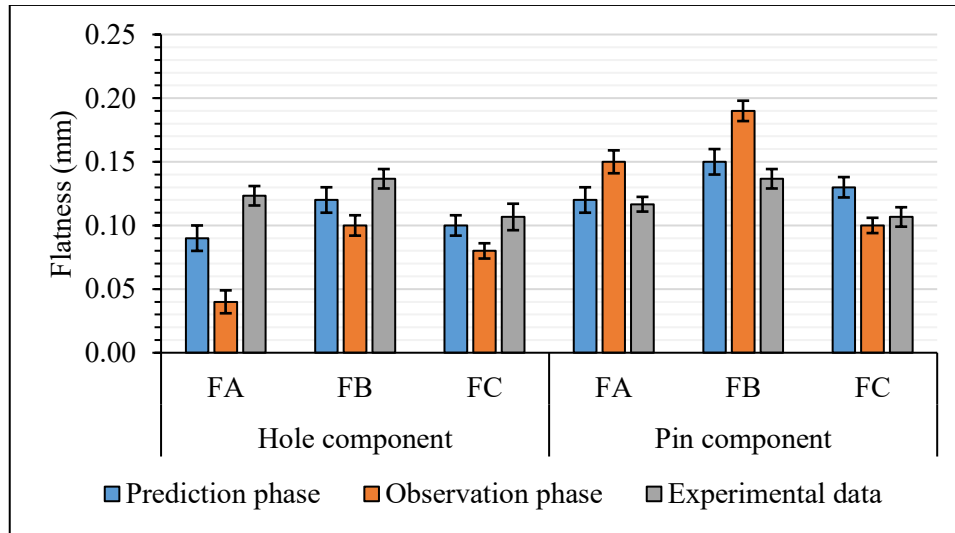


Figure 61. Comparison of flatness tolerance from skin model shapes and experimental data for hole component and pin component

Perpendicularity results for both prediction and observation phases are shown in Figure 62. The average perpendicularity for the prediction phase is 0.043 mm; for the observation phase, it is 0.045 mm, and for experimental results, it is 0.037 mm. The prediction and observation phase perpendicularity is also within a range of 0.020 mm from each other and experimental results except for one outlier, P2, the pin component.

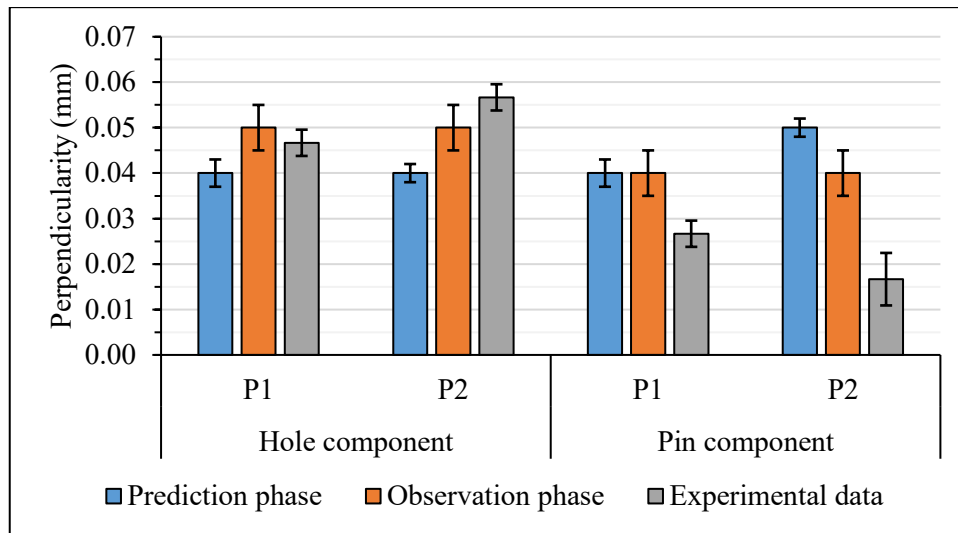


Figure 62. Comparison of perpendicularity tolerance from skin model shapes and experimental data for hole component and pin component

True position tolerance results are shown in Figure 63. The axial position of the cylindrical hole 1 and 2 is observed in this tolerance. For the cylindrical hole 1, the experimental results are within 0.050 mm of the observation phase results; and within 0.020 mm of the prediction phase. For the cylindrical hole 2, the average observation and experimental results are the same, but the prediction phase true position tolerance is 0.030 mm tighter. The trend of the pin component is quite different from the hole component. The experimental true position tolerance for both pins 1 and 2 is at least 0.250 mm higher than both observation and prediction phase results. It is because the true position is a composite tolerance, and it depends on the flatness of the datum planes and the axial position of the cylindrical features, and hence the cumulative effect leads to a larger tolerance zone. So, in this case, the true position tolerance results are dependent on the flatness tolerance of the plane and the perpendicularity tolerance of the cylindrical features. With regards to the specifications, the results are acceptable and conform to the assemblability condition.

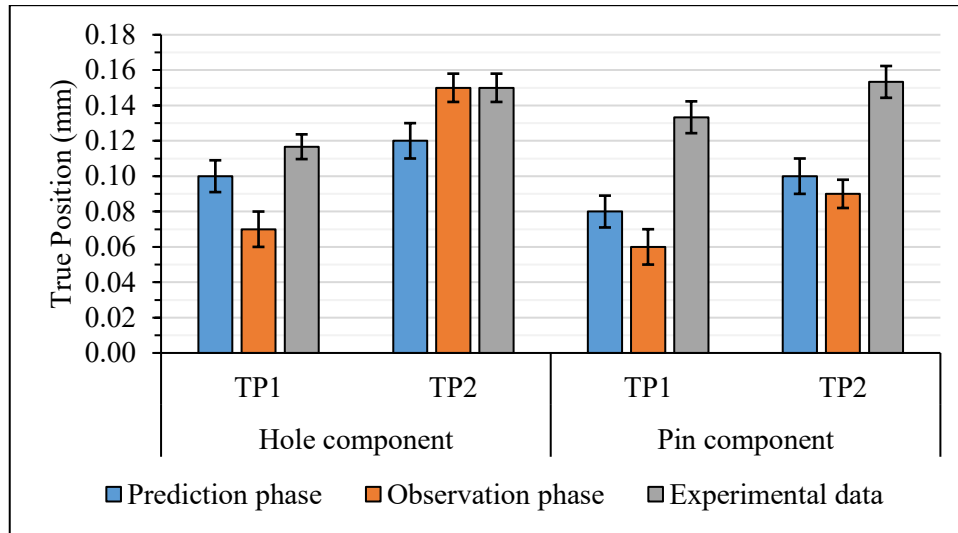


Figure 63. Comparison of true position tolerance from skin model shapes and experimental data for hole component and pin component

Overall, the results show a slight variation between the prediction and observation phase predictions. Even though this number should be identical, small differences exist due to the training criteria allowing for a 5% deviation and the limited number of thermo-mechanical deviation datasets. The diameter values and the GD&T characteristics of the prediction phase skin model shapes are in close agreement with the observation phase results and especially with the experimental results with a standard deviation of ± 0.010 mm. It validates the notion that the assemblability can be estimated based on the geometric tolerances before manufacturing the part. Moreover, most of the quantifiers are overpredicted by the prediction phase results but are within the given specifications and assemblability conditions. It is also reconfirmed with the actual assembly of the all three manufactured hole-pin pairs (one of the actual assembled components shown in Figure 58). The outliers in the prediction phase are due to the use of a uniform in-plane shrinkage factor instead of a shape-based and layer-based systematic deviation. It is to be noted as well that the observation phase results are based on FEM simulations, which already have at least a 10% error with respect to the experimental results. Also, another limitation in the prediction phase results is due to the trial and error-based updating of the prediction phase variables based on the deviations of the observation phase data.

6.8. Conclusions

Geometric functionality and assemblability of the metal AM parts depend largely on the form and position tolerances along with the dimensional deviations. The work presented in this chapter performs a virtual geometric tolerance and assemblability study based on assembly benchmark test artifact and skin model shapes. The geometry selection for the assembly benchmark is based on the feature-based benchmark design methodology in which the features are selected as per the geometric quantifier needed. A two-pin and two-hole component pair is selected as a case study in which geometric tolerances are specified to ensure assembly. For observation phase skin shapes, thermo-mechanical finite element simulations of the LPBF process are performed, and for systematic deviations in the prediction phase, the material shrinkage is used. Prediction phase variables are updated as per the observation phase results, and then samples are generated. These samples are then used to extract geometric tolerances such as flatness, cylindricity, perpendicularity and true position. The method is validated by comparison with the experimental results. Close agreement with the experimental results and the actual assemblability of the manufactured samples confirm the applicability of the method and further use in other metal AM processes.

The proposed methodology can be applied to a variety of process parameters and materials by training the model, using thermo-mechanical simulations, to capture the deviation information from new data and provide geometric tolerance and assemblability information. However, using a better systematic deviation model could improve the prediction phase results as compared to the experimental results. The fitting could also be improved by using automated optimization methods for variable updating. Machine learning models can be explored to automate the process of generating samples from either simulation or experimental data with parametric variations. Authors have analyzed assemblability based on the geometric tolerances only; however, surface-based methods should also be studied. Further, this work lays a direction in which the metal AM community needs to research more for developing new methods and improving existing methods to conduct a virtual geometric tolerance and assemblability study. Geometrically optimized metal AM will not only reduce material wastage but will increase its application in precision manufacturing areas as well.

7. Conclusions and Future Scope

7.1. Conclusions

Additive manufacturing (AM) technology is a leading component in the fourth industrial revolution or Industry 4.0. If the major bottlenecks limiting the use of AM in precision applications can be handled, it will be able to compete with the products manufactured via conventional manufacturing. This thesis is a step towards eliminating one such bottleneck of accurate geometric tolerance quantification and prediction. The thesis with its different research objectives leads to an overall geometric tolerancing quantification and prediction framework for additive manufacturing processes. This framework will assist the additive manufacturing engineers in developing tools for geometric tolerance quantification and prediction. Based on the research gaps and the objectives outlined in chapter one, the summary of the conclusions segregated based on the research objectives is presented below:

1. The second chapter provides a systematic methodology for the design and selection ofGBTAs. Selection is based on the GBTA purpose definition, e.g., AM process characterization, GBTA for specific application part or with parameters optimized for other output properties. The design is based on the guidelines of feature technology, by selecting and assigning features for specific geometric evaluation metrics. Features for all the GD&T characteristics and the fit for assembly requirements based on commonly used mechanical joints are presented. Other geometric properties like dimensional accuracy, minimum feature size, repeatability, surface finish is also considered. The design approach is divided into two stages leading to a normative GBTA design for generic geometric tolerance characterization of the AM process and a product-specific GBTA design for precise GD&T control. A case study is presented leading to the validation of the approach.
2. In the third and fourth chapter, the new GBTA design methodology is implemented on the FFF process for two specific case studies:
 - a. Assembly GBTA for GD&T and assemblability investigation of FFF parts based on process parametric changes. GD&T and IT grades results presented leading to assemblability information. The results show that the material type and part size have a significant effect on the GB&T and assemblability.
 - b. Implementation of a ‘reverse CAD’ algorithm to extract the accurate geometric shape of the FFF parts before printing. The resultant solid model provides a realistic replica

of the FFF part to be printed leading to an accurate geometric and mechanical analysis of the part to be printed. The reverse CAD model is compared with the nominal CAD in terms of geometric metrics and mass leading to validation.

3. The fifth chapter emphasizes the need for geometric tolerance characterization for metal AM processes because the inherent residual stresses during the build process lead to large variations in geometric tolerances. A new feature-based design of a geometric benchmark test artifact (GBTA) for LPBF is presented that can characterize major geometric tolerance characteristics in three principal planar directions. The GBTA was manufactured using stainless steel (SS 316L) on an LPBF process and subjected to geometric tolerance measurements. The measurements were conducted on the GBTA in two stages: first with the base plate intact, and then, after the base plate is removed. The experimental results are then compared with the GD&T results extracted from thermo-mechanical numerical simulations of the LPBF process with the same process parameters. The comparative analysis of the results before and after the removal of the base plate validates the need for tri-planar GD&T characterization in place of the generic deviation map study. Further, the simulation results give a fair estimation of the range and variation in the GD&T characteristics.
4. The sixth chapter aims at developing a product-specific GBTA design that is implemented for the quantification and prediction of GD&T and assemblability for the LPBF process. A two-phase ‘skin model shapes’ methodology is used. To train the model, thermo-mechanical numerical simulations are used in the first phase. The deviation results are compared with the prediction phase skin models, and the parameters are tuned accordingly so that prediction phase samples can be generated. These predictive geometries or skin models are then used to conduct a geometric tolerance analysis on the functional GD&T characteristics. A case study is performed in which an assembly-based GBTA is designed and is then subjected to a skin model shapes predictive tool. The modeling results are compared with experimental GD&T results. Experiments were conducted on an industry-scale LPBF process using Inconel718 metal powder. The comparative results not only validate the methodology but prove the usefulness of the methodology for GD&T-based assemblability prediction.

To sum up, this thesis provides a systematic framework for GD&T based geometric tolerance quantification and prediction for AM processes leading to reliable assemblability information.

7.2. Future research

Based on the limitations of the research work presented in this thesis, the future scope of this study is outlined in the discussion below. In chapter two, the GBTA design methodology is mostly focused on the GD&T and does not include procedures and guidelines for incorporating organic shapes, thin walls, large overhang features. Considering these shapes can be helpful for geometries which are more organic in nature and does not contain mating features or GD&T specific features. Along with this, guidelines need to be added for designing GBTAs for large parts so that costly experimentation can be avoided. Further research is required to incorporate guidelines into the GBTA design methodology for other AM processes whose machine architecture is different such as binder-jet AM or plasma transfer arc AM.

The parametric study presented in chapter three can be extended to various other geometries and process parametric variations to make sure that different assembly conditions are considered for FFF based assemblability investigation. Further research work can also be conducted to include other machine variables such as, extruder nozzle diameter, and slide type for the cartesian movement of the bed.

The reverse CAD algorithm presented in chapter four is only validated using mass comparison and overall geometric deviation analysis. A complete GD&T analysis still needs to be conducted on the reverse CAD models so that it can be further used for geometric conformance investigation purposes such as for GD&T prediction and parametric selection.

For the GBTA study in chapter five, improved simulation tools can be used to make sure that the GD&T quantification can be reliably achieved even without experimentation. As observed in some results, the simulation was not able to capture the anisotropy observed in experiments. This is hypothesized to be due to the movement of the recoater, which is not included in the simulation. Therefore, future investigations should incorporate the movement and direction of recoater in the simulation and other experimental conditions such as the direction of argon gas flow.

In chapter six, the parametric tuning for the variable selection of the skin model shapes is manual as of now, the method will improve if an optimization algorithm is used for parametric tuning of the prediction phase skin model shapes. Also, sensitivity analysis can be conducted on input variables and process parameters such as, on the heat absorption efficiency, and material properties of the powder, to improve the simulation results.

References

Aboutaleb, A. M., Bian, L., Rao, P. K., & Tschopp, M. A. (2017). Accelerated Geometry Accuracy Optimization of Additive Manufacturing Parts. In ASME 2017 12th International Manufacturing Science and Engineering Conference collocated with the JSME/ASME 2017 6th International Conference on Materials and Processing. American Society of Mechanical Engineers Digital Collection.

Ahn, S. H., Montero, M., Odell, D., Roundy, S., & Wright, P. K. (2002). Anisotropic material properties of fused deposition modeling ABS. *Rapid prototyping journal*.

Ameta, G., Fox, J., & Witherell, P. (2018). Tolerancing and verification of additive manufactured lattice with supplemental surfaces. *Procedia Cirp*, 75, 69-74.

Ameta, G., Lipman, R., Moylan, S., & Witherell, P. (2015). Investigating the role of geometric dimensioning and tolerancing in additive manufacturing. *Journal of Mechanical Design*, 137(11).

Ameta, G., Moylan, S. P., Witherell, P. W., & Lipman, R. (2015). Challenges in tolerance transfer for additive manufacturing. In *Summer Topical Meeting of American Society of Precision Engineering* (pp. 8-10).

ASME B46.1:2009, Surface texture: surface roughness, waviness and lay.

ASME Y14.46: 2017, Product definition for additive manufacturing.

ASME Y14.5: 2018, Dimensioning and Tolerancing - Engineering Drawing and Related Documentation Practices.

Barari, A., Kishawy, H. A., Kaji, F., & Elbestawi, M. A. (2017). On the surface quality of additive manufactured parts. *The International Journal of Advanced Manufacturing Technology*, 89(5-8), 1969-1974.

Barros, R., Silva, F. J., Gouveia, R. M., Saboori, A., Marchese, G., Biamino, S., ... & Atzeni, E. (2019). Laser powder bed fusion of Inconel 718: Residual stress analysis before and after heat treatment. *Metals*, 9(12), 1290.

BS 7172: Guide to assessment of position, size and departure from nominal form of geometric features

Byun, H. S., & Lee, K. H. (2003, May). Design of a new test part for benchmarking the accuracy and surface finish of rapid prototyping processes. In *International Conference on Computational Science and Its Applications* (pp. 731-740). Springer, Berlin, Heidelberg.

Calignano, F., Lorusso, M., Pakkanen, J., Trevisan, F., Ambrosio, E. P., Manfredi, D., & Fino, P. (2017). Investigation of accuracy and dimensional limits of part produced in aluminum alloy by selective laser melting. *The International Journal of Advanced Manufacturing Technology*, 88(1-4), 451-458.

Carter, W. T., Erno, D. J., Abbott, D. H., Bruck, C. E., Wilson, G. H., Wolfe, J. B., ... & Stevens, R. G. (2014). The GE aircraft engine bracket challenge: an experiment in crowdsourcing for mechanical design concepts. In *25th Annual International Solid Freeform Fabrication Symposium*, Austin, TX, Aug (pp. 4-6).

Chang, S., Li, H., Ostrout, N., & Jhuria, M. (2015). Geometric Element Test Targets for Visual Inference of a Printer's Dimension Limitations.

Cheng, B., Shrestha, S., & Chou, K. (2016). Stress and deformation evaluations of scanning strategy effect in selective laser melting. *Additive Manufacturing*, 12, 240-251.

Cogorno, G. R. (2006). *Geometric dimensioning and tolerancing for mechanical design* (p. 272). McGraw-Hill.

Colosimo, B. M., Huang, Q., Dasgupta, T., & Tsung, F. (2018). Opportunities and challenges of quality engineering for additive manufacturing. *Journal of Quality Technology*, 50(3), 233-252.

Cooke, A. L., & Soons, J. A. (2010, August). Variability in the geometric accuracy of additively manufactured test parts. In *Proceedings of 21st Annual International Solid Freeform Fabrication Symposium*, Austin, TX (pp. 1-12).

Dantan, J. Y., Huang, Z., Goka, E., Homri, L., Etienne, A., Bonnet, N., & Rivette, M. (2017). Geometrical variations management for additive manufactured product. *CIRP Annals*, 66(1), 161-164.

Dong, G., Tang, Y., & Zhao, Y. F. (2017). A survey of modeling of lattice structures fabricated by additive manufacturing. *Journal of Mechanical Design*, 139(10).

Equbal, A., Sood, A. K., Ansari, A. K., & Equbal, A. (2017). Optimization of process parameters of FDM part for minimizing its dimensional inaccuracy. *International Journal of Mechanical and Production Engineering Research and Development*, 7(2), 57-65.

Fahad, M., & Hopkinson, N. (2017). Evaluation and comparison of geometrical accuracy of parts produced by sintering-based additive manufacturing processes. *The International Journal of Advanced Manufacturing Technology*, 88(9-12), 3389-3394.

Gao, W., Zhang, Y., Ramanujan, D., Ramani, K., Chen, Y., Williams, C. B., ... & Zavattieri, P. D. (2015). The status, challenges, and future of additive manufacturing in engineering. *Computer-Aided Design*, 69, 65-89.

Garcia, E., Ayranci, C., & Qureshi, A. J. (2017, August). Digital light processing (dlp): Anisotropic tensile considerations. In *Proceedings of the 28th Annual International Solid Freeform Fabrication Symposium*, Austin TX, USA (pp. 7-9).

Gibson, I., Rosen, D., Stucker, B., & Khorasani, M. (2014). *Additive manufacturing technologies* (Vol. 17, p. 195). New York: Springer.

Gouge, M., Denlinger, E., Irwin, J., Li, C., & Michaleris, P. (2019). Experimental validation of thermo-mechanical part-scale modeling for laser powder bed fusion processes. *Additive Manufacturing*, 29, 100771.

Han, J., Wu, M., Ge, Y., & Wu, J. (2018). Optimizing the structure accuracy by changing the scanning strategy using selective laser melting. *The International Journal of Advanced Manufacturing Technology*, 95(9), 4439-4447.

Hanumaiah, N., & Ravi, B. (2007). Rapid tooling form accuracy estimation using region elimination adaptive search-based sampling technique. *Rapid Prototyping Journal*.

Haque, M. E., Banerjee, D., Mishra, S. B., & Nanda, B. K. (2019). A numerical approach to measure the surface roughness of FDM build part. *Materials Today: Proceedings*, 18, 5523-5529.

Hocken, R. J., & Pereira, P. H. (Eds.). (2012). *Coordinate measuring machines and systems* (Vol. 6). Boca Raton, FL: CRC press.

Hodge, N. E., Ferencz, R. M., & Solberg, J. M. (2014). Implementation of a thermomechanical model for the simulation of selective laser melting. *Computational Mechanics*, 54(1), 33-51.

Huang, Q., Nouri, H., Xu, K., Chen, Y., Sosina, S., & Dasgupta, T. (2014). Statistical predictive modeling and compensation of geometric deviations of three-dimensional printed products. *Journal of Manufacturing Science and Engineering*, 136(6).

Huang, Q., Nouri, H., Xu, K., Chen, Y., Sosina, S., & Dasgupta, T. (2014, August). Predictive modeling of geometric deviations of 3d printed products-a unified modeling approach for cylindrical and polygon shapes. In *2014 IEEE International Conference on Automation Science and Engineering (CASE)* (pp. 25-30). IEEE.

Huang, Q., Zhang, J., Sabbaghi, A., & Dasgupta, T. (2015). Optimal offline compensation of shape shrinkage for three-dimensional printing processes. *IIE transactions*, 47(5), 431-441.

Huang, Z., Dantan, J. Y., Etienne, A., Rivette, M., & Bonnet, N. (2018). Geometrical deviation identification and prediction method for additive manufacturing. *Rapid Prototyping Journal*.

ISO 1101: 2017, Geometrical product specifications (GPS): Geometrical tolerancing - Tolerances of form, orientation, location and run-out.

ISO 286-1:2010, Geometrical product specifications (GPS) — ISO code system for tolerances on linear sizes — Part 1: Basis of tolerances, deviations and fits.

ISO 17296-3: 2014, Additive manufacturing - General principles- Part 3: Main characteristics and corresponding test methods.

ISO/ASTM 52900:2015 (ASTM F2792), Additive manufacturing – General principles – Terminology.

ISO/ASTM 52902:2019, [ASTM F42] Additive manufacturing — test artifacts — geometric capability assessment of additive manufacturing systems.

Jia, Q., & Gu, D. (2014). Selective laser melting additive manufacturing of Inconel 718 superalloy parts: Densification, microstructure and properties. *Journal of Alloys and Compounds*, 585, 713-721.

King, W. E., Anderson, A. T., Ferencz, R. M., Hodge, N. E., Kamath, C., Khairallah, S. A., & Rubenchik, A. M. (2015). Laser powder bed fusion additive manufacturing of metals; physics, computational, and materials challenges. *Applied Physics Reviews*, 2(4), 041304.

Klahn, C., Singer, D., & Meboldt, M. (2016). Design guidelines for additive manufactured snap-fit joints. *Procedia CIRP*, 50, 264-269.

Leach, R. K., Bourell, D., Carmignato, S., Donmez, A., Senin, N., & Dewulf, W. (2019). Geometrical metrology for metal additive manufacturing. *CIRP annals*, 68(2), 677-700.

Li, C., Liu, J. F., Fang, X. Y., & Guo, Y. B. (2017). Efficient predictive model of part distortion and residual stress in selective laser melting. *Additive Manufacturing*, 17, 157-168.

Lieneke, T., Denzer, V., Adam, G. A., & Zimmer, D. (2016). Dimensional tolerances for additive manufacturing: Experimental investigation for Fused Deposition Modeling. *Procedia CIRP*, 43, 286-291.

Lu, Y., Wu, S., Gan, Y., Huang, T., Yang, C., Junjie, L., & Lin, J. (2015). Study on the microstructure, mechanical property and residual stress of SLM Inconel-718 alloy manufactured by differing island scanning strategy. *Optics & Laser Technology*, 75, 197-206.

Luan, H., & Huang, Q. (2015, August). Predictive modeling of in-plane geometric deviation for 3D printed freeform products. In 2015 IEEE International Conference on Automation Science and Engineering (CASE) (pp. 912-917). IEEE.

Luo, Z., & Zhao, Y. (2018). A survey of finite element analysis of temperature and thermal stress fields in powder bed fusion additive manufacturing. *Additive Manufacturing*, 21, 318-332.

Mahesh, M., Wong, Y. S., Fuh, J. Y. H., & Loh, H. T. (2004). Benchmarking for comparative evaluation of RP systems and processes. *Rapid Prototyping Journal*.

Mahmood, S., Qureshi, A. J., & Talamona, D. (2018). Taguchi based process optimization for dimension and tolerance control for fused deposition modelling. *Additive Manufacturing*, 21, 183-190.

Mahmood, S., Qureshi, A. J., Goh, K. L., & Talamona, D. (2017). Tensile strength of partially filled FFF printed parts: meta modelling. *Rapid Prototyping Journal*.

Maidin, S. B., Campbell, I., & Pei, E. (2012). Development of a design feature database to support design for additive manufacturing. *Assembly Automation*.

Mehdi-Souzani, C., Piratelli-Filho, A., & Anwer, N. (2017). Comparative study for the metrological characterization of additive manufacturing artefacts. In *Advances on Mechanics, Design Engineering and Manufacturing* (pp. 191-200). Springer, Cham.

Michaleris, P. (Ed.). (2011). *Minimization of welding distortion and buckling: modelling and implementation*. Elsevier.

Mishurova, T., Cabeza, S., Thiede, T., Nadammal, N., Kromm, A., Klaus, M., ... & Bruno, G. (2018). The influence of the support structure on residual stress and distortion in SLM Inconel 718 parts. *Metallurgical and Materials Transactions A*, 49(7), 3038-3046.

Mohamed, O. A., Masood, S. H., & Bhowmik, J. L. (2015). Optimization of fused deposition modeling process parameters: a review of current research and future prospects. *Advances in Manufacturing*, 3(1), 42-53.

Mohamed, O. A., Masood, S. H., & Bhowmik, J. L. (2016). Optimization of fused deposition modeling process parameters for dimensional accuracy using I-optimality criterion. *Measurement*, 81, 174-196.

Moroni, G., Syam, W. P., & Petro, S. (2014). Towards early estimation of part accuracy in additive manufacturing. *Procedia CIRP*, 21, 300-305.

Morse, E., Dantan, J. Y., Anwer, N., Söderberg, R., Moroni, G., Qureshi, A., ... & Mathieu, L. (2018). Tolerancing: Managing uncertainty from conceptual design to final product. *CIRP Annals*, 67(2), 695-717.

Mostafa, K. G., Montemagno, C., & Qureshi, A. J. (2018). Strength to cost ratio analysis of FDM Nylon 12 3D Printed Parts. *Procedia Manufacturing*, 26, 753-762.

Mostafa, K., Qureshi, A. J., & Montemagno, C. (2017, November). Tolerance control using subvoxel gray-scale DLP 3D printing. In *ASME International Mechanical Engineering Congress and Exposition* (Vol. 58356, p. V002T02A035). American Society of Mechanical Engineers.

Moylan, S., Slotwinski, J., Cooke, A., Jurens, K., & Donmez, M. A. (2012, August). Proposal for a standardized test artifact for additive manufacturing machines and processes. In *Proceedings of the 2012 annual international solid freeform fabrication symposium* (pp. 6-8). Austin, TX.

Moylan, S., Slotwinski, J., Cooke, A., Jurens, K., & Donmez, M. A. (2014). An additive manufacturing test artifact. *Journal of research of the National Institute of Standards and Technology*, 119, 429.

Nadammal, N., Cabeza, S., Mishurova, T., Thiede, T., Kromm, A., Seyfert, C., ... & Bruno, G. (2017). Effect of hatch length on the development of microstructure, texture and residual stresses in selective laser melted superalloy Inconel 718. *Materials & Design*, 134, 139-150.

Navangul, G., Paul, R., & Anand, S. (2013). Error minimization in layered manufacturing parts by stereolithography file modification using a vertex translation algorithm. *Journal of Manufacturing Science and Engineering*, 135(3).

Paris, H., & Mandil, G. (2018). Extracting features for manufacture of parts from existing components based on combining additive and subtractive technologies. *International Journal on Interactive Design and Manufacturing (IJIDeM)*, 12(2), 525-536.

Paul, R., & Anand, S. (2015). A new Steiner patch-based file format for additive manufacturing processes. *Computer-Aided Design*, 63, 86-100.

Peng, H., Ghasri-Khouzani, M., Gong, S., Attardo, R., Ostiguy, P., Gatrell, B. A., ... & Hoelzle, D. (2018). Fast prediction of thermal distortion in metal powder bed fusion additive manufacturing: Part 1, a thermal circuit network model. *Additive Manufacturing*, 22, 852-868.

Peng, H., Ghasri-Khouzani, M., Gong, S., Attardo, R., Ostiguy, P., Rogge, R. B., ... & Hoelzle, D. (2018). Fast prediction of thermal distortion in metal powder bed fusion additive manufacturing: Part 2, a quasi-static thermo-mechanical model. *Additive Manufacturing*, 22, 869-882.

Pfeifer, T., Koch, C., Van Hulle, L., Capote, G. M., & Rudolph, N. (2016). Optimization of the FDM additive manufacturing process. *Proceedings of the SPE ANTEC™ Indianapolis, Indianapolis, IN, USA, 22-25.*

Qureshi, A. J., Mahmood, S., Wong, W. L. E., & Talamona, D. (2015). Design for Scalability and Strength Optimisation for components created through FDM process. In *DS 80-6 Proceedings of the 20th International Conference on Engineering Design (ICED 15) Vol 6: Design Methods and Tools-Part 2 Milan, Italy, 27-30.07. 15 (pp. 255-266).*

Rajaguru, K., Karthikeyan, T., & Vijayan, V. (2020). Additive manufacturing—State of art. *Materials today: proceedings*, 21, 628-633.

Rebaioli, L., & Fassi, I. (2017). A review on benchmark artifacts for evaluating the geometrical performance of additive manufacturing processes. *The International Journal of Advanced Manufacturing Technology*, 93(5), 2571-2598.

Roy, R. K. (2001). *Design of experiments using the Taguchi approach: 16 steps to product and process improvement.* John Wiley & Sons.

Rupal, B. S., & Qureshi, A. J. (2018). Geometric Deviation Modeling and Tolerancing in Additive Manufacturing: A GD&T Perspective. In *1st Conference of NSERC Network for Holistic Innovation in Additive Manufacturing (HI-AM) (pp. 1-6).*

Rupal, B. S., Mostafa, K. G., Wang, Y., & Qureshi, A. J. (2019). A reverse cad approach for estimating geometric and mechanical behavior of fdm printed parts. *Procedia Manufacturing*, 34, 535-544.

Samie Tootooni, M., Dsouza, A., Donovan, R., Rao, P. K., Kong, Z. J., & Borgesen, P. (2017). Classifying the dimensional variation in additive manufactured parts from laser-scanned three-dimensional point cloud data using machine learning approaches. *Journal of Manufacturing Science and Engineering*, 139(9).

Scaravetti, D., Dubois, P., & Duchamp, R. (2008). Qualification of rapid prototyping tools: proposition of a procedure and a test part. *The International Journal of Advanced Manufacturing Technology*, 38(7-8), 683-690.

Schleich, B., & Wartzack, S. (2015). Evaluation of geometric tolerances and generation of variational part representatives for tolerance analysis. *The International Journal of Advanced Manufacturing Technology*, 79(5), 959-983.

Schleich, B., Anwer, N., Mathieu, L., & Wartzack, S. (2014). Skin Model Shapes: A new paradigm shift for geometric variations modelling in mechanical engineering. *Computer-Aided Design*, 50, 1-15.

Schmidt, M., Merklein, M., Bourell, D., Dimitrov, D., Hausotte, T., Wegener, K., ... & Levy, G. N. (2017). Laser based additive manufacturing in industry and academia. *Cirp Annals*, 66(2), 561-583.

Schoinochoritis, B., Chantzis, D., & Salonitis, K. (2017). Simulation of metallic powder bed additive manufacturing processes with the finite element method: A critical review. *Proceedings of the Institution of Mechanical Engineers, Part B: Journal of Engineering Manufacture*, 231(1), 96-117.

Shah, J. J. (1991)"Assessment of features technology, 'Computer Aided Design.": 331-343.

Shahrain, M., Didier, T., Lim, G. K., & Qureshi, A. J. (2016). Fast deviation simulation for 'fused deposition modeling' process. *Procedia Cirp*, 43, 327-332.

Singh, S., Singh, G., Prakash, C., & Ramakrishna, S. (2020). Current status and future directions of fused filament fabrication. *Journal of Manufacturing Processes*, 55, 288-306.

Song, J., Zhang, L., Wu, W., He, B., Ni, X., Xu, J., ... & Lu, L. (2019). Understanding processing parameters affecting residual stress in selective laser melting of Inconel 718 through numerical modeling. *Journal of Materials Research*, 34(8), 1395-1404.

Sood, A. K., Ohdar, R. K., & Mahapatra, S. S. (2009). Improving dimensional accuracy of fused deposition modelling processed part using grey Taguchi method. *Materials & Design*, 30(10), 4243-4252.

Sossou, G., Demoly, F., Montavon, G., & Gomes, S. (2018). An additive manufacturing-oriented design approach to mechanical assemblies. *Journal of Computational Design and Engineering*, 5(1), 3-18.

Toguem, S.-C. T., Mehdi-Souzani C., Anwer N., and Nouira H., "Customized design of artefacts for 649 additive manufacturing," in euspen's 19th International Conference & Exhibition, 2019, Accessed: Apr. 650 19, 2020.

Uddin, S. Z., Murr, L. E., Terrazas, C. A., Morton, P., Roberson, D. A., & Wicker, R. B. (2018). Processing and characterization of crack-free aluminum 6061 using high-temperature heating in laser powder bed fusion additive manufacturing. *Additive Manufacturing*, 22, 405-415.

Umaras, E., & Tsuzuki, M. S. (2017). Additive manufacturing-considerations on geometric accuracy and factors of influence. *IFAC-Papers Online*, 50(1), 14940-14945.

Vahabli, E., & Rahmati, S. (2016). Application of an RBF neural network for FDM parts' surface roughness prediction for enhancing surface quality. *International journal of precision engineering and manufacturing*, 17(12), 1589-1603.

Vilardell, A. M., Takezawa, A., Du Plessis, A., Takata, N., Krakhmalev, P., Kobashi, M., ... & Yadroitsev, I. (2019). Topology optimization and characterization of Ti6Al4V ELI cellular lattice structures by laser powder bed fusion for biomedical applications. *Materials Science and Engineering: A*, 766, 138330.

Wang, A., Song, S., Huang, Q., & Tsung, F. (2016). In-plane shape-deviation modeling and compensation for fused deposition modeling processes. *IEEE Transactions on Automation Science and Engineering*, 14(2), 968-976.

Whip, B., Sheridan, L., & Gockel, J. (2019). The effect of primary processing parameters on surface roughness in laser powder bed additive manufacturing. *The International Journal of Advanced Manufacturing Technology*, 103(9), 4411-4422.

Witherell, P., Herron, J., & Ameta, G. (2016). Towards annotations and product definitions for additive manufacturing. *Procedia CIRP*, 43, 339-344.

Y. Zhang and J. Zhang, "Finite element simulation and experimental validation of distortion and cracking failure phenomena 772 in direct metal laser sintering fabricated component," *Additive Manufacturing*, vol. 16, pp. 49–57, 2017.

Yang, H., Yang, J., Huang, W., Wang, Z., & Zeng, X. (2018). The printability, microstructure, crystallographic features and microhardness of selective laser melted Inconel 718 thin wall. *Materials & Design*, 156, 407-418.

Yang, L., & Anam, M. A. (2014). An investigation of standard test part design for additive manufacturing. In *Proceeding of the Solid Free Form Fabrication Symposium*.

Yang, Y. P., Jamshidinia, M., Boulware, P., & Kelly, S. M. (2018). Prediction of microstructure, residual stress, and deformation in laser powder bed fusion process. *Computational Mechanics*, 61(5), 599-615.

Yi, J. H., Kang, J. W., Wang, T. J., Wang, X., Hu, Y. Y., Feng, T., ... & Wu, P. Y. (2019). Effect of laser energy density on the microstructure, mechanical properties, and deformation of Inconel 718 samples fabricated by selective laser melting. *Journal of Alloys and Compounds*, 786, 481-488.

Zhang, Y., Bernard, A., Gupta, R. K., & Harik, R. (2016). Feature based building orientation optimization for additive manufacturing. *Rapid Prototyping Journal*.

Zuowei, Z. H. U., Keimasi, S., Anwer, N., Mathieu, L., & Lihong, Q. I. A. O. (2017). Review of shape deviation modeling for additive manufacturing. In *Advances on Mechanics, Design Engineering and Manufacturing* (pp. 241-250). Springer, Cham.

Appendix A: GBTA features for normative benchmark

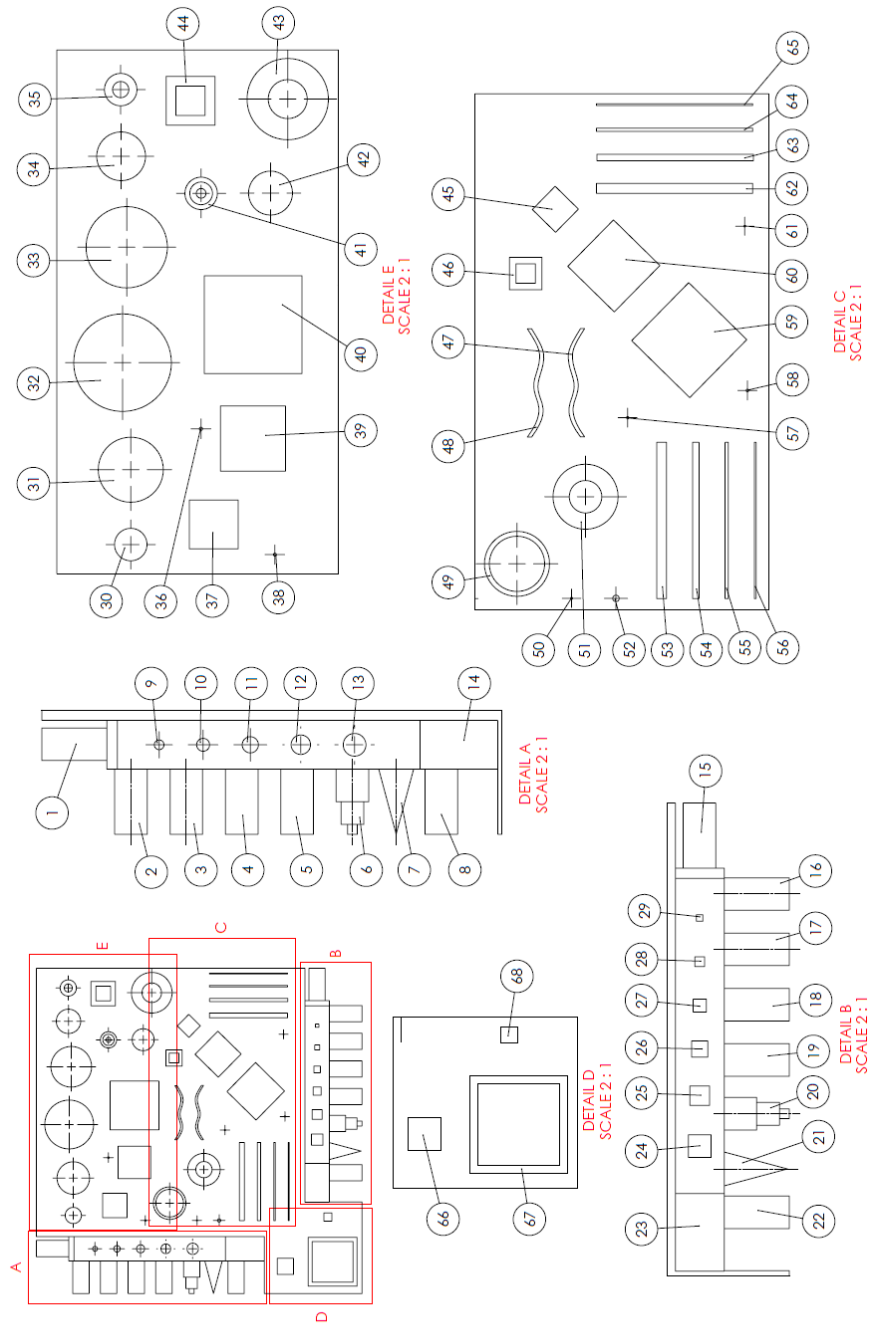


Figure A1. GBTA drawing depicting all the features along with their numbering

Table A1. GBTA features description as per the numbering

GD&T Characteristics	Plane/ Axis	Features
Flatness	XY	1,4,5,8,13,15,18,19,22,24,30,31,32,33,37,39,40,45,60,66,68
	YZ	2,4,18,19,24,37,39,40,44,62,63,64,65,66
	ZX	4,5,16,18,24,37,39,40,44,53,54,55,56,66
Straightness	XY	1,4,5,8,15,18,19,22,37,39,40,53,62
	YZ	24,37,39,40,62,65,66,67
	ZX	24,37,39,40,53,56,66,67
Parallelism	XY	4,5,8,13,18,22,24,30,31,32,37,39,40,60,66
	YZ	2,4,18,19,24,37,39,40,62,63,64,65,66
	ZX	4,5,16,18,24,37,39,40,53,54,55,56,66
Perpendicularity	XY	4,5,8,18,19,22,24,37,39,40,66
	YZ	24,37,39,40,62,63,64,65,66
	ZX	24,37,39,40,53,54,55,56,66
Angularity		14,23
Circularity	X	2,3,6B,6M,6T,7
	Y	16,17,20B,20M,20T,21
	Z	9,11,13,30,31,32,33,34,35,36,38,41B,41M,41T,42,43O,43I,49O,49I,50,51O,51I,52,57,58,61
Cylindricity	X	2,3,6B,6M
	Y	16,17,20B,20M
	Z	9,10,11,12,13,30,31,32,33,34,35,38,41B,41M,43O,43I,49O,49I,50,51O,51I,52,57,58,61
Concentricity	X	6M,6T
	Y	20M,20T
	Z	41M,41T
Circular Runout	X	6M,6T
	Y	20M,20T
	Z	41M,41T

Total Runout	X	6M
	Y	20M
	Z	41M